Analysis of Intergranular Stress Corrosion Cracking in Al-Mg Alloys under Atmospheric Exposure Conditions

---

A
Dissertation
Presented to
the faculty of the School of Engineering and Applied Science
University of Virginia

---

in partial fulfillment
of the requirements for the degree

Doctor of Philosophy

by

Patrick Steiner

August 2020

APPROVAL SHEET

This
Dissertation
is submitted in partial fulfillment of the requirements
for the degree of
Doctor of Philosophy

Author: Patrick Steiner

This Dissertation has been read and approved by the examing committee:

Advisor: James Burns

Advisor:

Committee Member: Robert Kelly

Committee Member: James Fitz-Gerald

Committee Member: John Scully

Committee Member: Devin Harris

Committee Member: Fritz Friedersdorf

Committee Member:

Accepted for the School of Engineering and Applied Science:

Craig H. Benson, School of Engineering and Applied Science

August 2020

Executive Summary

Intergranular stress corrosion cracking (IG-SCC) is a continuous problem for many alloy systems, especially for high strength Al-Mg alloys in aggressive saline environments. It is believed that a combined process starting with anodic dissolution of the intergranular β phase (Al_3Mg_2) coupled with hydrogen enhanced decohesion ahead of the crack tip is the underlying mechanism, with crack growth rates being shown to be highly dependent on both crack tip electrochemical potential and solution chemistry. The majority of these studies have been performed in electrochemically controlled full immersion environment where the bulk solution has both a large volume, fixed solution concentration, and the potential is fixed via a potentiostat. This differs from atmospheric environments, which involve lower solution geometries, higher ion concentrations, and no governing potentiostat. These environments are more typical of real-life service conditions and may exhibit different underlying IG-SCC mechanisms and crack growth rates compared to analogous immersion studies. However, atmospheric environments complicate testing techniques (e.g. linear elastic fracture mechanics (LEFM) and direct current potential drop (dcPD)) used to characterize IG-SCC behavior. As such the objective of this dissertation is to systematically isolate and understand the various distinct factors that are unique to atmospheric environments to better inform alloy development, prognosis modelling, and potential IG-SCC mitigation strategies.

The objective of this dissertation is to address these knowledge gaps by focusing on the following research questions:

- What are the potential limitations and modifications imposed upon the IG-SCC mechanism by transfer of the cathode from an infinite supply to solely the bulk surface of the sample surface?
- How do various solution geometries of reduced volume and solution layer thickness effect the IG-SCC mechanism development and/or propagation in Al-Mg alloys in saline environments, and what is the governing factor(s) at play?
- How do various solution chloride concentrations effect the IG-SCC mechanism development and/or propagation in Al-Mg alloys when exposed to varying atmospheric saline environments?

- Are metal-rich primers a viable IG-SCC mitigation strategy in atmospheric environments, and if so, what is their relative potency as compared to the existing full immersion results?
- In IG-SCC testing protocols that require exposed dcPD current wires, what are the potential effects caused by application of the dcPD current on the measured or applied electrochemical potential?

Towards this end, the dissertation is divided into three separate research thrusts. First, the isolated contributions of the removal of a governing potentiostat, solution geometry, and solution chloride composition were assessed. Archetypal atmospheric environments were created and benchmarked to isolate the geometric and chemical conditions that may be observed in service environments. The environments chosen were: (1) a misting condition, typified by a constant salt spray, (2) thin film condition, wherein a static thin film of solution was maintained around the crack tip, and (3) a wicking condition, typified by solution only located in the crack notch/wake. These atmospheric testing protocols were designed under the requirements that they 1) are compatible with LEFM-based testing, 2) are able to be electrochemically monitored, and 3) help to isolate important geometric and chemical features that would be observed in nominal atmospheric conditions. Utilizing these atmospheric environment protocols, it was confirmed that removal of a governing potentiostat transferred cathodic reactions from the potentiostat to the bulk specimen surface. Transfer of the cathodic reactions to the bulk surface was then determined to result in cathodic limitation of the IG-SCC mechanism in atmospheric environments based on the geometry of the solution due to ohmic drop and cathodic area reduction. This was explored further in highly-controlled thin film testing, in which a direct correlation between thin film thickness and IG-SCC susceptibility was observed (distinguished by changes in the IG-SCC parameters K_{TH} and da/dt_{II}). Lastly, atmospheric testing with multiple solution concentrations revealed that as chloride concentration increased IG-SCC susceptibility was increased unilaterally across all environments with little variation across the degrees of cathodic limitation.

Second, the practicality of mitigating IG-SCC via metal-rich primers in atmospheric environments was analyzed. These metal-rich coatings, which to date have only been evaluated in full immersion testing, employ various electrochemical methods to mitigate IG-SCC growth that may be drastically affected by the geometrical or compositional changes due to atmospheric conditions. Testing of a candidate ZRP in misting environments showed a reduction of the IG-SCC susceptibility and establishment of protective electrochemical potentials, with little impact of scribe length on the IG-SCC behavior.

Third, the effects of dcPD current wire application was assessed to allow for extension of these atmospheric environment protocols to more complex geometries and corrosion systems. It was determined that a strong metallurgical bond was required between the dcPD current wires and the sample surface, otherwise capacitance resulting from the dcPD current wire bonding could have a significant effect on both electrochemical potential or voltage applied. Specifically, attention must be paid to systems involving highly corrosive electrolytes.

Considering the practical impact of the current dissertation, results indicate that across all atmospheric environments the use of IG-SCC kinetics for full immersion testing at an appropriate set potential and the highest anticipated chloride concentration remain conservative across all conditions for Al-Mg alloys. Critically, these results do not account for the transient effects of wetting and drying, external contaminants, or other environmental effects such as UV radiation. Furthermore, the use of metal-rich primers to mitigate IG-SCC growth in atmospheric environments was found to result in a reduction of the IG-SCC susceptibility similar to that seen in full-immersion conditions, albeit at reduced effectiveness. Lastly, the method of dcPD current wire attachment was found to be critically important for environmental setups that require exposed dcPD current wires to solution. Considering scientific impacts, the development and benchmarking of multiple archetypal environments compatible with LEFM-based testing and electrochemical monitoring were designed and verified for the IG-SCC testing of samples in atmospheric environments. These protocols are easily transferable to other material systems/geometries and establish a rigorous method to qualitatively assess atmospheric environmental effects. Finally, key insights into the proposed IG-SCC mechanism for Al-Mg alloys were determined such as the governing effects of the cathodic current and close relation between the bulk surface potential and the anticipated anodic demand.

Relevant Research Publications

1. **P.J. Steiner**, J.T. Burns, Mechanistic Studies of Intergranular Stress Corrosion Cracking in Al-Mg Alloys under Atmospheric Exposure Conditions, CORROSION. 2018;74(10):1117-1131.
    a. Steiner contribution: primary performer, conducted experiments, analyzed data, wrote manuscript.
2. M.E. McMahon, **P.J. Steiner**, A.B. Lass, J.T. Burns, The Effect of Temper and Composition on the Stress Corrosion Cracking of Al-Mg Alloys, CORROSION. 2017;73(4):347-361.
    a. Steiner contribution: primary co-performer, conducted experiments, analyzed data, contributed to manuscript.
3. M.E. McMahon, **P.J. Steiner**, A.B. Lass, J.T. Burns, The Effect of Loading Orientation on the Stress Corrosion Cracking of Al-Mg Alloys, CORROSION. 2017;73(6):713-723.
    a. Steiner contribution: primary co-performer, conducted experiments, analyzed data, contributed to manuscript.
4. M.E. McMahon, R.L. Haines, **P.J. Steiner**, J.M. Lass, J.T. Burns, Beta phase distribution in Al-Mg alloys of varying composition and temper, Corrosion Science. 2020;169(2020):108618.
    a. Steiner contribution: co-performer, conducted pre and post characterization

Acknowledgements

First off, I would like to sincerely thank my research advisor, Prof. James Burns, for all the mentorship and support you have provided over my graduate career. I can only imagine some of the trouble I have put you through over the years with last minute deadlines and the various shenanigans I may have (allegedly) orchestrated. I have always admired your patience with me and willingness to appease my more creative research ideas and methods, which lucky for me more often than not worked out for the better. Your lessons, advice, and view of how scientific research should be conducted will be greatly treasured as I delve deeper into the scientific world. Let the mural on my office window stand as a testament of my respect for you, and if you ever get me that beer you owe me I might just tell you where your non-pink office chair wheels are hidden.

I would also like to thank my dissertation committee: Prof. Rob Kelly, Prof. John Scully, Prof. James Fitz-Gerald, Prof. Devin Harris, and Dr. Fritz Friedersdorf. Your input and feedback through my research have been invaluable towards this thesis. In particular I would like to thank Prof. Rob Kelly, you always seemed to have some time whenever I had an electrochemistry question I couldn't seem to answer. Prof. James Fitz-Gerald perhaps deserves my biggest thanks, however, as he also had the (mis?)fortune of being my undergraduate research advisor. I cannot begin to thank you enough for your mentorship during those years and desire to see me succeed.

I must also acknowledge my coworkers, particularly the past and present members of the Burns research group. Work has truly been a pleasure over the years and I always looked forward to our interactions together. Honorable mentions include Dr. Matt McMahon, who was my partner in crime for most of my tenure (and whom I still need to repay for that one prank), Dr. Zach Harris, the perfect senior student mentor and friend, Ryan Katona, whose cooperation was vital to many parts of my research, and Adam Thompson, whose friendliness and willingness to help made many late nights more tolerable.

Next, I would like to thank my family and friends, who have made my time in Charlottesville truly outstanding. Although he probably wasn't ecstatic to have his little brother follow him to grad school, my brother Dr. Matthew Steiner and his wife Dr. Kirsten Andersen have been a bedrock for me during my early years in Charlottesville. My sister, Dr. Caitlin Steiner, more so as she always had spare room in her house when I needed it and time to hang out with her little brother. I will always cherish the time my older siblings were in such close proximity, and without your help I am not sure I could have done it alone. Lastly, I would like to thank my parents most of all, and can only apologize for not having called home more. Without your support and love none of this would have been possible, and I hope that I have made you proud.

This research was supported financially by the Office of Naval Research (Awards #N00014-15-1-2491 and #N00014-18-S-B001), with Dr. Airan Perez as the Scientific Officer.

Table of Contents

List of Figures

List of Tables

Nomenclature

- IGC = intergranular Corrosion
- SCC = stress corrosion cracking
- IG-SCC = intergranular stress corrosion cracking
- HE = hydrogen embrittlement
- HEDE = hydrogen enhanced decohesion
- β phase = Al_3Mg_2
- α phase = Al – 5 wt.% Mg solid solution
- NAMLT = nitric acid mass loss test
- LEFM = linear elastic fracture mechanics
- SEN(T) = single edge notch (tensile)
- L = longitudinal/rolling direction
- T = transverse direction
- S = short transverse direction
- dcPD = direct current potential drop
- K_J = elastic-plastic stress intensity
- K_{TH} = threshold stress intensity
- da/dt_{II} = stage II crack growth rate
- OCP = open circuit potential
- FOCP = floating open circuit potential
- ORR = oxygen reduction reaction
- SCE = saturated calomel electrode
- SSC = sintered silver chloride
- EDM = electric discharge machined
- AAO = anodized alumina oxide
- WL = water layer
- ZRP = zinc rich primer

Chapter 1. Introduction and background

1.1. IG-SCC in Al-Mg alloys – status of the problem

Aluminum-magnesium alloys (classified as the AA5xxx series) are a work hardened, solid solution strengthened alloy class that has seen extensive use in marine applications due to their high strength-to-weight ratio, good weldability, and low cost[1]. However, as they are solid solution strengthened via supersaturation with magnesium, they can precipitate a deleterious β phase on grain boundaries at relatively low temperatures (as low ≈40°C)[2–5]. This process is termed sensitization and can occur in conditions comparable to in-service environments. The β phase is highly anodic to the parent Al matrix and can thus make the alloy susceptible to intergranular corrosion (IGC) and intergranular stress corrosion cracking (IG-SCC) in aqueous chloride environments[6]. Susceptibilities of these alloys to IGC and IG-SCC are often correlated to their Nitric Acid Mass Loss Test (NAMLT) value, wherein mass loss due to grain fallout during a nitric acid treatment is correlated to the β phase grain boundary coverage (reported in units of mg/cm^2) as described by ASTM G67[7].

The proposed mechanism of IG-SCC in 5xxx series Al alloys is still under debate, but substantial evidence supports a coupled anodic dissolution and hydrogen embrittlement (HE) mechanism[2,8,9]. It is suggested that dissolution of the highly anodic β phase at the crack front will lead to the production of metal cations, which then hydrolyze to decrease the pH of the crack tip solution. There will also be an ingress of chloride ions from the bulk solution to maintain charge balance. The low pH and high chloride environment can then enable the dissolution of the primary α Al matrix which will cause further crack tip acidification. While anodic dissolution rates of ~500 nm/sec have been observed, the crack growth rates measured experimentally are orders of magnitude higher[8]. This has led to speculation that the high pH and chloride concentration will increase the overpotential for H production at the crack tip, which can then adsorb onto the surface and then absorb into the Al matrix resulting in hydrogen embrittlement[4,8]. While the exact method of hydrogen embrittlement in these alloys is controversial, it has been postulated that the H will diffuse into the crack tip process zone and (1) weaken the grain boundary and/or particle-boundary to facilitate interface decohesion (a H-enhanced decohesion (HEDE) mechanism), and/or (2) enable enhanced plasticity due to shielding of the elastic fields around the dislocations (a H-enhanced local plasticity (HELP) mechanism).[8]

Prominently, the bulk of the research on the IGC and IG-SCC susceptibility of AA5xxx series alloys has been performed with specimens fully immersed in an electrolyte of constant composition as they are easy to control and are amenable to advanced characterization methods[4,5,8–14]. These full immersion conditions may not be fully representative of atmospheric service conditions that are often typified by salt-spray, rain, or a deliquesced thin-film electrolyte which involve lower volumes of corrosive solution around the crack tip[15]. Critically, these atmospheric environments can differ by two key aspects: a reduced solution geometry around the crack tip and an increase in solution solute concentrations. These differences may considerably change observed crack growth kinetics based on the proposed mechanism of IG-SCC in these alloys and dramatically change the IG-SCC behaviors seen in service. This motivates further exploration of these factors to inform prognosis modeling[13,16], alloy development[17–20], and mitigation strategies[21,22].

Furthermore, many recent high fidelity linear elastic fracture (LEFM) based studies of IG-SCC have been performed using a potentiostat to fix the electrochemical potential[5,11]. This approach is reasonable given the (1) the known/typical drift in open circuit potential over time[23], and (2) the strong dependence of IG-SCC susceptibility on the electrochemical potential[4,21]. Removal of the potentiostat (or other galvanic coupling) is of large consequence as any anodic dissolution must therefore be supported by cathodic current provided from elsewhere on the sample[24]. This coupling is critically important in the context of the proposed coupled IG-SCC mechanisms where anodic dissolution enables the development of an aggressive crack chemistry that sets the conditions necessary for the H-production at the crack tip. When combined with the reduction in solution geometry around the crack tip, this can potentially lead to substantial limitation of the supporting cathodic reaction, generally the ORR reaction on the bulk Al surface, through various effects such as ohmic drop, increased solution resistance, and/or restriction of the surface area in which it can occur[24–26]. Limitation of the balancing cathodic reaction may in turn stifle anodic dissolution rates in the proposed IG-SCC mechanism, resulting in lower IG-SCC susceptibilities than observed for full immersion environments.

Likewise, effects on the solution composition can also drastically alter IG-SCC growth behavior. In full immersion studies it has been observed that increased solution saline concentrations can lead to increased IG-SCC susceptibility by decreasing the pitting potentials of both the β and α phases[21]. This can lead to increased levels of dissolution at the crack tip and consequently increased levels of H-production. These increased saline concentrations can easily occur in atmospheric environments due to evaporation and deliquescence of water vapor on salt-contaminated surfaces. Furthermore, changes in the electrolyte composition can impact several other parameters critical to the IG-SCC mechanism, such as the electrolyte resistivity, crack chemistry development, passivation, and the open circuit potential of the system[4,9,14,21,27]. While these factors may affect the anodic dissolution of the crack tip, they could also drastically affect the balancing cathodic reaction on the bulk surface. The above demonstrates that the reduction in solution geometry and increase in solution composition are a very complex and intertwined paradigm that can deviate greatly from a potentiostatically controlled, constant composition full immersion condition.

Metal-rich coatings have gathered considerable interest for the potential mitigation of IGC and IG-SCC damage in service vessels due to their electrochemical properties. A primary mechanism by which they can protect 5xxx series alloys is by galvanically coupling metal pigments in the coating to the base Al alloy so that they can reduce the crack tip potential to more cathodic values less conducive to IG-SCC. Such coatings have been observed to retard or fully mitigate the IG-SCC mechanism altogether should they cathodically polarize the alloy below that of the breakdown potential of the β-phase ($E_{pit(\beta)}$)[28,29]. Furthermore, additional protection may be provided by chemical ion based inhibition or corrosion products formed during this process that provide a secondary impedance barrier to inhibit potent cathodic sites[28–33]. While numerous metal-rich systems have been considered and studied for Al and steel alloys, such as Zn[29,32–34], Mg[28,30,31], and other related hybrids[28], little study exists specifically on Al-Mg alloys in aggressive saline environments and atmospheric environments.

The potential effects of atmospheric environments on the mechanisms and mitigation of IG-SCC in highly sensitized Al-Mg alloys in aggressive saline conditions must be more fully assessed and understood. This baseline knowledge will enable more detailed prognosis

modeling, informed alloy development, and improved mitigation strategies such as cathodically protective metal-rich primers for use in marine environments.

1.2. Knowledge gaps

The previous overview identifies the following knowledge gaps that motivate the research inquiries in this dissertation:

(1) The known potential-dependent IG-SCC behavior of sensitized Al-Mg alloys in full-immersion saline environments has been extensively documented in the literature, especially at potentials cathodic to the open circuit potential (~0.8 V_{SCE}) [4,8,10,21]. The bulk of these studies, however, have been performed with a governing potential typically established via a potentiostat that essentially acts as an infinite cathodic supply. Removal of this potentiostat transfers the necessary cathodic reactions for IG-SCC to the bulk surface, as has been demonstrated in pitting studies[24–26], which may limit the extent to which the cathodic current may be supplied.

(2) The effect of solution geometries that may develop during atmospheric testing can differ drastically in both thin film thickness and solution volume. This reduction can produce three possible effects: (1) coupled with the removal of a governing potentiostat, these reduced thicknesses and volumes could potentially limit cathodic current availability by restricting cathodic reach through the solution through increased ohmic resistance, (2) reduced diffusional distances between the atmosphere and sample surface could affect dissolved oxygen content and therefore increase the cathodic reaction kinetics, and (3) vastly reduced geometries may cause relocation of the cathodic reactions to inside the crack wake and thus effect crack tip chemistry or potential.

(3) In addition to solution geometry, solution composition can be drastically altered during atmospheric development by evaporation and environmental humidity. Notably the chloride concentration may increase by an order of magnitude from deposited salts that remain on the sample surface as the water volume decreases. As shown by many studies, chloride ion concentration is critical to IG-SCC initiation and has a large effect on subsequent IG-SCC crack growth rates in full immersion environments. However, these

effects may be hampered or aided by atmospheric environments, as the lower solution geometries may affect ion diffusion and/or the required electrochemical reactions.

(4) Metal-rich primers have been increasingly demonstrated to provide potential mitigation of IG-SCC damage in various corrosion systems, and recent research has begun to look into their possible implementation on Al-Mg alloys in aggressive saline environments. These metal-rich primers primarily function by forming a galvanic couple between the base alloy and the metal pigments, cathodically polarizing the alloy to protective potentials that mitigate and/or prevent the onset of IG-SCC crack growth. Preliminary studies have shown the efficacy of these primers in full-immersion conditions, but atmospheric environments may impact active protection mechanism for the metal-rich primer and therefore reduce their viability in field environments.

(5) Some IG-SCC testing protocols and sample geometries require the exposure of dcPD current wires to the testing solution. Exposure of these wires in electrolytic solutions may allow for an unknown amount of current to bleed into electrochemical monitoring analysis and result in a loss of accuracy, the extent to which must be examined.

1.3. Research questions

The preceding overview has identified the following research questions regarding the IG-SCC testing of Al-Mg allows in atmospheric environments:

1. What are the potential limitations and modifications imposed upon the IG-SCC mechanism by transfer of the cathode from an infinite supply to solely the bulk surface of the sample surface?
2. How do various solution geometries of reduced volume and solution layer thickness effect the IG-SCC mechanism development and/or propagation in Al-Mg alloys in saline environments, and what is the governing factor(s) at play?
3. How do various solution chloride concentrations effect the IG-SCC mechanism development and/or propagation in Al-Mg alloys when exposed to varying atmospheric saline environments?

4. Are metal-rich primers a viable IG-SCC mitigation strategy in atmospheric environments, and if so, what is their relative potency as compared to the existing full immersion results?
5. In IG-SCC testing protocols that require exposed dcPD current wires, what are the potential effects caused by application of the necessary dcPD current on the measured or applied electrochemical potential/current?

1.4. Dissertation Overview

This dissertation is organized into five chapters, which can be divided into three overarching thrusts. First, in an attempt to characterize the distinguishing characteristics of atmospheric environments and address Research Questions 1-3, Chapters 2 – 4 will focus on isolating the effects of the removal of a governing potentiostat, solution geometry, and solution chloride concentration. To this end, each chapter will first develop rigorous atmospheric testing environments and protocols representative of various archetypal in-service atmospheric conditions. The environments chosen were a misting condition, typified by a constant salt spray, a thin film condition, wherein a static thin film of solution will be maintained around the crack tip, and a wicking condition, typified by solution only located in the crack notch/wake. These environments were designed to be compatible with linear elastic fracture mechanics-based (LEFM) testing techniques with high-fidelity crack monitoring through use of the direct current potential drop (dcPD) method[35]. Additionally, a robust electrochemical monitoring technique was employed in each environment to allow for electrochemical potential measurement or manipulation as this has been shown to play a large role in the proposed IG-SCC mechanism[4,21]. As the use of a standard SCE reference probe is impractical for these environments due to their reduced solution geometries a novel technique was developed.

The second thrust of this dissertation, presented in Chapter 5, will attempt to analyze the efficacy of proposed metal-rich primer IG-SCC mitigation techniques (Research Question 4). These metal-rich coatings, which to date have only been evaluated in full immersion testing, employ various electrochemical methods to mitigate IG-SCC growth and may be drastically affected by the geometrical or compositional changes due to atmospheric conditions. Of specific interest will be primers infused with metals anodic to the Al matrix, thus they will cathodically protect the base alloy and prevent dissolution of the β particles by serving as a sacrificial anode. These metal-rich primers can create physical barriers to corrosion, can release chemicals into solution, or form secondary impedance barriers through corrosion product formation. As these mechanisms rely on the formation of a galvanic cell to function, they are consequently affected by many of the same factors discussed above for the IG-SCC mechanism. Therefore, the efficacy of these primers will be tested in these atmospheric environments to help inform future primer development and application.

The final thrust of this dissertation will attempt to answer Research Question 5 in Chapter 6. The dcPD technique is a powerful tool that can be used in IG-SCC testing to achieve *in-situ* crack growth monitoring and allow for loading protocols that require real time crack length determination. Therefore, it is an integral part of many IG-SCC studies wherein its application is possible. While the geometry in this dissertation is highly amenable to this technique, other geometries and corrosion systems that may also be tested utilizing the atmospheric environments developed in this dissertation may not be and could therefore result in additional areas of concern that must be addressed. Specifically, the exposure of the dcPD current wires to solution may impact nominal electrochemical parameters and result in unforeseen discrepancies in material behavior.

Each chapter begins with a brief summary of the chapter, followed by a brief background section and the identification of the overarching objectives/research questions which guide the work completed within the chapter. An overview of the experimental methods utilized is also provided within each chapter, followed by the presentation and discussion of pertinent results. Each chapter then concludes with a summary of major conclusions and implications pertinent to IG-SCC mitigation and lifing methodologies.

1.5. References

1. N.J.H. Holroyd, and G.M. Scamans, *Corrosion* 72 (2016): pp. 136–143.
2. D.R. Baer, C.F. Windisch, M.H. Engelhard, M.J. Danielson, R.H. Jones, and J.S. Vetrano, *J. Vac. Sci. Technol. A Vacuum, Surfaces, Film.* 18 (2000): pp. 131–136.

3. R. Goswami, G. Spanos, P.S. Pao, and R.L. Holtz, *Mater. Sci. Eng. A* 527 (2010): pp. 1089–1095.
4. C.B. Crane, R.G. Kelly, and R.P. Gangloff, *Corrosion* 72 (2016): pp. 242–263.
5. M.E. Mcmahon, P.J. Steiner, A.B. Lass, and J.T. Burns, *Corrosion* 73 (2017): pp. 347–361.
6. G.M. Scamans, N.J.H. Holroyd, and C.D.S. Tuck, *Corros. Sci.* 27 (1987): pp. 329–347.
7. Standard Test Method for Determining the Susceptibility to Intergranular Corrosion of 5XXX Series Aluminum Alloys by Mass Loss After Exposure to Nitric Acid (NAMLT Test) 1. *Annu. B. ASTM Stand.* **i,** 5–7 (2004).
8. C.B. Crane, and R.P. Gangloff, *Corrosion* 72 (2016): pp. 221–241.
9. R.H. Jones, J.S. Vetrano, and J.F. Windisch, *Corrosion* 60 (2004): pp. 1144–1154.
10. R.H. Jones, D.R. Baer, M.J. Danielson, and J.S. Vetrano, *Metall. Mater. Trans. A* 32 (2001): pp. 1699–1711.
11. M.E. Mcmahon, P.J. Steiner, A.B. Lass, and J.T. Burns, *Corrosion* 73 (2017): pp. 713–723.
12. J.L. Searles, P.I. Gouma, and R.G. Buchheit, *Metall. Mater. Trans. A Phys. Metall. Mater. Sci.* 32 (2001): pp. 2859–2867.
13. G.L. Pioszak, and R.P. Gangloff, *Metall. Mater. Trans. A Phys. Metall. Mater. Sci.* 48 (2017): pp. 4025–4045.
14. J. Seong, G.S. Frankel, and N. Sridhar, *Corrosion* 72 (2015): pp. 284–296.
15. N. Brown, P. Kramer, F. Friedersdorf, M. Schindelholz, and J. Siegel, *Corrosion* 72 (2016).
16. R.P. Gangloff, *Corrosion* 72 (2016): pp. 862–880.
17. M.C. Carroll, P.I. Gouma, M.J. Mills, G.S. Daehn, and B.R. Dunbar, *Scr. Mater.* 42 (2000): pp. 335–340.
18. M.C. Carroll, P.I. Gouma, G.S. Daehn, and M.J. Mills, *Mater. Sci. Eng. A* 319–321 (2001): pp. 425–428.
19. N.L. Sukiman, R.K. Gupta, R.G. Buchheit, and N. Birbilis, *Corros. Eng. Sci. Technol.* 49 (2014): pp. 254–262.
20. R.K. Gupta, R. Zhang, C.H.J. Davies, and N. Birbilis, *Corrosion* 70 (2014): pp. 402–413.
21. M.E. McMahon, J.R. Scully, and J.T. Burns, *Jom* 69 (2017): pp. 1389–1397.
22. M.E. McMahon, J.T. Burns, and J.R. Scully, “Metal-Rich Coating Development for Fracture

Mitigation in Al-Mg Alloys," in ECS Meet. Abstr. (2017), pp. 783–783.

23. R.G.K. D. Mizuno, *Corrosion* 69 (2013): pp. 580–592.
24. Z.Y. Chen, F. Cui, and R.G. Kelly, *J. Electrochem. Soc.* 155 (2008): p. C360.
25. Z.Y. Chen, and R.G. Kelly, *J. Electrochem. Soc.* 157 (2010): p. C69.
26. F. Cui, F.J. Presuel-Moreno, and R.G. Kelly, *Corros. Sci.* 47 (2005): pp. 2987–3005.
27. S.K. Lee, P. Lv, and D.D. Macdonald, *J. Solid State Electrochem.* 17 (2013): pp. 2319–2332.
28. M.E. McMahon, "AlMgRP Cycle Testing McMahon (WIP)" (n.d.).
29. M.E. McMahon, "ZnRP Accel Cycle Test McMahon (WIP)" (n.d.).
30. A.D. King, and J.R. Scully, *Corrosion* 67 (2011): pp. 1–22.
31. R.J. Santucci, B. Kannan, and J.R. Scully, *Corrosion* 74 (2018): pp. 96–111.
32. M. Szociński, and K. Darowicki, *Prog. Org. Coatings* 96 (2015): pp. 58–64.
33. R.N. Jagtap, P.P. Patil, and S.Z. Hassan, *Prog. Org. Coatings* 63 (2008): pp. 389–394.
34. S. Shreepathi, P. Bajaj, and B.P. Mallik, *Electrochim. Acta* 55 (2010): pp. 5129–5134.
35. R.P. Gangloff, D.C. Slavik, R.S. Piascik, and R.H. Van Stone, *Small Crack Test Methods* (1992): pp. 116–168.

Chapter 2. Effect of solution geometry and cathodic source

2.1. Abstract

The effect of atmospheric environments on the IG-SCC behavior of AA5083-H131 and AA5456-H116 was investigated using fracture mechanics-based testing, high fidelity monitoring of crack growth kinetics, and electrochemical potential measurements. The IG-SCC susceptibility was found to decrease in atmospheric environments as compared to full immersion at -0.8 V_{SCE}. Critically, the decrease in IG-SCC susceptibility was most prevalent for higher levels of sensitization and the more susceptible AA5083-H131 alloy. These results are analyzed in the context of a coupled anodic dissolution and H-embrittlement mechanism, wherein the reduction in IG-SCC susceptibility in the atmospheric environments results from cathodic limitation of the governing IG-SCC mechanism, leading to a decrease in the dissolution at the crack tip, a less aggressive crack chemistry development, and thus lower levels of H production. A close correlation between the OCP of the bulk surface and the crack growth kinetics was observed for environments without a set potential, and correlates well with known potential-dependent IG-SCC observations.

Note: One (1) peer-reviewed journal article has been published based on the work presented in this chapter, which can be accessed using the details below:

5. **P.J. Steiner**, J.T. Burns, Mechanistic Studies of Intergranular Stress Corrosion Cracking in Al-Mg Alloys under Atmospheric Exposure Conditions, CORROSION. 2018;74(10):1117-1131.
    a. Steiner contribution: primary performer, conducted experiments, analyzed data, wrote manuscript.

2.2. Introduction

As reviewed in Chapter 1, Aluminum-magnesium alloys (classified as AA5xxx series) are being increasingly utilized in marine applications due to a high strength-to-weight ratio, good weldability, and low cost[1]. These characteristics result from a combination of both work hardening and solid solution strengthening primarily via supersaturated magnesium (typically on the order of 3-5.5 wt%). The supersaturation of magnesium causes these alloys to be prone to sensitization; specifically, at elevated temperatures (40°C to 180°C) the Mg can precipitate to form a deleterious β phase (Al_3Mg_2) along grain boundaries[2,3]. This β phase is highly anodic to the parent Al matrix and will be preferentially dissolved in chloride-based electrolyte environments leading to a high susceptibility of Al-Mg alloys to intergranular corrosion (IGC) and intergranular stress corrosion cracking (IG-SCC)[4]. Prolonged inservice exposure to relatively low-temperatures (as low as ≈40°C[5,6]) has been shown to induce sensitization which leads to premature failure of 5xxx series components. Such inservice failures have motivated extensive study to understand and quantify the susceptibility of these materials to this failure mechanism. The degree to which an alloy is sensitized is traditionally reported via the ASTM G67 Nitric Mass Loss Test (NAMLT)[7], which correlates mass loss due to grain fallout during a nitic acid treatment to the amount of β phase along grain boundaries. The accuracy and application of the NAMLT value is not fully rigorous, particularly for compositions/tempers that promote matrix attack[6,8]. However this metric has engineering scale merit and serves as the leading proxy for β phase coverage, and IGC and IG-SCC susceptibility[6].

From a mechanistic perspective, sensitization induced IG-SCC has been widely studied in 5xxx series Al alloys. The effects of sensitization time and temperature[9–12], NAMLT value[6,13,14], electrolyte composition[10,15,16], electrochemical potential[5,6,11,16,17], composition[6], loading orientation[13], and temper[6] have all been considered. Substantial evidence supports a hydrogen embrittlement (HE) model that is enabled by the aggressive crack tip chemistry caused by anodic dissolution of the grain boundary β phase (and possibly the α-matrix)[2,9,10]. Specifically, dissolution of the β phase decreases the pH (via hydrolysis of Mg^{2+}) and promotes chloride ingress to maintain charge balance. This more aggressive solution can enable dissolution of the α matrix which will further acidify the crack tip (via hydrolysis of Al^{3+}); this crack tip chemistry is maintained via occlusion. Measured anodic dissolution rates are orders of magnitude lower than rates typically seen for IG-SCC, which strongly supports the presence of an additional mechanism[9]. The high pH and chloride concentration increases the overpotential for H production at the crack tip surface[5,9], therefore allowing for HE to occur. The mechanism governing HE is controversial but in the context of IG-SCC in AA5xxx alloys, it is postulated that the hydrogen produced at the crack tip is absorbed into the stress field ahead of the crack tip (and local stress fields proximate to the β particles) to cause grain boundary and/or particle-boundary interface decohesion. This process enables the higher crack growth rates than possible from a pure anodic dissolution mechanism[9].

Prominently, the bulk of the research on the IGC and IG-SCC susceptibility of AA5xxx series alloys has been performed with specimens fully immersed in an electrolyte of constant composition[5,6,9–11,13,17,18]. Furthermore, recent high fidelity linear elastic fracture (LEFM) based characterizations of IG-SCC[6,13] have reasonably been performed using a potentiostat to fix the electrochemical potential due to (1) the known/typical drift in open circuit potential over time[19], and (2) the strong dependence of IG-SCC susceptibility on the electrochemical potential[5,15]. Critically, these full immersion and potentiostatically controlled conditions may not be representative of atmospheric service conditions that are often typified by salt-spray, rain, or a deliquesced thin-film electrolyte which involve lower volumes of corrosive solution around the crack tip. There are several important aspects of realistic atmospheric environments that may deviate from testing in full-immersion of a constant electrolyte at a fixed potential. First, atmospheric conditions will often experience wetting-drying cycles; in many instances the solute mass is fixed in the electrolyte, as such the reduction of solution volume at lower relative humidity (RH) vastly increases the solution concentration. Changes in the electrolyte composition can impact parameters critical to the IG-SCC behavior, such as the electrolyte resistivity, the breakdown potential of the various microstructure phases, and the open circuit potential[15]. Second, without a potentiostat or outside source of electrochemical potential control, any anodic dissolution must be supported by cathodic current provided from elsewhere on the sample. This coupling is critically important in the context of the proposed coupled IG-SCC mechanisms where anodic dissolution enables the development of an aggressive crack chemistry that sets the conditions necessary for the H-production at the crack tip. Third, the electrolyte geometry is important in that it will govern the bulk specimen area available to provide cathodic current to support the coupled anodic dissolution/H-embrittlement damage mode. Specifically, a reduction in electrolyte volume may result in a significant ohmic drop[20,21], shortening the effective reach of the cathodic reaction over the sample surface and thus limiting the available cathodic current. *In toto*, atmospheric conditions can deviate greatly from potentiostatically controlled testing in constant composition, full immersion condition due to their impact on the cathodic/anodic reaction behaviors that control the crack chemistry development pertinent to crack tip H production.

2.2.1. Chapter objective

The overarching aim of this chapter is to generate quantitative metrics IG-SCC susceptibility (via LEFM techniques) of engineering relevant 5xxx-series alloys in atmospheric conditions; such data will inform prognosis modeling[18,22], alloy development[23–26], and mitigation strategy development[15,27]. To achieve these goals a rigorous testing methodology must be established to enable high fidelity crack monitoring, and precise control and monitoring of the atmospheric environments. This effort will specifically focus on the influence of the evolving open circuit potential and the electrolyte volume/geometry. The effect of varying electrolyte composition will be addressed in a subsequent chapter but is purposefully excluded to systematically decouple the role of varying electrolyte composition, bulk open circuit potential, and electrolyte geometry. Once rigorous protocols representative of atmospheric service conditions are established, the LEFM based IG-SCC crack growth behavior will be interpreted in the context of the measured electrochemical data collected during testing and the coupled anodic dissolution and H-embrittlement mechanism.

2.3. Experimental methods and material

2.3.1. Materials and sample prep

Two engineering relevant Al-Mg alloys, AA5083-H131 and AA5456-H116 were investigated. The sources, thicknesses, and composition of these alloys are reported in Table 2.1. The primary compositional difference between these two alloys is that AA5456-H116 contains roughly 0.5 wt% higher Mg content, with all other alloying elements remaining similar. The temper designations also indicate that both alloys have been strain hardened, with AA5083-H131 retaining 3/8 of the residual hardening and AA5456-H116 retaining 1/8[28]. This difference in strain hardening is reflected in the differing yield strengths of the two alloys, reported in Table 2.2, with AA5083-H131 exhibiting a ~45 MPa higher value. Grain size analysis on the alloys is also reported in Table 2.2 and indicates that the AA5083-H131 alloy has an average grain dimension roughly 100 µm longer in the rolling direction (L). Prior efforts using LEFM based methods to characterize these exact production lots of materials in 0.6 M NaCl at -0.8 V_{SCE} demonstrated that for a constant NAMLT level the AA5083-H131 was significantly more susceptible to IG-SCC than the AA5456-H116[6]. Additional microstructure and sensitization analysis on these alloys are detailed in the same study.

Table 2.1. Alloy temper, source, and compositional information for the two alloys used.

Alloy	**Temper**	**Source and Plate Thickness**	**Mg**	**Mn**	**Fe**	**Zn**	**Si**	**Ti**	**Cr**	**Cu**	**Al**
AA5083-Spec →			4.0-4.9	0.4-1.0	0.4	0.25	0.4	0.15	0.05-0.25	0.1	Bal
5083	H131	Alcoa 5.7 cm	4.4	0.7	0.22	0.02	0.1	0.02	0.08	0.05	Bal
AA5456-Spec →			4.7-5.5	0.5-1.0	0.4	0.25	0.25	0.2	0.05-0.20	0.1	Bal
5456	H116	Aleris 5.7 cm	5.2	0.77	0.15	0.04	0.13	0.03	0.1	0.02	Bal

Table 2.2. Ramberg-Osgood parameters utilized for all fracture mechanical J-analysis (where σ_o is the 0.2% offset yield strength and both α and n are hardening curve fitting parameters) along with grain size and directionality ratios for the two alloys used along the rolling direction (L), short transverse direction (S), and transverse direction (T).

Alloy	**Ramberg-Osgood Parameters**				**Grain Size**				**Directionality ratio**		
	σ_o (MPa)	**α**	**n**		**L-direction [μm]**	**S-direction [μm]**	**T-direction [μm]**		**L/S**	**L/T**	**T/S**
AA5083-H131	283.4	0.52	11.2		328	35	57		9.37	5.75	1.62
AA5456-H116	238.5	0.32	15.2		234	30	57		7.8	4.1	1.9

Single edge notch tensile (SENT) specimens of both alloys were machined from both plates with an S-L orientation (loading applied in S direction, crack growth in L direction) and polished to 400 grit finish. The samples have a gauge width of 17.33 mm and thickness of 6.62 mm. A 1.52 mm deep electrically discharged machined (EDM) notch was placed at the mid-point of the gauge section which aligned with the center (T/2) location in the S-direction of the plate. Samples were then sensitized at 100°C to achieve the desired NAMLT value. For AA5083-H131 samples were heated for 175 and 336 hours to achieve NAMLT values of 22 and 40 mg/cm^2, respectively. For AA5456-H116 samples were heated for 72 and 160 hours to achieve NAMLT values of 22 and 40 mg/cm^2 respectively. Prior to testing, samples were cleaned by sonication in acetone, methanol, and de-ionized (DI) water, respectively for 15 min each. A rubber butyl stop-off lacquer and vinyl electrical tape were used to mask the non-gauge section of the sample, only leaving exposed alloy 7.5 mm above and below the crack path (1.5 cm total height) unless otherwise noted.

2.3.2. Mechanical testing

All fracture tests were conducted using software-controlled, servo-hydraulic frames with active crack length feedback via the direct current potential difference (dcPD) method[29]. Potential readings were taken via copper wires (0.127 mm diameter) coated in PFA (perfluoroalkoxyalkane) spot welded 0.5±0.1 mm from the center of the EDM notch with a 6 A constant current passing through the sample. These potential readings were then taken every 30 seconds in a process reported by McMahon et al.[6,13] and converted to an instantaneous crack length using the Johnson's equation, resulting in crack growth resolution of roughly 0.5 µm[6].

Samples were loaded by means of freely rotating clevis grips, in compliance with stress intensity (K) boundary conditions[30]. They were fatigue precracked to a cumulative notch plus crack length of 2 mm at a constant K_{max} of 6 MPa√m at a stress ratio ($R = K_{min}/K_{max}$) of 0.1 and a frequency of 8 Hz. The precrack length was then extended to 2.75 mm via a decreasing K protocol from a K_{max} of 6 MPa√m to a K_{max} of 3.5 MPa√m at a stress ratio of 0.1 and a frequency of 8 Hz. At this point a 2 kN load was applied to the precracked specimens (corresponding to a K_{max} of roughly 2 MPa√m) and the testing environment was introduced; these conditions were held for 10 hr to stabilize the initial crack tip and bulk surface chemistry. Following this 10 hr hold samples were tested via slow-rising displacement at a rate corresponding to an initial dK/dt of roughly 0.25 MPa√m/hr. Tests were run until failure or the samples exhibited bulk scale plasticity.

Following test completion, linear post-processing crack length corrections were applied based on fracture surface analysis of the initial and final crack lengths. Crack growth rates were calculated from the tangent of a second order polynomial fit to 7 crack length vs time data points (akin to the protocol established for fatigue crack growth rates in ASTM E647[31]). Elastic-plastic stress intensity (K_J) analysis was also conducted using the 0.2% offset yield strength and Ramberg-Osgood constants for the alloys, derived via compressive testing and reported in Table 2.3, in compliance with previous literature[9,32,33]. A functional resolution limit due to localized (crack tip) plasticity introducing 'false' dcPD-measured crack extension was previously established for this production lot of AA5083-H131 lot and has a functional form of:[9,34]

$$\frac{da}{dt}_{False} = 5 \times 10^{-7} \cdot \exp(0.0577K) \qquad \text{(Eq. 2.1)}$$

Recent fracture mechanics experiments conducted in an inert environment (dry N_2 gas with RH < 5%) on a Ni-based superalloy using a fixed dK/dt testing protocol demonstrate that the dcPD-measured resolution limit scales linearly with dK/dt[35]. A correction protocol was then developed to subtract this 'false' da/dt contribution from measured da/dt, thereby enabling the 'true' da/dt to be determined for an experiment conducted under fixed dK/dt conditions[35]. Given that the current study utilizes testing at a fixed *displacement* rate, it is expected that dK/dt will begin to increase from the initial value of 0.25 MPa√m/hr once crack growth occurs. As such, it is incorrect to simply subtract Eq. 2.1 from measured da/dt vs. K relationships as was done in prior work[6,13,35,36] since Eq. 2.1 is only rigorously valid for dK/dt = 0.3 MPa√m/hr and therefore must be modified to incorporate an explicit dK/dt dependence. Given that the mechanistic basis for the scaling in the resolution limit is based solely on fracture mechanics principles[35,37] and is therefore nominally material-agnostic, a dK/dt dependence can be introduced into Eq. 2.1 *via* dividing the prefactor (5×10^{-7}) in Eq. 2.1 by the dK/dt for the experiment to which Eq. 2.1 was fit (0.3 MPa√m/hr)[9], yielding:

$$\frac{da}{dt}_{False} = 1.667 \times 10^{-6} \left(\frac{dK}{dt}\right) \cdot \exp(0.0577K) \qquad \text{(Eq. 2.2)}$$

In the current study, dK/dt was determined by numerically differentiating a smoothing spline fitted to the experimental K vs. time data using the Matlab curve fitting toolbox. A smoothing parameter (p) of 0.9 was utilized for fitting each individual experiment. The smoothing spline was selected for fitting the K vs. time profile due to an improved fit (quantified *via* R^2) over the entire time range relative to a power law or exponential function. An example confirming this improved fit is shown in Figure 2.1a, which demonstrates that the power law and exponential fits have difficulty capturing the data at low and high K regions, respectively. This good agreement between the smoothing spline fit and experimental K vs. time data relative to a power or exponential fit is further established by a comparison with secant and tangent-based calculations of dK/dt. The secant-calculated dK/dt represents the instantaneous slope of the K vs. time profile, while the tangent calculation for dK/dt is adapted from the 7-point polynomial approach for calculating crack growth rates in ASTM E647[31]. As shown in Figure 2.1b, the derivative of the smoothing spline fit generally captures both the secant and tangent-based dK/dt, while the derivative of the power law and exponential fits exhibit poor agreement. Note that dK/dt cannot be calculated for the first and last three experimental datapoints when the tangent approach is employed, which is why the tangent-based data are truncated relative to the fitted and secant results.

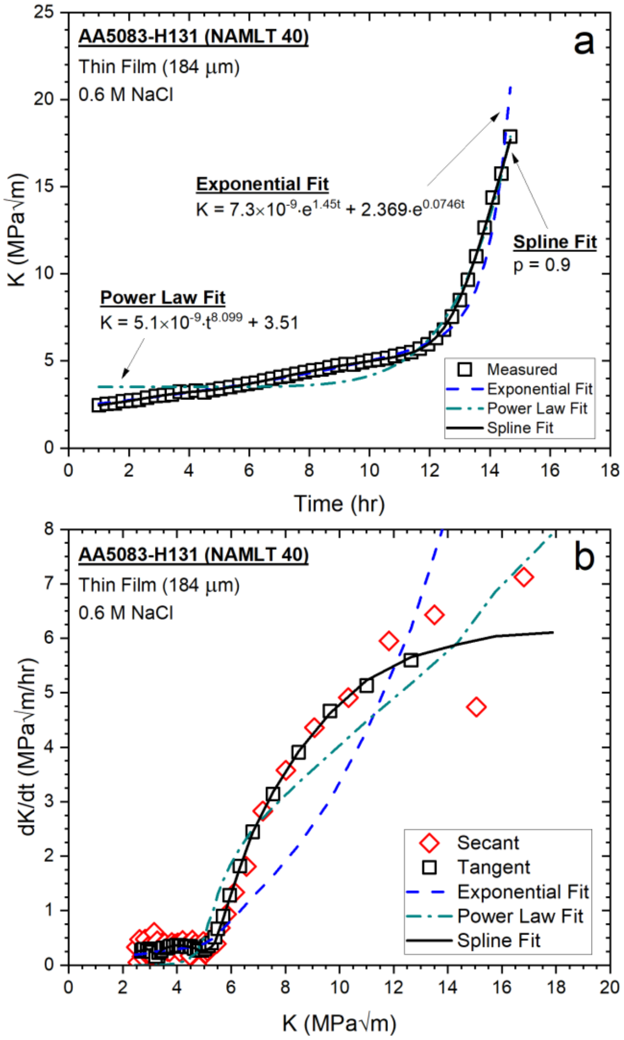

Figure 2.1. Comparison of the fit between (a) experimental K vs. time data and various fitting strategies and (b) analytically determined dK/dt vs. K data and numerical differentiation of the fitting approaches utilized in (a). The secant-based dK/dt in (b) is calculated from the instantaneous slope of the K vs time data in (a), while the tangent-based dK/dt is calculation using the 7-point polynomial approach employed in ASTM E647[31].

These data in Figure 2.1b demonstrate the importance of accounting for variable dK/dt effects on the resolution limit that are likely to arise during constant displacement rate testing. Specifically, since dK/dt in Figure 2.1b increases to »6 MPa√m/hr before the end of the experiment, this would result in a 20-fold increase in the magnitude of the 'false' da/dt relative to that predicted by the 'resolution limit' proposed by Crane *et al.*[9] Such increases in the magnitude of the false da/dt could potentially obfuscate the interpretation of subtle differences in crack growth kinetics. Once the dK/dt vs. K relationship is known, such as in Figure 2.1b, Eq. 2.2 can be utilized to calculate a test-specific resolution limit that accounts for the expected increase in dK/dt as cracking progresses. This 'false' da/dt can then be subtracted from the experimentally-measured da/dt to correct for effects of localized plasticity on the dcPD system[35]. An example of this correction scheme is shown in Figure 2.2, which demonstrates (1) the large departure in the resolution limit for a constant displacement experiment relative to that expected from Crane *et al.*[9] and (2) the general decrease in the corrected da/dt relative to the dcPD-measured da/dt.

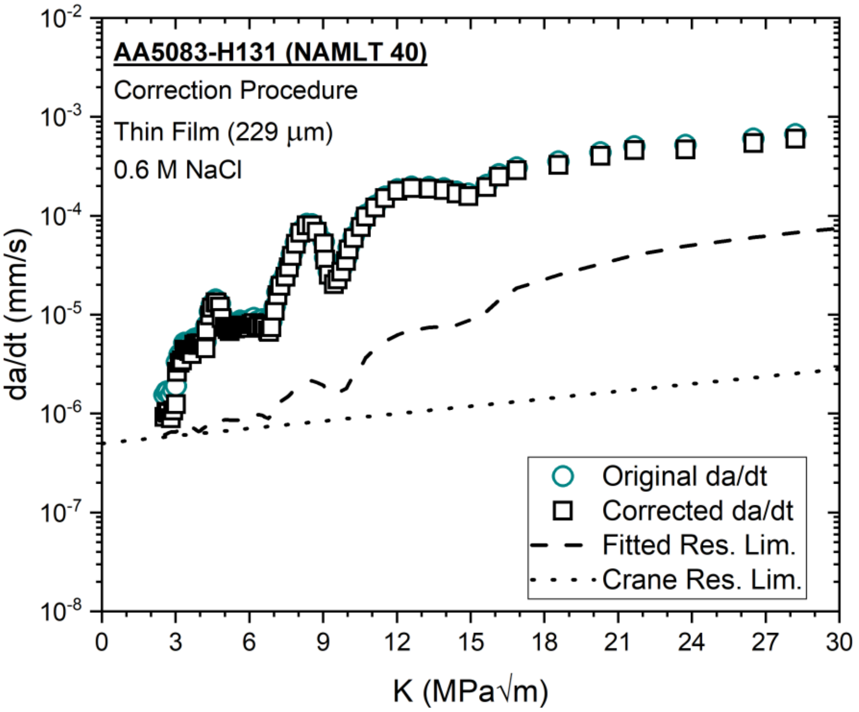

Figure 2.2. Correction procedure for removing the 'false' dcPD-measured crack growth rates attributable to localized plasticity in an experiment that exhibits a variable dK/dt. The variable dK/dt can lead to significant increases in the magnitude of the 'false' da/dt (Fitted Res. Lim.) relative to that expected for fixed dK/dt = 0.3 MPa√m/hr[9] *(Crane Res. Lim.).*

2.3.3. Environmental setup

In this chapter, three broad environmental categories were investigated: full immersion, misting, and wicked electrolyte directly into the crack. Full immersion conditions were conducted in a 200 mL Plexiglass cell, into which a 2 L reservoir of aerated 0.6 M NaCl solution at room temperature was circulated at a rate of 20 mL/min using a peristaltic pump. Two full-immersion conditions were investigated: (1) the test was run with no potential control and the open circuit potential (OCP) was allowed to float for the duration of the testing (termed FOCP in this paper), or (2) where a constant potential was set by the potentiostat. For full immersion testing with no set potential, the exposed alloy surface area was varied from 1 cm to 0.5 mm above and below the crack path (2 cm and 1 mm total height respectively). For all full immersion testing with a set potential a potentiostat was used in floating ground mode (as the specimen was grounded through the loading frame) with a platinum mesh surrounding the sample as the counter electrode and an SCE probe as the reference.

The misting protocol was designed to be representative of a constant salt-spray environment, and was thus loosely based on ASTM B117[38]. To this end a Plexiglass cell with a large radius and a sloped ceiling and floor was designed to promote air circulation and drainage of coalesced water away from the sample. Two 80° conical fine mist spray nozzles with an inner diameter of 0.35 mm were positioned at the cell perimeter on either side of the crack path and would continuously spray the sample from a 2 L reservoir of aerated 0.6 M NaCl solution at room temperature at a rate of roughly 40 mL/min. Drainage from the cell was collected and circulated back into the reservoir.

The condition wherein electrolyte was wicked directly into the crack (termed the "wicking condition") was designed to mimic when electrolyte is contained only within the crack, as may be pertinent to the point in a wet-dry cycles where the external surface is fully dry, but electrolyte remains trapped within the crack. For this condition, a wetted fiberglass wick was threaded through the sample notch, with one end located in a 100 mL input solute reservoir of aerated 0.6 M NaCl solution at room temperature and the other end leading into a separate output reservoir. This arrangement allowed the wick to act as a gravity siphon, in which electrolyte from the higher input reservoir would flow through the wick, into the notch, and into the lower output reservoir. This flow rate was not precisely measured but was estimated to be on order of 1 mL/hr. The 100 mL input reservoir would be refilled daily with fresh 0.6 M NaCl solution and would not be circulated from the output reservoir. Confirmation that the electrolyte filled the entirety of the crack (from the mouth to the tip) is supported by two observations: (1) a decrease in the observed crack length due to electrical shorting, and (2) IGC growth of the crack during a low static load (below the threshold stress intensity for IG-SCC). The first observation arises when solution in the crack tip destabilizes the electrically insulating oxide layer on the crack wake surfaces, this enables an electrical pathway due to surface contacts[29]. The resulting lower potential drop, leads to calculated crack lengths that are smaller than reality[29]. Evidence of this shorting (thus of an electrolyte wicking into the crack) is shown in Figure 2.3, where a fatigue pre-crack was performed in air then a 1 kN load hold was applied. At 1 h (solid line in Figure 2.3) the wicking of electrolyte was begun, the electrical shorting is clearly observed as evidenced by the decrease in the calculated crack size. Full entry into the electrolyte is confirmed by the subsequent rise in the crack size, which was attributed to actively growing IGC (which may be stress assisted) and is confirmed by the inset fractography in Figure 2.3. The IGC progression is dependent upon electrolyte being present at the crack tip. The combined dcPD shorting behavior and observed IGC progression conclusively establishes that the wicking procedure fully fills the crack (from the mouth to the tip) with electrolyte.

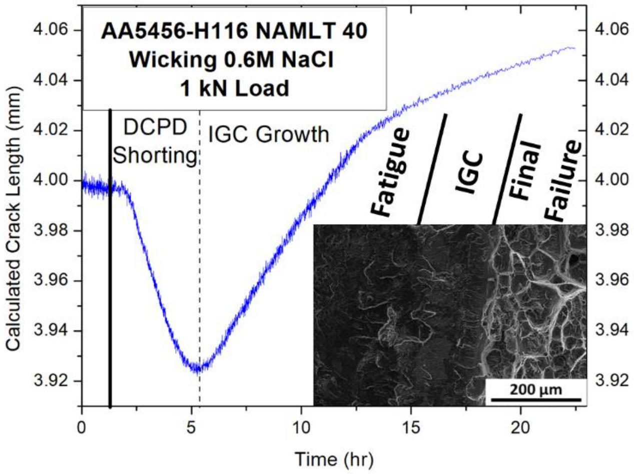

Figure 2.3. Crack tip solution verification of the wicking condition during a static 1 kN hold. Solution entering the crack tip causes shorting of the signal and a corresponding false shortening of the calculated crack length before IGC growth causes true crack tip lengthening. Fractography of the resulting surface can be seen in the bottom right showing true crack IGC growth.

2.3.4. Electrochemical monitoring

For the FOCP, misting, and wicking conditions monitoring of the OCP and control of the applied potential during testing was achieved via a 4 mm diameter sintered silver/silver-chloride probe (SSC). Details of the governing electrochemical concepts, functional details/limitations of the probe application, and verification of the probe accuracy for thin film electrochemical measurements was demonstrated by Khullar et al..[39] Notably, the probes were found to not impact the electrolyte composition, function well with currents up to 1 mA, and calculation of the ideal solution theoretical potential of these probes at 25°C in a 0.6 M NaCl solution (via the Nernst equation) reveals only a 5 mV difference (E_{SSC} = +0.236 V_{SHE}) from that of an SCE reference probe (E_{SCE} = +0.241 V_{SHE}). Confirmation of the SSC probe accuracy was performed by instrumenting a single sample (loaded at 2 kN) in full immersion 0.6 M NaCl with an SSC probe and the standard SCE monitoring system previously described. The measured values confirmed the above calculations, showing a small (~5 mV) offset that was stable over a 10 hr hold time. During immersion and misting tests the probe was placed at the bottom of the exposed window on the side opposite the EDM notch (~12 mm diagonally away from the notch tip for a 15 mm window). The probe was attached to the sample via 100 µm thick double-sided adhesive to slightly offset it from the sample surface. For wicking tests the probe was placed in the outflow reservoir roughly 5 cm down the wick path from the sample notch.

It is worth noting that in the probe configurations detailed above, distance from the crack tip to the SSC probe through thin/narrow ionic solution paths may lead to an increased electrical resistance. This can cause a change in the perceived potential due to ohmic drop, thus affecting the accuracy and validity of the SSC probe. For the wicking condition no IR drop is expected due to the lack of current flow through the wick. Conversely the effects of this probe distance were tested for the misting condition and can be seen in Figure 2.4, wherein the recorded potentials of three probes placed 0, 4, and 8 mm away from the crack path are compared. One can see that as probe distance is increased the recorded potential is also altered on the order of a few millivolts. While this is recognized as an area of concern and a potential source of error, due to the low currents involved in OCP measurements and the magnitude of the observed effects this should have a negligible consequence on the OCP interpretations in this study.

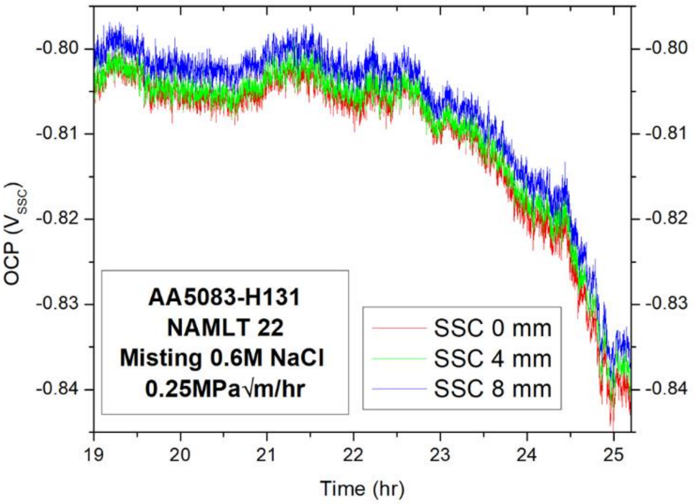

Figure 2.4. OCP vs. time graph depicting the observed gradient away from the crack path. The OCP is found to increase as the probe is placed further from the crack path.

2.4. Results

2.4.1. Influence of environment on IG-SCC kinetics

Use of the dcPD method and slow rising displacement loading protocol described above allows for detailed analysis relating the crack growth rate, da/dt, versus K_J. From these data the various stages of SCC crack growth can be determined and the IG-SCC dependent parameters derived. Traditionally the two parameters of interest are the K_{TH} and the Stage II crack growth rate (da/dt_{II}), shown visually on an example K_J vs da/dt_{II} graph in Figure 2.5. The K_{TH} is defined as the beginning of IG-SCC dominated fracture and is functionally defined as a significant increase in the slope of the da/dt vs. K_J relationship that occurs above the resolution limit[9]. The da/dt_{II} is defined as the crack growth rate which it is largely independent of increasing stress intensity; this has been postulated to be due to an H-diffusion limitation from the crack tip surface into the crack tip process zone[9,11]. This limitation causes a plateau in the da/dt vs K_J graph leading up to the K_{IC}, at which point sub-critical HEAC based cracking is augmented by a ductile failure mechanism (possibly some stable ductile tearing then final rupture). It is worth noting that scatter has been observed in the da/dt vs. K_J relationship for samples from the same lot run under the same conditions has been reported previously, thus current data should be analyzed in the context of this inherent variability.[9] While experimental complexity and material resources have limited extensive replicates, duplicates of tests have been performed where possible to address these concerns.

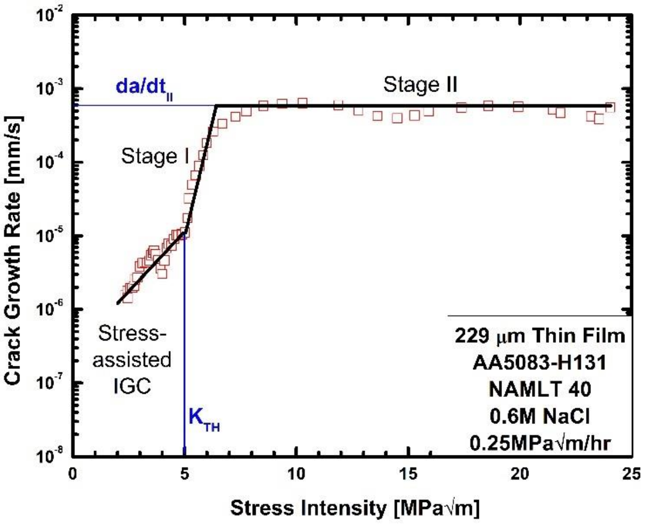

Figure 2.5. Visual representation of a typical K_J vs. da/dt graph with significant values for crack growth highlighted.

Crack growth vs stress intensity data for AA5083-H131 are reported in Figures 2.6a and 2.6b for NAMLT 22 mg/cm^2 and NAMLT 40 mg/cm^2, respectively. The full immersion condition set to -0.8 V_{SCE} exhibited the highest IG-SCC susceptibility as compared to the other environments. For both NAMLT values of 22 mg/cm^2 and 40 mg/cm^2 this condition exhibited the lowest K_{TH} (5 and 6 MPa√m, respectively) and the highest da/dt_{II} rates (2x10^{-3} and 3x10^{-3} mm/s, respectively). For the NAMLT value of 22 mg/cm^2 all atmospheric conditions are then seen to exhibit similar trends, with a K_{TH} of around 8 MPa√m and da/dt_{II} rates of around 6x10^{-4} mm/s. For the NAMLT value of 40 mg/cm^2 it is seen that the immersion FOCP 2 mm and misting condition exhibited similar susceptibility, with da/dt_{II} rates comparable to the immersion -0.8 V_{SCE} but with noticeably higher values for K_{TH} (6 and 7 MPa√m respectively). Meanwhile the immersion FOCP 1 mm and wicking condition exhibited the least IG-SCC susceptibility, with a K_{TH} values of 7 MPa√m and a da/dt_{II} of 8x10^{-4} mm/s.

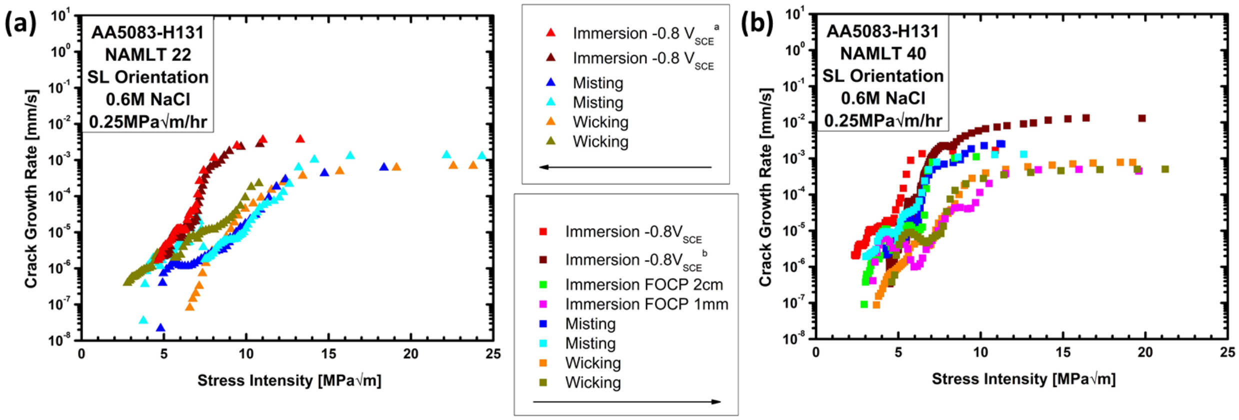

Figure 2.6. Crack growth rate versus stress intensity for AA5083-H131 in different environmental conditions at NAMLT values of (a) 22 mg/cm^2 and (b) 40 mg/cm^2. The test denoted "a" was taken from McMahon et al.[6] and the test denoted "b" was taken from Crane[40].

Due to the decreased IG-SCC susceptibility of the AA5456-H116 alloy, the net section proportional limit must be taken into consideration during slow-rising displacement testing. As higher stress intensities are required in order to initiate IG-SCC, larger loads are consequently achieved during testing. Should these loads exceed the proportional limit of the remaining sample ligament then plasticity effects will increase the electrical resistance of the sample and result in a false indication of extension in the dcPD calculated crack length. This false increase in crack length will invalidate the dcPD readings and K solution once this proportional limit has been reached, resulting in larger calculated stress intensities than actually observed. To confirm the validity of the dcPD signal until the proportional limit has been reached an AA5456-H116 NAMLT 40 sample was tested in the 0.6 M NaCl FOCP condition until the proportional limit of the alloy was reached (determined to be 140 MPa for AA5456-H116 from stress-strain plot analysis). The test was then terminated and fatigue cracked to a cumulative notch plus crack length of 9 mm at a constant K_{max} of 6 MPa√m at a stress ratio ($R = K_{min}/K_{max}$) of 0.1 and a frequency of 8 Hz. Fractography of this test can be seen in Figure 2.7, confirming the accuracy of the dcPD method until the proportional limit has been reached due to the correspondence of the calculated dcPD crack length (orange) and the actual crack front (red). Additionally, the presence of real IG-SCC growth is seen, as indicated by the intergranular morphology during the slow-rising displacement region, consistent with the proposed mechanism. To retain accuracy of the data and validity of the dcPD method all data collected past the proportional limit for AA5456-H116 will be truncated.

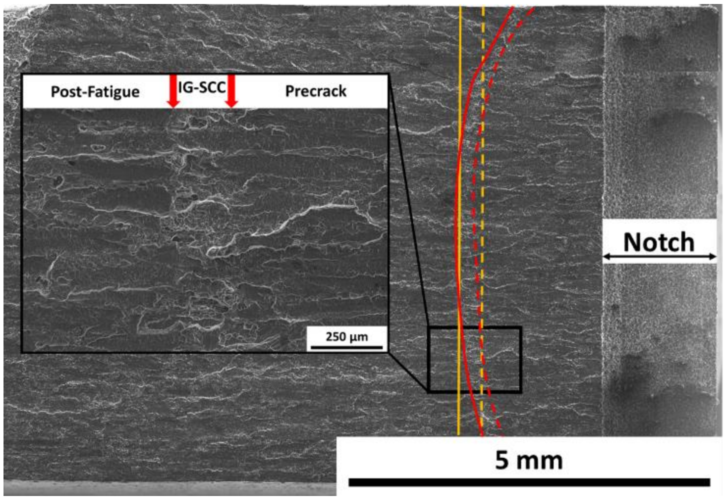

Figure 2.7. Fracture surface of AA5456-H116 NAMLT 40 in the 0.6 M NaCl FOCP condition. The dashed red line outlines the precrack front and the solid red line outlines the crack front when the proportional limit was hit (140 MPa, $K_J = 16.9$ MPa√m). The orange dashed line represents the dcPD precrack length and the solid orange line represents the dcPD crack length calculated upon reaching the proportional limit. Magnification of the slow-rising displacement region shows intergranular morphology consistent with IG-SCC.

Crack growth vs stress intensity data for AA5456-H116 are reported in Figures 2.8a and 2.8b for NAMLT 22 mg/cm^2 and NAMLT 40 mg/cm^2, respectively. The dependence on the loading environments is less substantial for the AA5456-H116 than was observed for AA5083-H131. For this alloy at a NAMLT value of 22 mg/cm^2, there was no detectable difference in the observed susceptibility for the different environments as all tests showed a K_{TH} of around 10 MPa√m. At a NAMLT value of 40 mg/cm^2 these values remain similar, except the full immersion -0.8 V_{SCE} condition which showed a lower K_{TH} of ≈7 MPa√m and a higher da/dt_{II} rate of 1x10^{-3} mm/s.

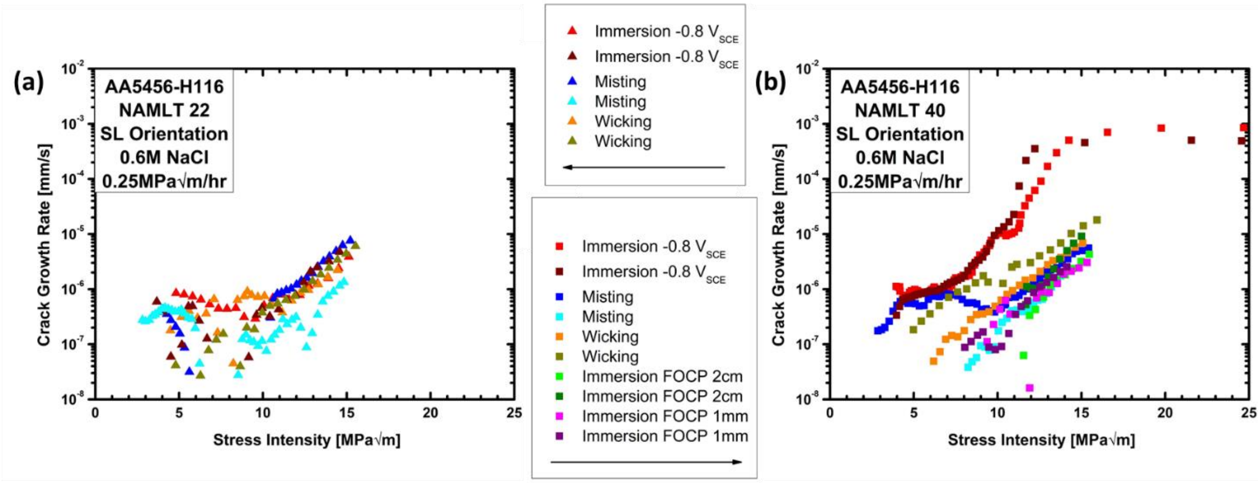

Figure 2.8. Crack growth rate versus stress intensity for AA5456-H116 in different environmental conditions at NAMLT values of (a) 22 mg/cm^2 and (b) 40 mg/cm^2.

In summary, five findings are worth noting: (1) for AA5083-H131 the full immersion condition set to -0.8 V_{SCE} exhibited the most IG-SCC susceptibility; (2) for AA5083-H131 the wicking condition exhibited the least IG-SCC susceptibility; (3) for AA5083-H131 these differences were more pronounced at the higher NAMLT value of 40 mg/cm^2; (4) for AA5083-H131 run in the immersion FOCP condition the exposed alloy area had a large effect on IG-SCC susceptibility; and (5) for AA5456-H116 there was no noticeable effect of environments on IG-SCC susceptibility except for the full immersion condition at -0.8 V_{SCE} for a NAMLT of 40 mg/cm^2.

2.4.2. Electrochemical potential observations

Electrochemical potential has been shown to have a strong correlation to the IG-SCC susceptibility of 5xxx series aluminum alloys[5,11,15], thus potential readings were taken during the tests in which no set potential was applied in an attempt to correlate trends in the OCP to the crack growth kinetics. Examples of collected OCP plots are shown in Figure 2.9 for AA5456-H116 at a NAMLT of 40 mg/cm^2 in full immersion FOCP 1 mm (Figure 2.9a), AA5456-H116 at a NAMLT of 40 mg/cm^2 in misting (Figure 2.9b), and AA5083-H131 at a NAMLT of 22 mg/cm^2 in wicking (Figure 2.9c). There are common trends that correlate to different crack growth regime: (1) a slightly negative drift in the OCP prior to the K_{TH}; (2) a more significant and constant decline in OCP during Stage I and Stage II crack growth; and (3) sharp negative spikes in the OCP occurring after the K_{IC} (taken from literature values) was exceeded with a general increase in the mean OCP. These regimes are delineated in Figure 2.9a-c by marking the K_{TH} and K_{IC} on the plots with vertical lines. Values of the OCP at the start of SCC testing (E_I), at the K_{TH} (E_{TH}), and at K_{IC} (E_{IC}) are reported in Table 2.3 for all conditions without a set potential. It must be noted that for AA5456-H116 samples portions of the OCP data are reported past when the proportional limit has been exceeded and these regions are labelled in Figure 2.9a-c. While the measured dcPD crack length and calculated stress intensities are not fully accurate in these regions, they can still provide valuable insight to the general electrochemical behavior and mechanisms.

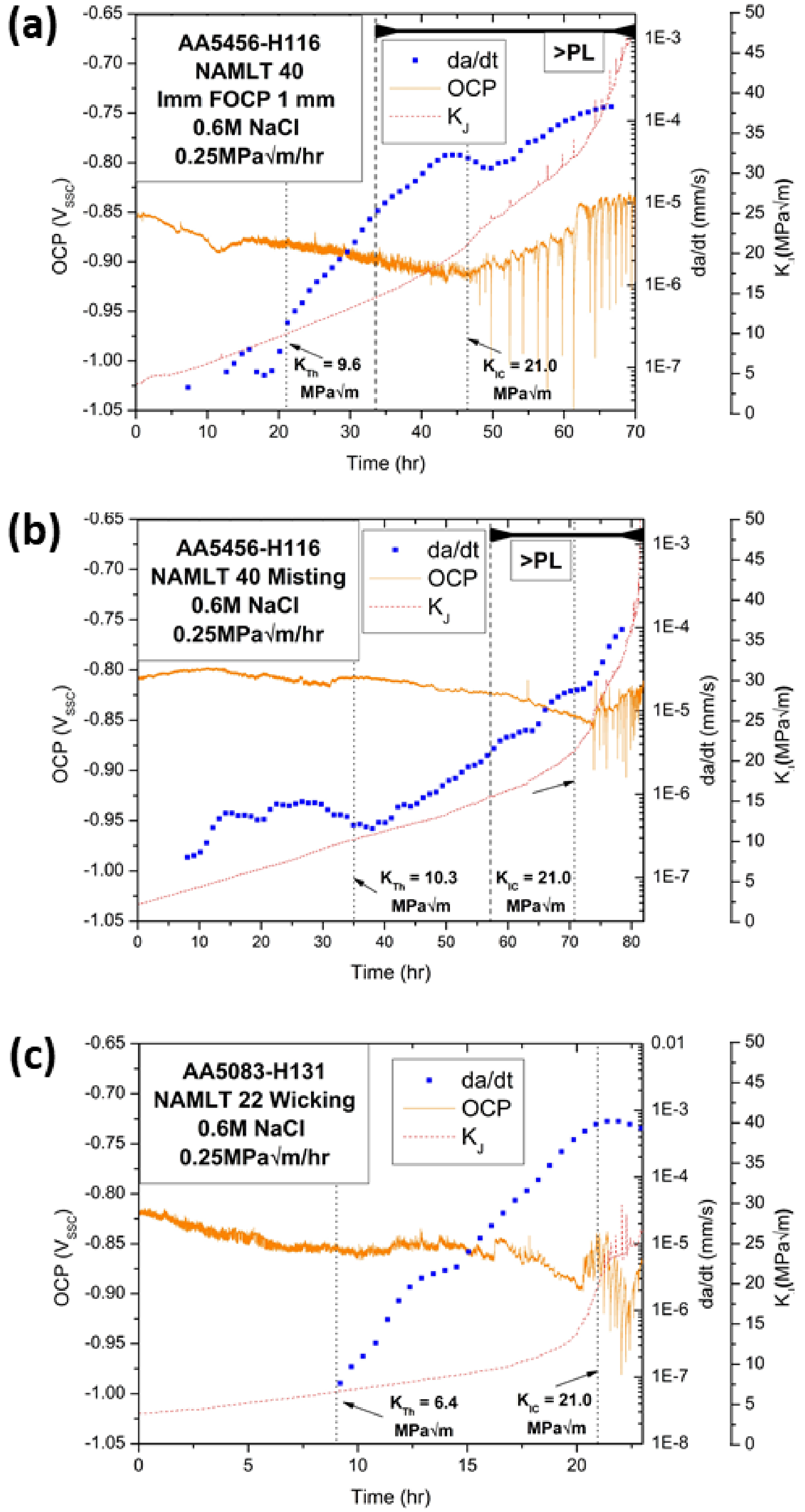

Figure 2.9. OCP (V_{SSC}), da/dt (mm/s), and K_J (MPa√m) vs time (hr) data for (a) AA5456-H116 NAMLT 40 mg/cm^2 in the immersion FOCP 1 mm condition, (b) AA5456-H116 NAMLT 40 mg/cm^2 in the misting condition, and (c) AA5083-H131 NAMLT 22 mg/cm^2 in the wicking condition. Data taken past the proportional limit (>PL) has been marked where appropriate.

Table 2.3. Values of the OCP (V_{SSC}) at the start of SCC testing (E_I), at the K_{TH} (E_{TH}), and at K_{IC} (E_{IC}) for all conditions without a set potential.

OCP Potential Values (V_{SSC})		AA5083-H131		AA5456-H116	
		NAMLT 22	NAMLT 40	NAMLT 22	NAMLT 40
Immersion FOCP 2cm	E_I		-0.85		-0.83
	E_{Th}		-0.89		-0.845
	E_{IC}		-0.9		-0.86
Immersion FOCP 1mm	E_I		-0.893		-0.84
	E_{TH}		-0.902		-0.88
	E_{IC}		-0.916		-0.91
Misting	E_I	-0.797	-0.81	-0.803	-0.807
	E_{TH}	-0.8	-0.841	-0.805	-0.809
	E_{IC}	-0.836	-0.88	-0.828	-0.852
Wicking	E_I	-0.82	-0.864	-0.765	-0.88
	E_{TH}	-0.859	-0.888	-0.798	-0.911
	E_{IC}	-0.898	-0.897	-0.871	-0.928

Further analysis of the negative spikes occurring after reaching the K_{IC} can be seen in Figure 2.10a and 2.10b. It was found that these spikes correspond directly with sudden crack extensions between collected data points (every 30 seconds), as shown in Figure 2.10a, believed to be primarily due to the combined action of stage II IG-SCC and ductile tearing as the specimen approaches non-stable final rupture. In general, larger drops in OCP tend to correlate with larger crack extensions, as shown in Figure 2.10b. Furthermore, closer inspection of the spike morphology reveals that while the spikes have a sudden sharp decrease at their initiation, their return to the resting OCP is more gradual and on the timescale of minutes rather than seconds. The correlations presented in Figure 2.10a and 2.10b clearly demonstrates a link between crack extension (thus the creation of unpassivated Al surface area) and the OCP response, however detailed examination of the coupled IG-SCC and ductile tearing mechanisms directly preceding final rupture is outside of the scope of the current study.

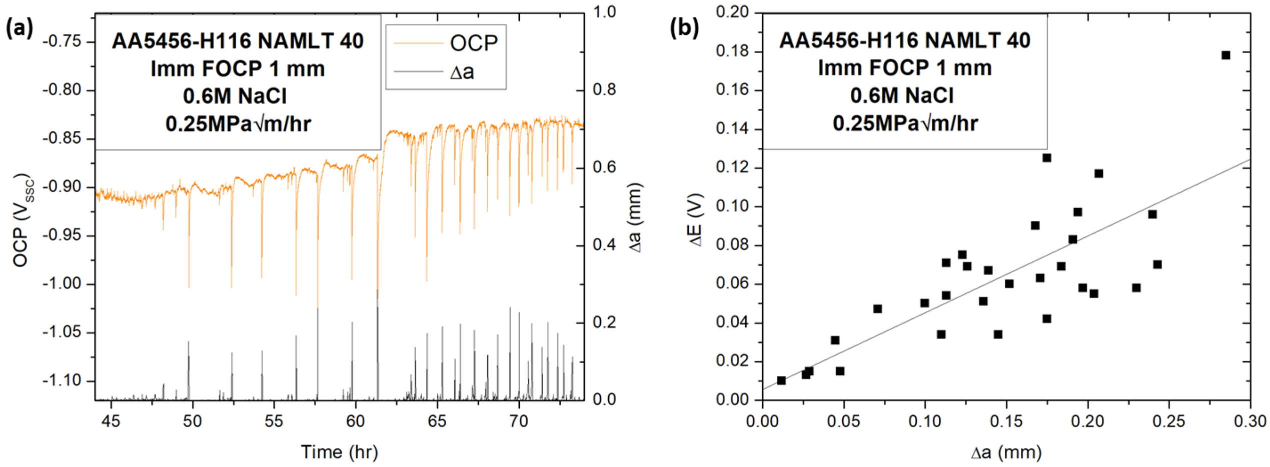

Figure 2.10. (a) OCP values (V_{SSC}) compared with Δa (mm) vs time (hr) data for AA5456-H116 NAMLT 40 mg/cm^2 in the immersion FOCP 1 mm condition. (b) Scatter plot comparing sudden crack extension growth length (Δa, mm) versus change in OCP reading (ΔE, V) for measured ductile spikes.

2.5. Discussion

From Figures 2.6 and 2.8 it is seen that despite a constant initial electrolyte composition, a difference in the IG-SCC susceptibility is observed for the different electrolyte geometries. As compared to the full immersion condition with a set potential, atmospheric conditions tend to exhibit lower IG-SCC susceptibility with the wicking condition exhibiting the least. Furthermore, larger variations are observed in the more susceptible conditions (AA5083-H131 and the higher NAMLT of 40 mg/cm^2). These results are analyzed in the context of a cathodic limitation framework, in which the anodic demand fueling the relevant IG-SCC mechanism is limited by the cathodic current the bulk surface is able to supply in the absence of an external potentiostat. As this anodic demand is higher for more IG-SCC susceptible conditions, cathodic limitation is thus more prevalent and will have a larger effect. Additionally, implications of this cathodic limitation framework are used to explain the observed trends in the OCP behavior during atmospheric testing, most notably the decrease in potential during Stage I and Stage II crack growth.

2.5.1. Role of cathodic limitation in atmospheric environments

It is useful to consider the IG-SCC susceptibility trends and corresponding shifts in measured OCP values in the context of the proposed coupled anodic dissolution and HEAC based mechanisms for cracking[5,6,9,10,13]. Specifically, H-production at the crack tip causes embrittlement and is enabled by the development of an aggressive crack tip chemistry[5,9]. This chemistry is set by the anodic dissolution of the intergranular β phase (and α-matrix) at exposed grain boundaries and requires an equal and complementary cathodic current supply. For potentiostat controlled testing, there is nominally an "infinite" cathode that will supply the necessary current in order to maintain the constant electrochemical potential. For testing without potentiostat control or an external cathode, however, the cathodic current must be supplied from elsewhere on the specimen surface. This limitation has been observed in atmospheric IGC studies (such as the pitting of stainless steel[20]) where the area surrounding the corrosion site acts as the cathode for the required anodic reactions. It was also shown that the distance over which this cathode can supply the necessary current was found to be critically dependent on the volume and geometry of the solution[20]. This arises from the associated ohmic drop accompanying the narrower and longer ionic paths. Therefore in atmospheric environments, where there are limited solution volumes, cathodic limitation can potentially stifle the anodic dissolution of the β phase, which precludes the development of the aggressive crack tip chemistry and retards the IG-SCC crack growth rates.

The effects of this cathodic source transfer can be clearly seen in in the crack growth kinetics for AA5083-H131 (Figure 2.6a and 2.6b). In the full immersion condition, for a fixed potential of -0.8 V_{SCE} high susceptibility is observed (the lowest K_{TH} values and the highest da/dt_{II} rates). This result is hypothesized to be due to the constant cathodic supply from the potentiostat, which provided sufficient cathodic current to enable unimpeded anodic dissolution at the crack tip. As previously discussed, the anodic dissolution enables the development of the crack tip chemistry necessary for the H-production that governs the IG-SCC mechanism. For the full immersion FOCP 2 cm and the misting conditions there is a modest decrease in susceptibility (the K_{TH} increases noticeably and da/dt_{II} slightly decreases) as compared to the full immersion potentiostatically controlled condition. Two aspects of this change are notable. First, the reduction in susceptibility suggests that the cathodic current supplied by the specimen surface is reduced as compared to the "unlimited" cathodic current supply from the potentiostat. Second, the fact that the FOCP 2 cm and the misting conditions are similar suggests that the reduction in solute volume/thickness (thus the increased solution resistance) for the misting environment does not sufficiently reduce the interaction area on the bulk surface able to supply the cathodic current. Further reduction in susceptibility (increase of the K_{TH} and decrease of the da/dt_{II}) occurs in both the wicking and the FOCP 1 mm environmental conditions. In the case of the FOCP 1mm environmental condition the cathodic interaction area (despite a high solution volume) is physically limited by masking the bulk surface, whereas in the wicking condition the interaction area is limited to within the crack due to the targeted insertion of the electrolyte within the crack. Achieving near identical IG-SCC susceptibility via bulk specimen masking and targeted electrolyte insertion strongly supports the catholic limitation hypothesis.

All of these trends are more pronounced at the higher NAMLT level of 40 mg/cm^2 due to the increased anodic demand resulting from larger quantities of β phase on the grain boundaries, causing cathodic limitation effects to have greater consequence. For the AA5456-H116 alloy the same effects observed for AA5083-H131 are not seen and no significant change is observed between any of the immersion FOCP or atmospheric conditions. Due to the similarities in IG-SCC kinetics between the immersion FOCP and atmospheric conditions, it is unlikely that solution geometry or exposed surface area had any discernable effect of cathodic limitation for this alloy. This result is most likely explained by the increased IG-SCC resistance of this alloy resulting in less anodic current being required to fuel the IG-SCC mechanism, thus all cathodic systems are able to provide the diminished anodic demand despite cathodic availability.

2.5.2. Correlation between electrochemical potential and IG-SCC mechanisms

The electrochemical potential trends are directly correlated to the IG-SCC crack growth kinetics behavior for each of the non-potentiostat controlled test environments, as clearly shown in Figure 2.9a-c. This correlation can be understood based on simple mixed-potential theory (coupling the crack tip and the bulk/crack wake surfaces) and assuming that the cathodic kinetics are fixed for a single environmental condition. Simply put, in order to supply higher levels of anodic current at the crack tip, the potential on the bulk surface must adjust. Such an increase in demand for anodic current could be due to either an increase in the crack tip activity and/or an increase in the crack tip area. The latter would be the case during crack progression where crack advance exposes fresh and unpassivated crack tip area (both matrix and β-phase) which is prone to dissolution thus requires an increase demand for anodic current. The demand for anodic current will continually be increasing as the da/dt increases due to larger increments of crack advance. This process is shown schematically in Figure 2.11 on an Evans diagram plot of potential versus total current, the cathodic oxygen reduction reaction (ORR) kinetics on the external surface are plotted (and assumed constant) along with the anodic kinetics at the crack tip (assuming the stabilized aggressive chemistry has developed). At time-step 1 the crack has not begun to propagate, as the crack begins to propagate (time-step 2) there is in an increase in the crack tip area, thus the total current shifts to the right (assuming constant activity); further increases in crack propagation rate (time-step 3) results in a further shift. While this simple paradigm neglects any changes in the crack chemistry that would also alter the anodic activity, IR drop down the crack, and changes in the ORR kinetics[41], these complicating factors do not invalidate the qualitative conceptual framework for interpreting the trends in Figure 2.9.

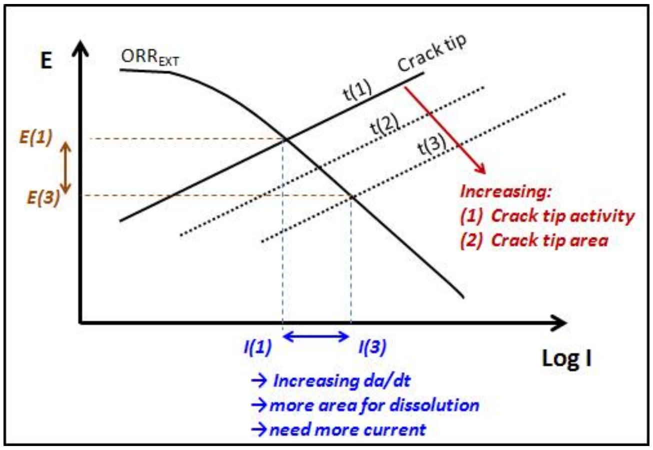

Figure 2.11. Evans diagram schematic showing the correlation between anodic current demand and cathodic potential. As crack tip activity and area increases a growing demand for current causes the cathodic reaction potential on the bulk sample surface to decrease to supply the required current for the IG-SCC mechanisms.

The paradigm above can be used to interpret each of the behavioral trends observed in Figure 2.9. During the initial stage of the test, in which the stress intensity is below the K_{TH} and IG-SCC growth is not present, there is a slight cathodic drift in the OCP to lower values with a high degree of variability. This is typical of OCP measurements and may be associated with IGC behavior and/or the development of the local aggressive crack tip chemistry which would require more current from the external cathode. Once the K_{TH} is exceeded and IG-SCC growth starts, the OCP shows much less variation and exhibits a constant, generally steady decrease. This is consistent with the mixed-potential based mechanism proposed above, specifically crack growth exposes increased area for dissolution, thus a higher demand for anodic current, this demand is met by a decrease in the potential to provide the matching cathodic current. As the IG-SCC growth rates increase, the demand increases proportional to increment of crack extension, which drives the bulk surface potential to more cathodic values. This steady decrease in the potential halts at roughly the point where the K exceeds the K_{IC}, at which point the potential data exhibits erratic behavior including the sharp spikes reported in Figure 2.10 and a general increase in the mean OCP. Full interpretation of the erratic potential behavior and general increase in the mean OCP in the regime where the specimen is experiencing the onset of bulk-scale plasticity, coupled contributions of both IG-SCC and ductile tearing, and near to the final failure regime is outside of the scope of the current effort. However, this behavior is speculated to be due in part to the transition from an intergranular dominated SCC cracking mechanism to a transgranular ductile mechanism. As a transgranular mechanism would expose less of the anodic β-phase primarily populating the grain boundaries a general decrease in the anodic demand could be expected. While this postulation requires further study and confirmation, it is useful to discuss the sharp negative spikes observed in Figure 2.9 and 2.10. Plotting the OCP and the change in crack length (Δa) versus the time, it is clear there is a close correlation of these spikes to the occurrence of sudden large crack extensions. This behavior is fully consistent with the mixed-potential based mechanism where large crack extensions (likely due to a mechanically induced mechanism) provide a sharp increase in newly exposed crack surface. The freshly exposed surface will be susceptible to dissolution in the aggressive crack tip chemistry, which will result in a large and immediate anodic current demand. This anodic demand increase will cause a large decrease in the bulk surface potential to provide the necessary balancing cathodic current. As expected the occurrence of larger potential spikes result from larger crack extensions, which would involve larger anodic demand due to larger exposed areas.

One last trend remains to be justified, and that is the difference in IG-SCC susceptibilities seen between the full immersion experiments run at -0.8 V_{SCE} and the FOCP 2cm where there is extensive bulk surface area available. This stark difference is clearly seen for NAMLT 40 mg/cm^2 in AA5456-H116 in Figure 2.8b and AA5083-H131 in Figure 2.6b. As the solution configurations are identical, cathodic limitation via solution geometry cannot be controlling this discrepancy. It is therefore proposed that this difference results solely from the change in bulk surface potential associated with the removal of the controlling potentiostat and the limited cathodic kinetics on aluminum alloy surfaces. Analysis of the values in Table 2.3 show that during tests with no set potential the measured OCP is seen to be decrease from -0.8 V_{SCE} to ~-0.9 V_{SCE} during the IG-SCC propagation. While this drop in potential is necessary to support the demand for anodic current at the crack tip, the shift in bulk potential to more negative values will retard the IG-SCC mechanism[5,15]. Specifically, recent work on both the current lots of AA5083-H131 and AA5456-H116 have demonstrated that decreasing the bulk potential will lead to a less aggressive local crack tip chemistry by shifting the crack tip potential to values below the breakdown potentials of the β (~1.0 V_{SCE}) and α (~0.9 V_{SCE}) phases[5,15]. Although measured potentials for atmospheric environments are not sufficiently cathodic to prevent dissolution of the β phase from occurring (thus the mitigation of IG-SCC) retardation of α phase dissolution is most likely taking place to decrease IG-SCC growth rates.

2.5.3. Potential based verification of the cathodic limitation hypothesis

Several aspects of the data presented above strongly suggest that electrolyte geometry induced cathodic limitation can occur for some 5xxx-series alloys, NAMLT levels, and environmental conditions. First, the correlation between the crack growth kinetics and the measured OCP values clearly suggests that the bulk surface is the source of the cathodic current that balances the anodic processes at the crack tip. Second, the fact that the FOCP 2 cm growth rate data is decreased as compared to the potentiostatic controlled -0.8 mV_{SCE} data demonstrates that the bulk surface is unable to support the same level of crack tip anodic dissolution. Furthermore, the slower growth rates are consistent with the more cathodic measured OCP values of -0.8 to -0.9 V_{SCE} (Table 2.3); prior work has demonstrated that IG-SCC susceptibility is decreased at more cathodic potentials[5,15]. Third, the strong decrease in growth rates observed for the 5083-H131 in for the FOCP 1 mm and wicking environments (Figure 2.6) suggest that as the available area to support the cathodic reaction is reduced the IG-SCC susceptibility is decreased. Fourth, the exact correspondence between the FOCP 2 cm and the misting data suggest that the water layer thickness associate with the misting condition (likely ≈140 µm based on ASTM B117 testing with an EIS device detailed in Chapter 3) is sufficiently large to not result in a strong increase in resistance, thus minimally effects the available bulk surface interaction areas. Fifth, material conditions that are more susceptible to IG-SCC (e.g higher NAMLT values, and AA5083-H131) show the highest sensitivity to the atmospheric environments. This result is reasonable considering that materials with a higher susceptibility will have a higher demand for anodic current, thus will be more strongly influenced by a cathodic limitation mechanism.

To confirm the important role of potential and cathodic availability for atmospheric conditions, AA5456-H116 was tested at a NAMLT value of 40 mg/cm^2 in the misting and wicking environments with the potential set to -0.8 V_{SSC} via use of the SSC probe. Critically, these experiments in part isolate the effect of electrolyte geometry and the degree of polarization. The results, shown in Figure 2.12, show that these polarized wicking and misting environments generally exhibit a lower K_{TH} and higher da/dt$_{II}$ rates as compared to their accompanying atmospheric tests at OCP conditions. However, these conditions still resulted in a lower susceptibility than was observed for the full immersion conditions at -0.8 V_{SCE}. The difference between the polarized tests in full immersion and in the polarized misting and wicking environments is likely due to IR drop from the SSC probe placement in relation to the crack tip, as discussed previously in the methods section for SSC probe application. This lower susceptibility may also explain the observed increased variability in the polarized misting condition tests, as probe placement was found to have a higher influence on electrochemical readings. Regardless this data clearly demonstrates that independent of the electrolyte geometry that an externally applied potential can produce higher levels of susceptibility.

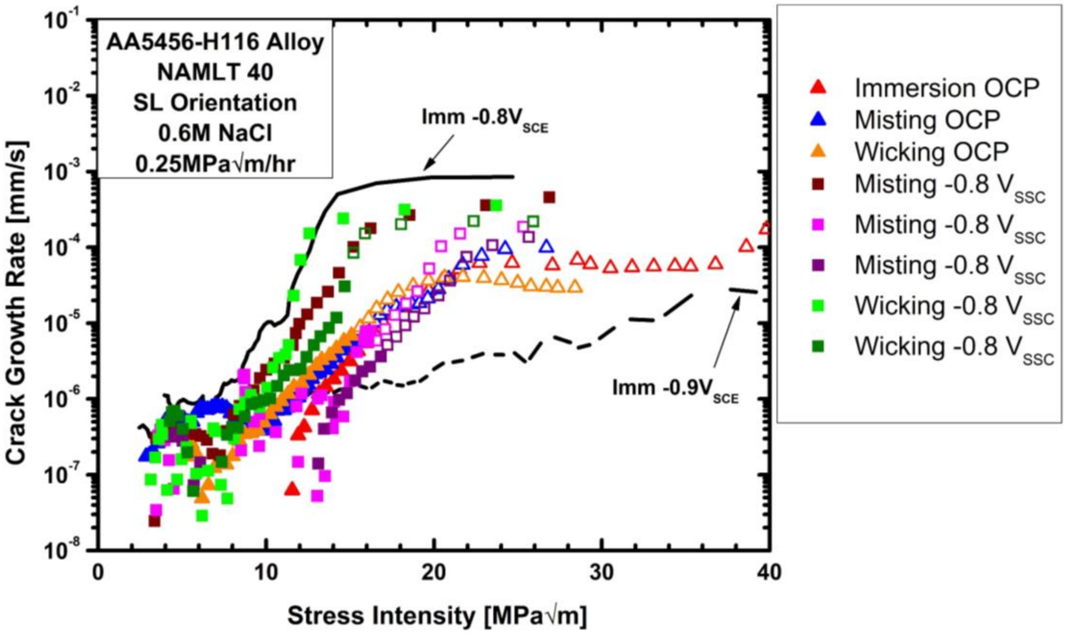

Figure 2.12. Crack growth versus stress intensity plot for AA5456-H116 NAMLT 40 mg/cm^2 at various environmental conditions with both controlled and floating electrochemical potentials. Data recorded past the proportional limit are indicated by hollow symbols.

In further concurrence with the role of cathodic limitation, cathodic current readings taken during the polarized atmospheric tests show similar trends to that of the potential readings taken for the OCP tests. This result agrees with the proposed mechanism as cathodic current demanded by increasing IG-SCC rates should be directly linked to the bulk surface potential drop seen in cathodically limited environments, as explained above. Therefore, trends seen in the potential during an OCP test should also be observed in the cathodic current demand for a polarized test. This effect can be seen in Figure 2.13, where cathodic current readings were taken during one of the AA5456-H116 NAMLT 40 mg/cm^2 misting tests polarized to -0.8 V$_{SSC}$. Similar to OCP tests, the applied current was found to slightly drift with a high degree of variability prior to reaching the K$_{TH}$, at which point a steady increase in the magnitude of the current was observed during IG-SCC growth. This behavior is as expected. As the crack accelerates, its demand for current requires the potentiostat via SSC to provide more current in order to maintain the external potential at the set value. Upon reaching the K$_{IC}$ of the material the sharp spikes are also observed, once again matching up directly with any sudden large crack extensions, as seen in Figure 2.14a, with larger crack extensions generally leading to larger changes in current, as seen in Figure 2.14b.

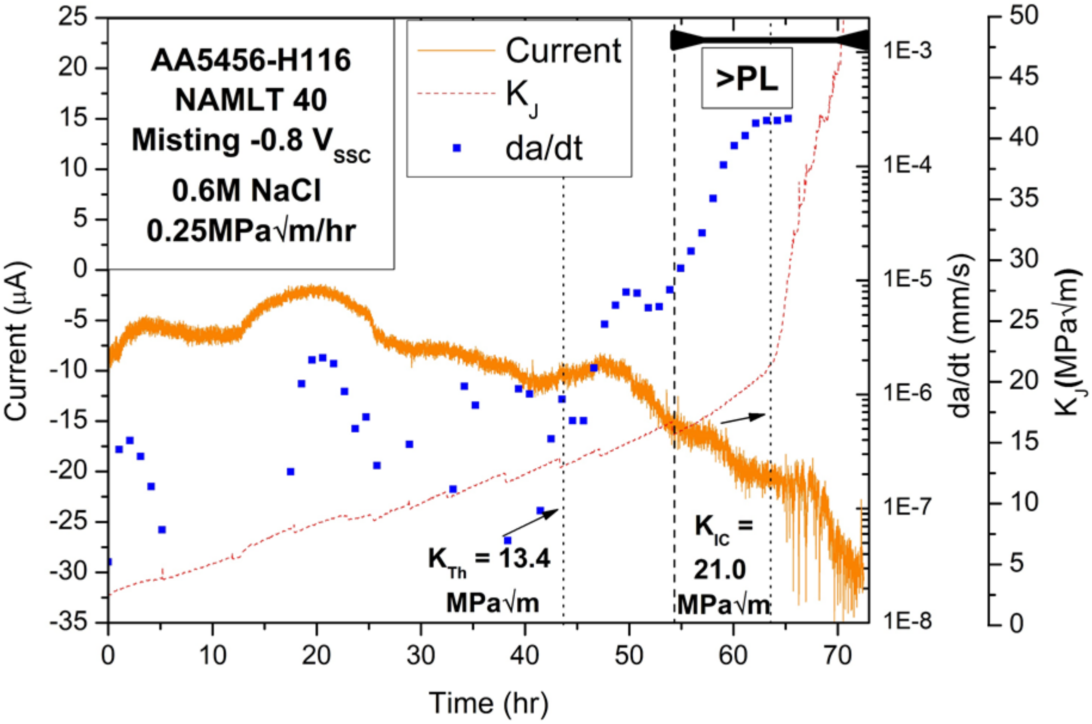

Figure 2.13. Current (μA), da/dt (mm/s), and K_J (MPa√m) vs time (hr) data for AA5456-H116 NAMLT 40 mg/cm^2 in the misting condition with a set potential of -0.8 V_{SCC}. Data taken past the proportional limit (>PL) has been marked where appropriate.

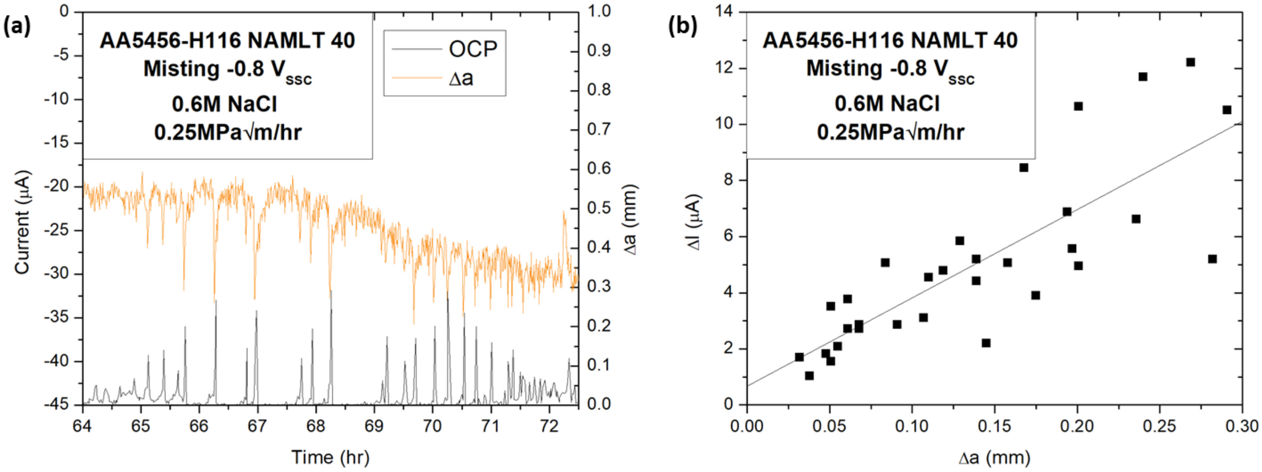

Figure 2.14. (a) Current (μA) compared with Δa (mm) vs time (hr) data for AA5456-H116 NAMLT 40 mg/cm^2 in the misting condition set to -0.8 V_{SSC}. (b) Scatter plot comparing sudden crack extension growth length (Δa, mm) versus change in current reading (ΔA, μA) for measured ductile spikes.

2.6. Conclusions

The intergranular stress corrosion cracking susceptibility of AA5083-H131 and AA5456-H116 alloys sensitized at 100°C to NAMLT values of 22 mg/cm^2 and 40 mg/cm^2 were assessed in various full-immersion and atmospheric environments (misting and wicking) in 0.6 M NaCl with no set potential. Tensile testing was performed with high-resolution crack growth monitored using the dcPD method and constantly replenished environments with 0.6 M NaCl solution. All subcritical crack growth data were analyzed using the elastic-plastic K_J. Novel use of a sintered silver/silver chloride probe allowed for in-situ electrochemical potential measurements and polarization in these atmospheric environments. The following conclusions are established:

- For a constant electrolyte composition, AA5083-H131 and AA5456-H116 testing in atmospheric environments showed decreased IG-SCC susceptibility as compared to full immersion experiments with a set -0.8 V_{SCE} potential.
- Fluctuations in the OCP of the bulk surface directly correlated with trends in the crack growth kinetics for environments (full immersion, misting, and wicking) without a set potential.
- Retarded crack growth kinetics are attributed to cathodic limitation of the governing IG-SCC mechanism and correlate with known potential-dependent IG-SCC observations.
- Changes in solution composition and variability of the atmospheric environment (wet/dry cycles) were not considered and may have additional effects in practical applications.

2.7. Acknowledgements

This research was financially supported by the Office of Naval Research with Dr. Airan Perez as the Scientific Officer. Professor R.G. Kelly has also provided valuable insight into the development of these atmospheric environments and interpretation of the results.

2.8. References

1. N.J.H. Holroyd, and G.M. Scamans, *Corrosion* 72 (2016): pp. 136–143.
2. D.R. Baer, C.F. Windisch, M.H. Engelhard, M.J. Danielson, R.H. Jones, and J.S. Vetrano, *J. Vac. Sci. Technol. A Vacuum, Surfaces, Film.* 18 (2000): pp. 131–136.
3. R. Goswami, G. Spanos, P.S. Pao, and R.L. Holtz, *Mater. Sci. Eng. A* 527 (2010): pp. 1089–1095.

4. G.M. Scamans, N.J.H. Holroyd, and C.D.S. Tuck, *Corros. Sci.* 27 (1987): pp. 329–347.
5. C.B. Crane, R.G. Kelly, and R.P. Gangloff, *Corrosion* 72 (2016): pp. 242–263.
6. M.E. Mcmahon, P.J. Steiner, A.B. Lass, and J.T. Burns, *Corrosion* 73 (2017): pp. 347–361.
7. Standard Test Method for Determining the Susceptibility to Intergranular Corrosion of 5XXX Series Aluminum Alloys by Mass Loss After Exposure to Nitric Acid (NAMLT Test) 1. *Annu. B. ASTM Stand.* **i,** 5–7 (2004).
8. M.E. McMahon, R.L. Haines, P.J. Steiner, J.M. Schulte, S.E. Fakler, and J.T. Burns, *Corros. Sci.* 169 (2020): p. 108618.
9. C.B. Crane, and R.P. Gangloff, *Corrosion* 72 (2016): pp. 221–241.
10. R.H. Jones, J.S. Vetrano, and J.F. Windisch, *Corrosion* 60 (2004): pp. 1144–1154.
11. R.H. Jones, D.R. Baer, M.J. Danielson, and J.S. Vetrano, *Metall. Mater. Trans. A* 32 (2001): pp. 1699–1711.
12. R. Goswami, G. Spanos, P.S. Pao, and R.L. Holtz, *Metall. Mater. Trans. A* 42 (2011): pp. 348–355.
13. M.E. Mcmahon, P.J. Steiner, A.B. Lass, and J.T. Burns, *Corrosion* 73 (2017): pp. 713–723.
14. K. Williams, R. Bayles, P.M. Natishan, and D.D. Macdonald, *ECS Trans.* 50 (2013): pp. 449–455.
15. M.E. McMahon, J.R. Scully, and J.T. Burns, *Jom* 69 (2017): pp. 1389–1397.
16. S.K. Lee, P. Lv, and D.D. Macdonald, *J. Solid State Electrochem.* 17 (2013): pp. 2319–2332.
17. J.L. Searles, P.I. Gouma, and R.G. Buchheit, *Metall. Mater. Trans. A Phys. Metall. Mater. Sci.* 32 (2001): pp. 2859–2867.
18. G.L. Pioszak, and R.P. Gangloff, *Metall. Mater. Trans. A Phys. Metall. Mater. Sci.* 48 (2017): pp. 4025–4045.
19. R.G.K. D. Mizuno, *Corrosion* 69 (2013): pp. 580–592.
20. Z.Y. Chen, and R.G. Kelly, *J. Electrochem. Soc.* 157 (2010): p. C69.
21. F. Cui, F.J. Presuel-Moreno, and R.G. Kelly, *Corros. Sci.* 47 (2005): pp. 2987–3005.
22. R.P. Gangloff, *Corrosion* 72 (2016): pp. 862–880.
23. M.C. Carroll, P.I. Gouma, M.J. Mills, G.S. Daehn, and B.R. Dunbar, *Scr. Mater.* 42 (2000): pp. 335–340.

24. M.C. Carroll, P.I. Gouma, G.S. Daehn, and M.J. Mills, *Mater. Sci. Eng. A* 319–321 (2001): pp. 425–428.

25. N.L. Sukiman, R.K. Gupta, R.G. Buchheit, and N. Birbilis, *Corros. Eng. Sci. Technol.* 49 (2014): pp. 254–262.

26. R.K. Gupta, R. Zhang, C.H.J. Davies, and N. Birbilis, *Corrosion* 70 (2014): pp. 402–413.

27. M.E. McMahon, J.T. Burns, and J.R. Scully, “Metal-Rich Coating Development for Fracture Mitigation in Al-Mg Alloys,” in ECS Meet. Abstr. (2017), pp. 783–783.

28. M.L.C. Lim, R.G. Kelly, and J.R. Scully, *Corrosion* 72 (2016): pp. 198–220.

29. R.P. Gangloff, D.C. Slavik, R.S. Piascik, and R.H. Van Stone, *Small Crack Test Methods* (1992): pp. 116–168.

30. H. Tada, P. Paris, and G. Irwin, “The Stress Analysis of Cracks Handbook” (St. Louis, MO: Paris Productions Incorporated, 1985).

31. E647-15e1. Standard Test Method for Measurement of Fatigue Crack Growth Rates. *ASTM B. Stand.* 1–49 (2016). doi:10.1520/E0647-15E01.2

32. T. Anderson, “Fracture Mechanics: Fundamentals and Applications,” 3rd ed. (Boca Raton, FL: CRC Press, 2005).

33. V. Kumar, M.D. German, and C.F. Shih, “An Engineering Approach for Elastic-Plastic Fracture Analysis” (1981).

34. C.B. Crane, R.G. Kelly, and R.P. Gangloff, *Corrosion* 72 (2016): pp. 242–263.

35. Z.D. Harris, E.M. Dubas, A.S. Popernack, B.P. Somerday, and J.T. Burns, *Theor. Appl. Fract. Mech.* (n.d.): p. in review.

36. P. Steiner, and J. Burns, *ICF 2017 - 14th Int. Conf. Fract.* 1 (2017): pp. 566–567.

37. R.P. Gangloff, H.M. Ha, J.T. Burns, and J.R. Scully, *Metall. Mater. Trans. A* 45 (2014): pp. 3814–3834.

38. ASTM International, *Water* 03 (2003): pp. 1–15.

39. P. Khullar, J. V. Badilla, and R.G. Kelly, *ECS Electrochem. Lett.* 4 (2015): pp. C31–C33.

40. C.B. Crane, “Validation of the Coupled Dissolution-Hydrogen Embrittlement Mechanism of IGSCC in Low Temperature Sensitized AA5083-H131,” University of Virginia, 2013.

41. K.R. Cooper, and R.G. Kelly, *Corros. Sci.* 49 (2007): pp. 2636–2662.

Chapter 3. Effect of thin film water layer thickness

3.1. Abstract

The effect of thin film environments on the intergranular stress corrosion cracking (IG-SCC) behavior of AA5083-H131 was investigated using fracture mechanics-based testing, high-fidelity monitoring of crack growth, and electrochemical potential measurements. A protocol for conducting thin film IG-SCC fracture mechanics experiments with anodized aluminum oxide (AAO) membranes is developed and the ability to maintain films of specific thicknesses without impeding oxygen diffusion during testing is validated *via* EIS testing and computational modelling. The IG-SCC susceptibility was found to increase once a critical thin film thickness of 82 µm was achieved; above this thickness a dual IG-SCC susceptibility behavior was observed. These results are analyzed in the context of a coupled anodic dissolution and hydrogen (H) embrittlement mechanism, where susceptibility is found to scale with the cathodic limitation of the governing IG-SCC mechanism. Specifically, thinner film thicknesses lead to a decrease in the dissolution at the crack tip, a less aggressive crack chemistry development, and thus lower levels of H production. A close correlation between the open circuit potential of the bulk surface and the crack growth kinetics was also observed, consistent with trends reported in previous IG-SCC studies on this alloy.

3.2. Introduction

The IG-SCC behavior of Al-Mg alloys in atmospheric environments is of particular interest to marine superstructure applications where in-service conditions are characterized by decreased solution volumes and increased solution ion concentrations. These atmospheric environments are typically formed via sea spray or deliquescence of saline solutions on the alloys surface, resulting in either discrete droplets or a thin continuous salt film across the sample surface. The thickness and uniformity of the droplets/film created are dependent on many different variables, such as surface condition, relative humidity, temperature, and dissolved species present. These factors can critically impact the corrosion rates as the water layer thickness has been shown to directly affect the available cathodic current in electrochemical studies[1–3]. Therefore, accurate determination and control of the water layer thickness is of paramount concern in any study characterizing the effects of thin film atmospheric environments.

The two primary ways in which the thickness of the water layer can impact the available cathodic current are by affecting the solution ohmic resistance and the oxygen diffusion kinetics[3]. Due to the limited dimensions of the electrolyte films in thin film environments, currents passing through the film can be subjected to substantial ohmic drops. In cases with localized corrosion sites, such as pitting, this ohmic drop can bound the size of the supporting cathodic area and limit the available cathodic current and corrosion rates[1,2]. These effects are enhanced for lower solution geometries and less conductive electrolytes. Conversely, lower thin film thicknesses can result in smaller oxygen diffusion layers and increased oxygen uptake on the sample surface. Research by Tomashov indicated four distinct regimes of reaction control due to film thickness, with control shifting from diffusion layer control in full immersion and thick film environments to cathodically controlled immersion in thin film environments on the order of microns[4]. Further experimental studies have indicated this transition in likely in the range of 500 µm to 1 mm[5–8], while recent modelling studies have suggested this critical film thickness is closer to 250 µm[9].

To date the bulk of methods employed in the creation of thin film environments for experimental testing employ similar strategies. First the sample surface to be studied is prepared through polishing and plasma cleaning (to increase the wettability of the surface), then a salt is introduced onto the sample surface, and finally control of the ultimate film thickness is achieved through careful humidity and temperature regulation. The introduction of salt onto the sample surface has been performed via many different processes, such as manual deposition[10,11], atomization[12,13], salt-printing[14], and use of an intermediary volatile solvent followed by vaporization[15–17]. Depending on the substrate wettability and salt deposition uniformity, deliquescence of water onto the surface at high humidity or stabilization of the deposited saline solution will then result in either droplets of various sizes or a uniform thin film across the surface. While this paradigm has seen widespread use in the literature, other studies have also shown the use of physical borders such as polyamide tape or plastic around a masked area of interest to artificially create water layers of known thickness[18,19].

Due to the extremely high sensitivity of atmospheric environments to humidity, temperature, surface preparation, and salt loading technique, minimal fracture-mechanics based SCC experiments have been performed in atmospheric environments as compared to full immersion conditions. Testing of an Al-Cu-Li alloy with various surface preparation techniques and droplet morphologies has been investigated by Warner, but the scope of the study was limited to fatigue testing[15]. Similarly, extensive studies investigating the atmospheric-induced SCC cracking of stainless-steel alloys has been performed, but the majority of these studies utilize a similar droplet morphology and are not linear elastic fracture mechanics (LEFM) compatible[11,13,16,17]. Therefore, there is a critical knowledge gap in the literature concerning LEFM-based SCC testing in atmospheric environments. An attempt to create such LEFM-based SCC atmospheric testing methods was established in a previous study for Al-Mg alloys, along with complementary characterization techniques germane to SCC analysis such as direct current potential drop (dcPD) and electrochemical monitoring[20]. In this study it was determined that atmospheric testing induced lower IG-SCC susceptibilities through cathodic limitation of the governing IG-SCC mechanism. In particular, for the sensitized alloy AA5083-H131 it was shown that a clear distinction in the IG-SCC susceptibility exists between the continuous misting condition, which resulted in minimal cathodic limitation, and the wicking condition, which exhibited large amounts of cathodic limitation. It is therefore possible that through the selective application of discrete thin film thicknesses between those expected for these two conditions the cathodic limitation can be manipulated and its role in determining IG-SCC susceptibility potentially demarcated. The effect of water layer thickness, potentially due to oxygen transport distance reduction and/or increased ohmic resistance, can then be further isolated. Therefore, there is the need to develop and validate a new thin film protocol that is compatible with LEFM based testing, allows for dcPD crack measurement, and allows for electrochemical monitoring. Such testing would enable data generation to inform mechanistic insights and generate quantitative growth rate behavior in atmospheric environments that can be used to improve upon current fracture mechanics-based life prediction models.

3.2.1. Chapter objective

There are four primary objectives of this chapter. First, to establish and validate a rigorous and repeatable protocol for performing high fidelity LEFM-based testing in controlled thin film environments while maintaining a constant solution chloride concentration. Second, to quantify the SCC behavior of a sensitized Al-Mg alloy at various controlled thin film thicknesses. Third, to correlate trends in observed IG-SCC behavior to measured electrochemical potential data. Lastly, to use this unique experimental data to gain mechanistic insights into the aspects of atmospheric conditions that make such conditions distinct from full immersion testing as well as comment on the implication for data generation relevant to structural management of engineering components.

3.3. Experimental methods and material

3.3.1. Materials and sample prep

In this study the Al-Mg alloy engineering alloy AA5083-H131 was investigated. The source, thickness, and composition of this alloy are reported in Table 2.1. The temper designation indicates that this alloy has been strain hardened, retaining 3/8 of the residual hardening[21]. The Ramberg-Osgood parameters and results of a grain size analysis are reported in Table 2.2. Prior LEFM based testing of this exact production lot of material demonstrated a high susceptibility to IG-SCC at a NAMLT value of 40 mg/cm^2 in 0.6 M NaCl[20]. Additional microstructure and sensitization analysis on this alloy are detailed elsewhere[22].

Single edge notch tensile (SENT) specimens of the AA5083-H131 alloy were machined with an S-L orientation (loading applied along the S direction, crack growth occurring in the L direction) and polished to 400 grit surface finish. The samples had a gauge width of 17.33 mm and thickness of 6.62 mm. A 1.52 mm deep electrically discharged machined (EDM) notch was placed at the mid-point of the gauge section which aligned with the center (T/2) location in the S-direction of the plate. Samples were then sensitized at 100°C for 336 hours to achieve the desired NAMLT value of 40 mg/cm^2 based on previously established sensitization curves for this material lot derived from ASTM G67 testing[23].

3.3.2 Mechanical testing

All fracture tests were conducted using software-controlled, servo-hydraulic frames with active crack length feedback via the direct current potential difference (dcPD) method[24]. Potential readings were taken via copper wires (0.127 mm diameter) coated in PFA (perfluoroalkoxyalkane) spot welded 0.5±0.1 mm from the center of the EDM notch with a constant 6 A or 1 A current passing through the sample during precracking and constant displacement testing, respectively. These potential readings were then taken every 30 seconds in a process reported by McMahon et al.[22,25] and converted to an instantaneous crack length using the Johnson's equation, resulting in crack growth resolution of roughly 0.5 µm[22].

Samples were loaded by means of freely rotating clevis grips, in compliance with stress intensity (K) boundary conditions[26]. They were fatigue precracked to a cumulative notch plus crack length of 2 mm at a constant K_{max} of 6 MPa√m at a stress ratio ($R = K_{min}/K_{max}$) of 0.1 and a frequency of 8 Hz. The precrack length was then extended to 2.75 mm via a decreasing K protocol from a K_{max} of 6 MPa√m to a K_{max} of 3.5 MPa√m at a stress ratio of 0.1 and a frequency of 3 Hz. At this point a 2 kN load was applied to the precracked specimens (corresponding to a K_{max} of roughly 2 MPa√m) and the testing environment was introduced; these conditions were held for 1 hr to stabilize the initial crack tip and bulk surface chemistry. Following this 1 hr hold samples were tested via slow-rising displacement at a rate corresponding to an initial dK/dt of roughly 0.25 MPa√m/hr. Tests were run until failure or the samples exhibited bulk scale plasticity.

Following test completion, linear post-processing crack length corrections were applied based on fracture surface analysis of the initial and final crack lengths. Crack growth rates were calculated from the tangent of a second order polynomial fit to 7 crack length vs time data points (akin to the protocol established for fatigue crack growth rates in ASTM E647[27]). Elastic-plastic stress intensity (K_J) analysis was also conducted using the 0.2% offset yield strength and Ramberg-Osgood constants for the alloys, derived via compressive testing and reported in Table 2.2, in compliance with previous literature[28–30]. A functional resolution limit due to localized (crack tip) plasticity introducing 'false' dcPD-measured crack extension was previously established for this production lot of AA5083-H131 lot and has a functional form of:[30,31]

$$\frac{da}{dt}_{False} = 5 \times 10^{-7} \cdot \exp(0.0577K) \qquad \text{(Eq. 3.1)}$$

Recent fracture mechanics experiments conducted in an inert environment (dry N_2 gas with RH < 5%) on a Ni-based superalloy using a fixed dK/dt testing protocol demonstrate that the dcPD-measured resolution limit scales linearly with dK/dt[32]. A correction protocol was then developed to subtract this 'false' da/dt contribution from measured da/dt, thereby enabling the 'true' da/dt to be determined for an experiment conducted under fixed dK/dt conditions[32]. Given that the current study utilizes testing at a fixed displacement rate, it is expected that dK/dt will begin to increase from the initial value of 0.25 MPa√m/hr once crack growth occurs. As such, it is incorrect to simply subtract Eq. 3.1 from measured da/dt vs. K relationships as was done in prior work[22,25,32,33] since Eq. 3.1 is only rigorously valid for dK/dt = 0.3 MPa√m/hr and therefore must be modified to incorporate an explicit dK/dt dependence. Given that the mechanistic basis for the scaling in the resolution limit is based solely on fracture mechanics principles[32,34] and is therefore nominally material-agnostic, a dK/dt dependence can be introduced into Eq. 3.1 via dividing the prefactor (5×10-7) in Eq. 3.1 by the dK/dt for the experiment to which Eq. 3.1 was fit (0.3 MPa√m/hr)[30], yielding:

$$\frac{da}{dt}_{False} = 1.667 \times 10^{-6} \left(\frac{dK}{dt}\right) \cdot \exp(0.0577K) \qquad \text{(Eq. 3.2)}$$

In the current study, dK/dt was determined by numerically differentiating a smoothing spline fitted to the experimental K vs. time data using the Matlab curve fitting toolbox. A smoothing parameter (p) of 0.9 was utilized for fitting each individual experiment. The smoothing spline was selected for fitting the K vs. time profile due to an improved fit (quantified *via* R^2) over the entire time range relative to a power law or exponential function. Once the dK/dt vs. K relationship is known Eq. 3.2 can be utilized to calculate a test-specific resolution limit that accounts for the expected increase in dK/dt as cracking progresses. This 'false' da/dt can then be subtracted from the experimentally-measured da/dt to correct for effects of localized plasticity on the dcPD system[32].

3.3.3. Thin film generation

Multiple thin film generation protocols were explored and eventually rejected due to procedural and/or accuracy concerns. The traditional method of thin film creation *via* salt solution spraying was first employed, but orientation of the sample surface vertically and heating of the sample due to dcPD current (even when lowered to values as low as 1 A) resulted in low film stabilities and frequent drying of the sample. Additionally, values for calculated thin film thicknesses, derived from calculations of the salt loading density and sample surface area, were highly variable and inconsistent. Similar issues were experienced when attempting deliquescence of a thin film in high humidity environments. Ultimately, a novel technique derived from the use of physical borders and an anodized aluminum oxide (AAO) membrane was established that was able to address these concerns.

3.3.4. Thin film environmental setup

Prior to testing, samples were cleaned by sonication in acetone, methanol, and DI water, respectively for 15 min each and subsequently dried with pressurized air. Vinyl electrical tape, of a known targeted thickness, was then used to surround the edges of the SEN(T) gauge section to create a border around the crack path and sides of the sample, resulting in an exposed area of roughly 15 mm x 12 mm on each side, leaving four solution/gas ports along the top. Whatman® Anodisc AAO membranes with 20 nm pore diameter were sourced from Sigma Aldrich for this study and pretreated for one hour in a 5% trimethoxy(octyl)silane in acetone solution to further induce hydrophobicity. An AAO was then placed over the electrical tape border on both sides of the sample as seen in Figure 3.1. Additionally, an AAO membrane was placed over the front of the sample over the notch opening directly, offset only by the spot welded 127 µm diameter copper wires, to prevent leaking. A rubber butyl stop-off lacquer was then used to seal the edges of the AAO membrane below the crack path plane while silicone vacuum grease was used above the cracking plane to allow for sliding of the membrane during mechanical testing and extension of the sample. A thin cellulose strip was placed into one of the solution input ports to allow for filling of the AAO "jacket" with solution. The sample was then enclosed in an acrylic cell with two enclosed saturated potassium sulfate solution reservoirs (~500 mL total) surrounding the sample to maintain a high relative humidity (~98%) throughout the duration of testing to prevent drying of the sample and variation in the solution concentration.

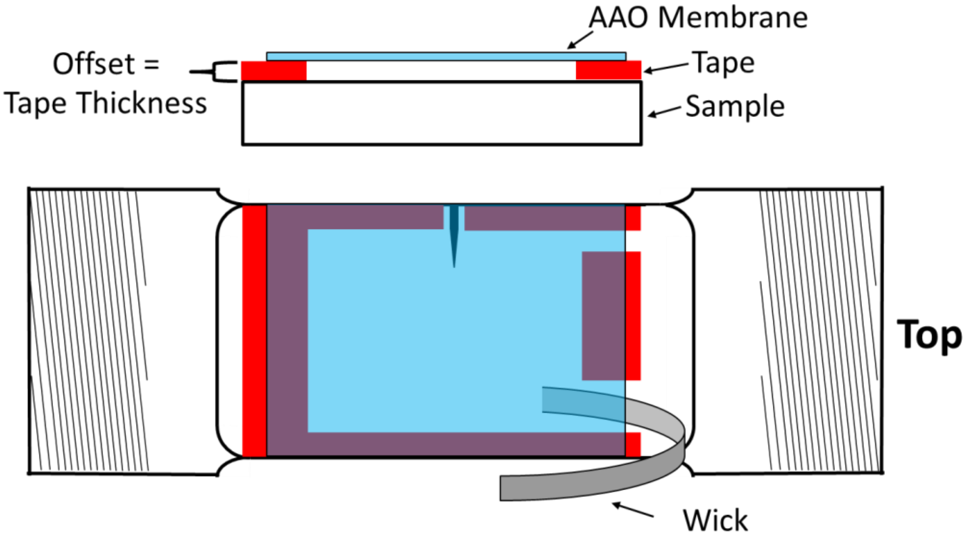

Figure 3.1. Schematic of the thin film setup. An AAO membrane (blue) is placed over a tape border (red) of a known thickness. Two gaps in the tape border near the top are left for air escape during filling and a cellulose wick to introduce solution.

3.3.5 Electrochemical monitoring

During LEFM testing, the OCP was monitored via a 4 mm diameter sintered silver/silver-chloride probe (SSC). Details of the governing electrochemical concepts, functional details/limitations of the probe application, and verification of the probe accuracy for thin film electrochemical measurements was demonstrated by Khullar et al.[19] and successfully demonstrated to work with SCC testing in a previous study[20]. Notably, the probes were found to not impact the electrolyte composition, function well with currents up to 1 mA, and calculation of the ideal solution theoretical potential of these probes at 25°C in a 0.6 M NaCl solution (via the Nernst equation) reveals only a 5 mV difference (E_{SSC} = +0.236 V_{SHE}) from that of an SCE reference probe (E_{SCE} = +0.241 V_{SHE}). During testing the probe was placed outside one of the AAO membrane solution input ports and ionically connected via a saturated cellulose strip. The probe was attached to the outside of the sample via 100 µm thick double-sided adhesive. It is worth noting that in the probe configurations detailed above, distance from the crack tip to the SSC probe through thin/narrow ionic solution paths may lead to an increased electrical resistance.

This can cause a change in the perceived potential due to ohmic drop, thus affecting the accuracy and validity of the SSC probe as has been seen in previous related testing[20], but should be relatively minor in the scope of this study due to the low currents involved.

3.4. Results

3.4.1. AAO film verifications

To validate the use of AAO membranes in the creation of thin water films, it must be shown that (1) water layers produced using these films accurately represent the nominal water layer thickness, (2) the membrane is electrically non-conductive and water impermeable, and (3) oxygen is allowed to diffuse through the membrane without sufficient resistance to alter electrochemical reactions. The accurate water layer representation of the AAO membrane was tested using a 10 mm x 50 mm poly(methyl methacrylate) cell with two 0.5 mm diameter nickel (99.98%) wires embedded perpendicularly into the surface 5 mm apart, as seen in Figure 3.2a. Vinyl tape borders of known thicknesses were then placed along the sides of the cell and an AAO membrane placed on top of these borders. Saturated NaCl solution (5.45 M) was then inserted between the AAO membrane and the cell surface between the two nickel electrodes. Electrochemical impedance spectroscopy (EIS) at open circuit potential was then performed between 7 Mhz to 1 khz with six measurement points per decade of frequency. Sine waves with an amplitude of 10 mV were applied at about the open circuit potential and each point was an average of 10 measures with no reference electrode, resulting in a curve similar to Figure 3.2b. A derivative was taken of the resistance curve and the resistance of the frequency value associated with the lowest change in resistance (which is taken to be the resistance of the water layer minus the interfacial resistances between the nickel and solution) was used to calculate the water layer thickness according to Equation 3.3:

$$WL = \frac{d}{R_{WL} \times \kappa \times w} \qquad \text{(Eq. 3.3)}$$

Where d is the distance between electrodes, R_{WL} is the resistance and the chosen frequency, κ is the solution conductivity, and w is the width of the channel between the tape borders. Calculated thin film thickness are reported in Table 3.1. Further investigation into the accuracy of these AAO-created thin films using this EIS device are discussed in a complementary paper by Katona et. al, and show good agreement with COMSOL modelling[35].

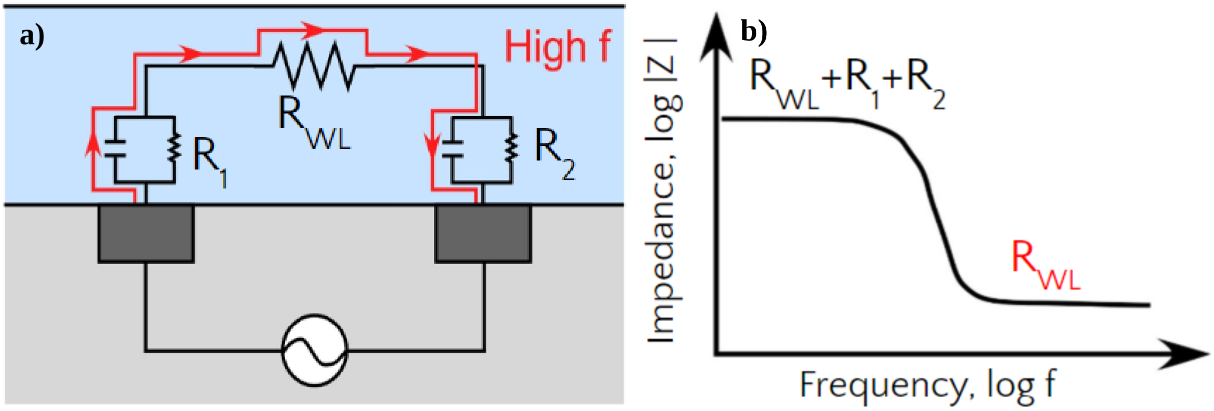

Figure 3.2. EIS device schematic for thin film thickness verification (a) a simplified diagram of a Bode plot obtained from the EIS device indicating the measured resistance used to calculate thin film thickness.

Table 3.1. Comparison between optically measured WL thicknesses versus WL thicknesses calculated via EIS.

Tape Thickness (µm)	WL Calculated (µm)	Difference (µm)
54.1	52.9	1.2
58.8	62.1	3.3
77.2	80.8	3.6
82.0	77.3	4.7
92.0	79.8	12.2
137.0	138.9	1.9

Verification of the AAO membrane protocol physical accuracy can be seen by the good correspondence between the actual thickness of the bordering tape, as measured by optical microscope, and the calculated water layer thickness via EIS device in Table 3.1. All but one measurement resulted in correspondence ±5 µm, ultimately indicating that the nominal water film thickness is being accurately represented by the tape thickness and the AAO membrane is serving as an effective, non-permeable border for the thin film solution. Verification of the AAO membrane electrical resistance and liquid water impermeability can also be quickly verified.

To test the gas permittivity of the membrane a 38 mm diameter hole was drilled into 4.5 L container with an Altair® O_2 atmospheric gas detector (0.1% resolution) inside. The container was then completely filled with pure nitrogen gas and the atmospheric oxygen content measured in separate tests with the hole completely covered, covered with the AAO membrane, and completely open. Data was taken every 10 seconds for 5 minutes or until 5% oxygen inside the container was reached. These results are shown in Figure 3.3, and show that oxygen diffusion through atmospheric air is slowed to roughly 20% when an AAO membrane is used. Despite this reduction, oxygen diffusion rates in air are recorded to be roughly 4 orders of magnitude greater than that of oxygen in water and thus should have a negligible impact on the atmospheric oxygen available at the rate-limiting water-air interface[36,37]. The effects of the reduced surface area caused by the AAO membrane on the diffusion of this oxygen into the thin film itself at this water-air interface can then be analyzed further using COMSOL modelling.

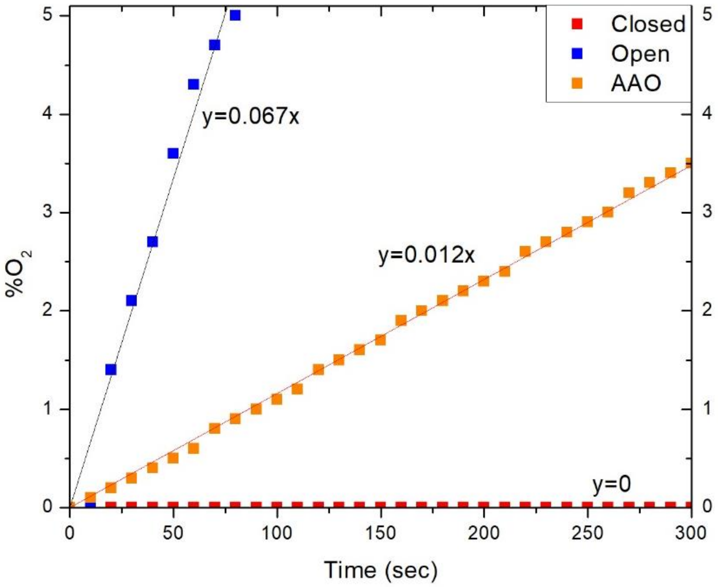

Figure 3.3. Results indicating the gas permittivity of the AAO membrane. Oxygen diffusion was reduced by approximately 82% when an AAO membrane was placed over the opening as compared to when it was uncovered.

Finite element analysis was performed using COMSOL (ver. 5.5) by Carolina Vicente Moraes of the Robert Kelly research group at UVA to model the impact of the AAO membrane on the oxygen diffusion in the electrolyte. Figure 3.4 shows a schematic of the geometry utilized in the model. The total length of the geometry was 100 µm and two water layer thickness were simulated: 25 and 800 µm. The top boundary, which is indicated by a dashed line, represents the membrane. The empty spaces between the segments represent the pores where air is in contact with the solution. The segments represent the alumina walls that separate the pores. The diameter of the pores was defined to be 20 nm with a porosity of roughly 50%, which was verified *via* SEM analysis. The thickness of the walls was varied according to the membrane porosity. For example, for a porosity of 50%, both the wall thickness and pore diameter were set to 20 nm;

note that Figure 3.4 is not to scale. The bottom boundary describes the surface of the metal. The concentration of oxygen at this boundary was set to 0, consistent with fast oxygen reduction occurring at the surface of the metal which represents a worst-case scenario in terms of the membrane affecting the electrochemistry. At the top boundary, two different boundary conditions were used to simulate the pores and the walls. At the walls, the normal flux of oxygen was set to 0. At the pores, the concentration of oxygen was set equal to the saturation concentration of oxygen in an electrolyte solution of 1 M NaOH (9.2×10^{-4} M)[38], assuming that, at the air/liquid interface, the dissolved oxygen is in equilibrium with its partial pressure of 0.21 atm. At the right and left boundaries, the normal flux of oxygen was set to 0. The initial concentration of oxygen within the electrolyte was set to 0, simulating a deaerated solution. The oxygen diffusion coefficient of 1.65×10^{-5} cm^2/s was extracted from the literature for a 1 M NaOH electrolyte solution[38].

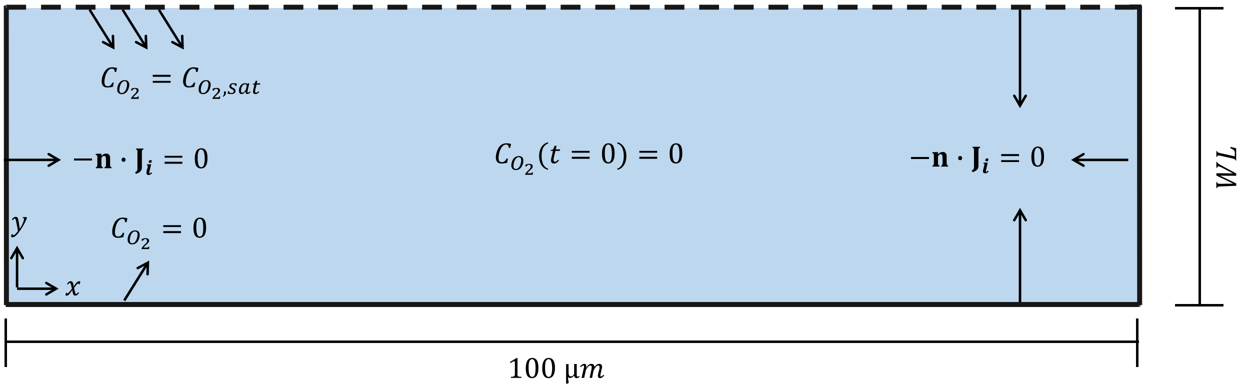

Figure 3.4. Schematic drawing of the geometry and boundary conditions utilized to model O2 transport. Note that the drawing is not in scale.

Figure 3.5(a) shows the flux transient of dissolved oxygen at the midpoint on the surface of the substrate (at x = 50 μm; Figure 3.4) under an electrolyte film of 20 μm with and without a 50% porosity membrane. In particular, Figure 3.5(a) demonstrates that the fluxes with or without the AAO membrane significantly overlap, indicating that the presence of the membrane does not affect the flux of oxygen reaching the metallic substrate. Additionally, the diffusion of oxygen is fast for these thin water layers, as steady-state is reached in approximately 0.2 s. Figure 3.5(b) displays the oxygen concentration gradient, in a color scale, and the oxygen flux, represented by streamlines, at steady-state (t = 1 s). The dissolved oxygen concentration varies from 9.2×10^{-4} M, at the air/liquid interface, to 0 M, at the surface of the metal, as defined by the boundary conditions. Figure 3.5(c) shows a close-up view of a single flux streamline with the AAO membrane (solid line) and without the membrane (dashed line). The oxygen flux obtained with the membrane only deviates from the flux obtained without the membrane within 20 μm of the air/electrolyte interface.

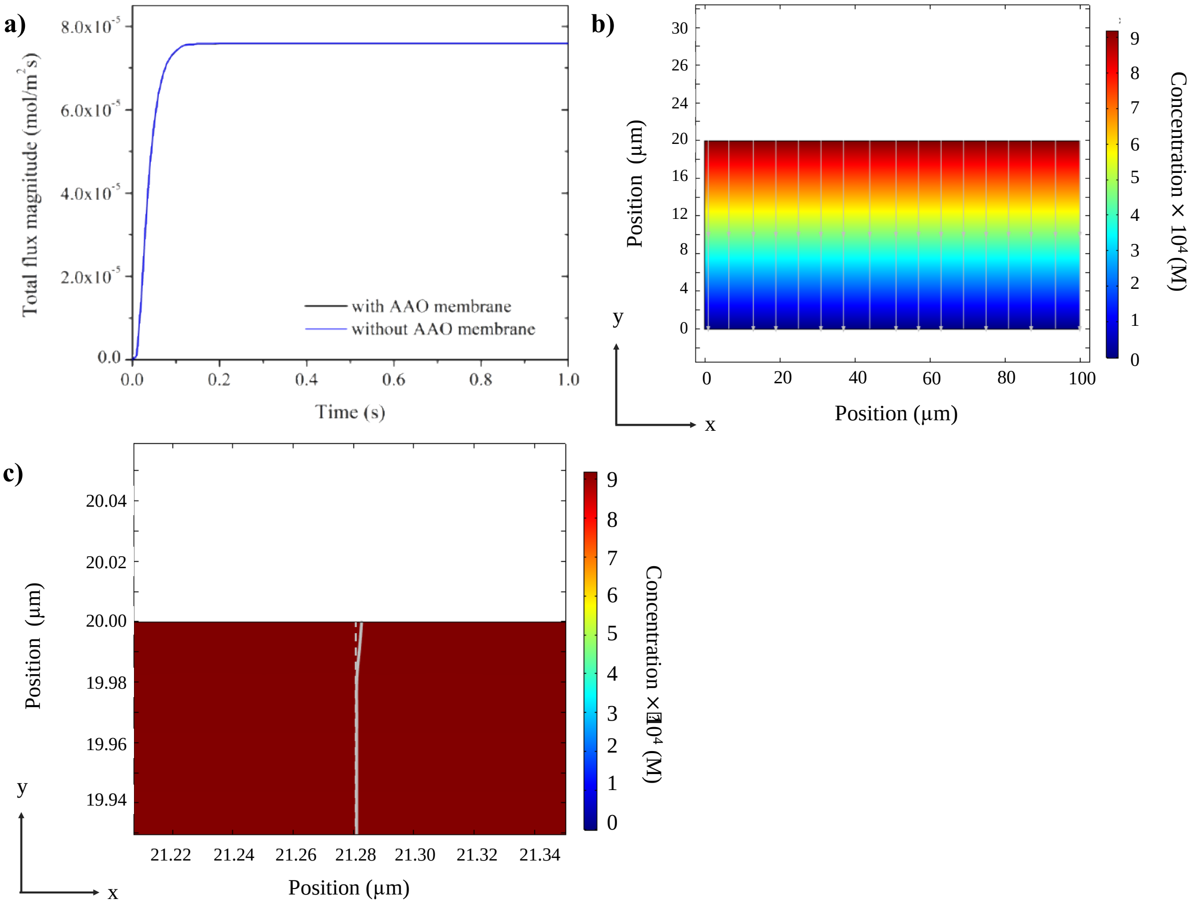

Figure 3.5. a) Oxygen flux transient at the midpoint of the surface of the metal (x=50 μm) at a 20 μm WL with and without the AAO membrane (50% porosity); b) Oxygen concentration gradient and flux streamlines on at steady-state (t = 1 s); c) Close-up view of one the flux streamlines. The dashed line represents the oxygen flux streamline calculated without the AAO membrane over the electrolyte film.

Figure 3.6 shows the ratio of the dissolved oxygen flux at the surface of the metal with and without the membrane over a 20 μm electrolyte film for different porosities (50, 25, 12.5 and 1%). The ratio of the fluxes is approximately 1 for porosities ranging from 50 to 12.5%, confirming that the membrane does not affect the oxygen diffusion. With a porosity of 1%, however, the oxygen flux reaching the surface is restricted by the membrane, as evidenced by the smaller ratio of 0.89 between the fluxes in Figure 3.6. Figure 3.7a shows the flux transient at the surface of the metal with and without a 50% porosity membrane over an 800 µm thin film. For an 800 µm WL, the flux reaches steady-state at approximately 200 s. Again, the membrane does not affect the steady state flux at the surface of the metal. Figure 3.7b shows the ratio between the fluxes at the surface of the metal with and without a membrane with varying porosities. In an 800 µm thick electrolyte film, the oxygen flux is not considerably affected by the membrane at steady state, even for 1% porosity membrane. These modelling results therefore indicate that for the 50% porosity AAO membrane used in this study oxygen diffusion through the membrane is not affected for thin films between 20 µm to 800 µm.

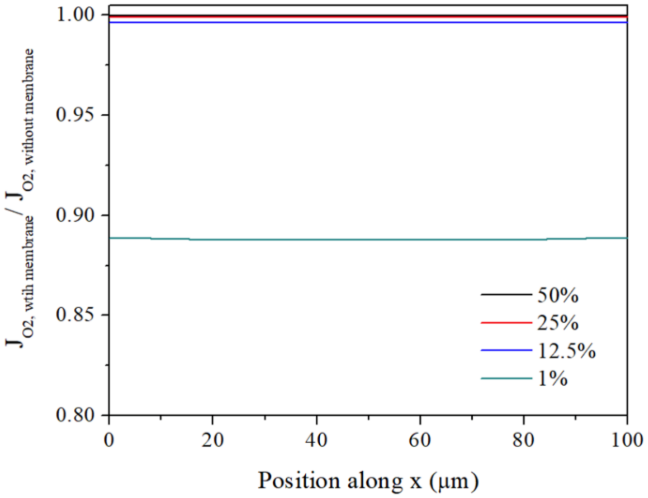

Figure 3.6. Ratio of oxygen flux at the surface of the metal with and without a membrane of varying porosities for a 20 µm WL.

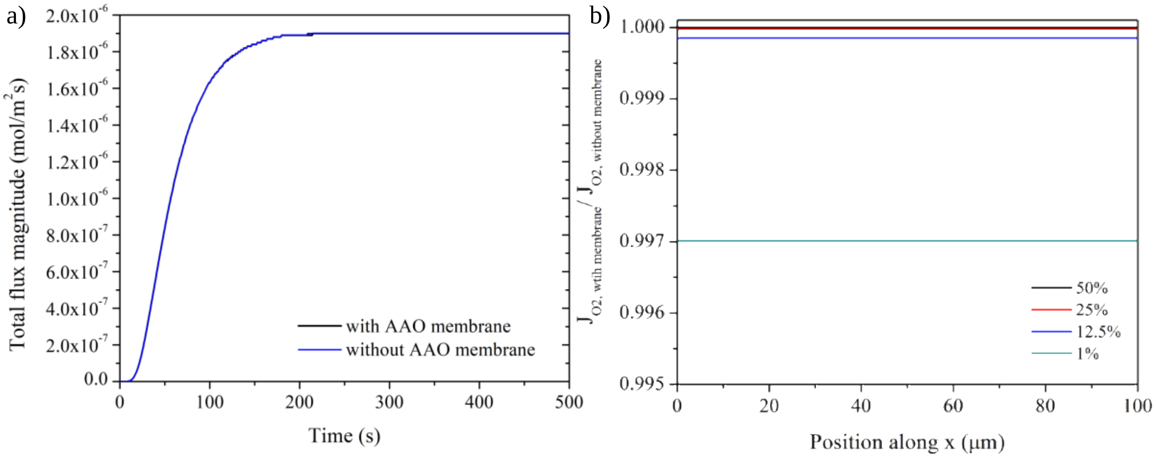

Figure 3.7. a) Ratio of oxygen flux at the surface of the metal with and without a membrane of varying porosities for an 800 µm WL; b) Ratio of oxygen flux at the surface of the metal with and without a membrane of varying porosities for an 800 µm WL.

3.4.2. Influence of thin film thickness on IG-SCC

Use of the dcPD method and slow rising displacement loading protocol described above allows for detailed analysis relating the crack growth rate, da/dt, versus the stress intensity, K_J. From these data the various stages of SCC crack growth can be determined and the IG-SCC dependent parameters derived. Traditionally the two parameters of interest are the K_{TH} and the Stage II crack growth rate (da/dt_{II}). The K_{TH} is demarcated as the stress intensity at the beginning of IG-SCC dominated fracture as opposed to stress-assisted intergranular corrosion (IGC). This is traditionally defined as the stress intensity at which crack growth exceeds the resolution limit. Due to the high susceptibility of AA5083-H131 at a NAMLT level of 40 mg/cm^2, however, stress-assisted IGC occurs at rates above this resolution limit and the K_{TH} is instead defined as the onset of Stage I cracking and a rapid increase in crack growth rate[31]. The da/dt_{II} is defined as the crack growth rate which it is largely independent of increasing stress intensity; this has been postulated to be due to an H-diffusion limitation from the crack tip surface into the crack tip process zone[31,39]. This limitation causes a plateau in the da/dt vs K_J graph leading up to the K_{IC}, at which point sub-critical HEAC based cracking is augmented by a ductile failure mechanism (possibly some stable ductile tearing then final rupture). It is worth noting that scatter has been observed in the da/dt vs. K_J relationship for samples from the same lot run under the same conditions, thus current data should be analyzed in the context of this inherent variability[31]. While experimental complexity and material resources have limited extensive replicates, duplicates of tests have been performed to address these concerns.

Crack growth vs stress intensity data for AA5083-H131 sensitized to NAMLT 40 mg/cm^2 at various thin film thicknesses are reported in Figures 22a-f. Included are data from prior work for full immersion (termed FOCP 2 cm; solid line), and wicking (dashed line); these data bound the levels of cathodic limitation possible for the thin film testing. Testing at all thicknesses resulted in K_{TH} values between 4-7 MPa√m and were largely bounded by the FOCP 2 cm and wicking conditions. The 54 and 82 µm thick thin film conditions exhibited K_{TH} of around 6 to 7 MPa√m and a da/dt_{II} of ~6×10^{-4} mm/s, which are akin to the wicking conditions, however a dual trend is observed for thicknesses 92 µm and larger. Specifically, for the 92, 137, 184, and 229 µm thicknesses one duplicate is observed to behave similar to the wicking (and the 54 and 82 µm) results while the other duplicate shows a significantly decreased K_{TH} of ~4 MPa√m and a da/dt_{II} of ~1x10^{-3}.

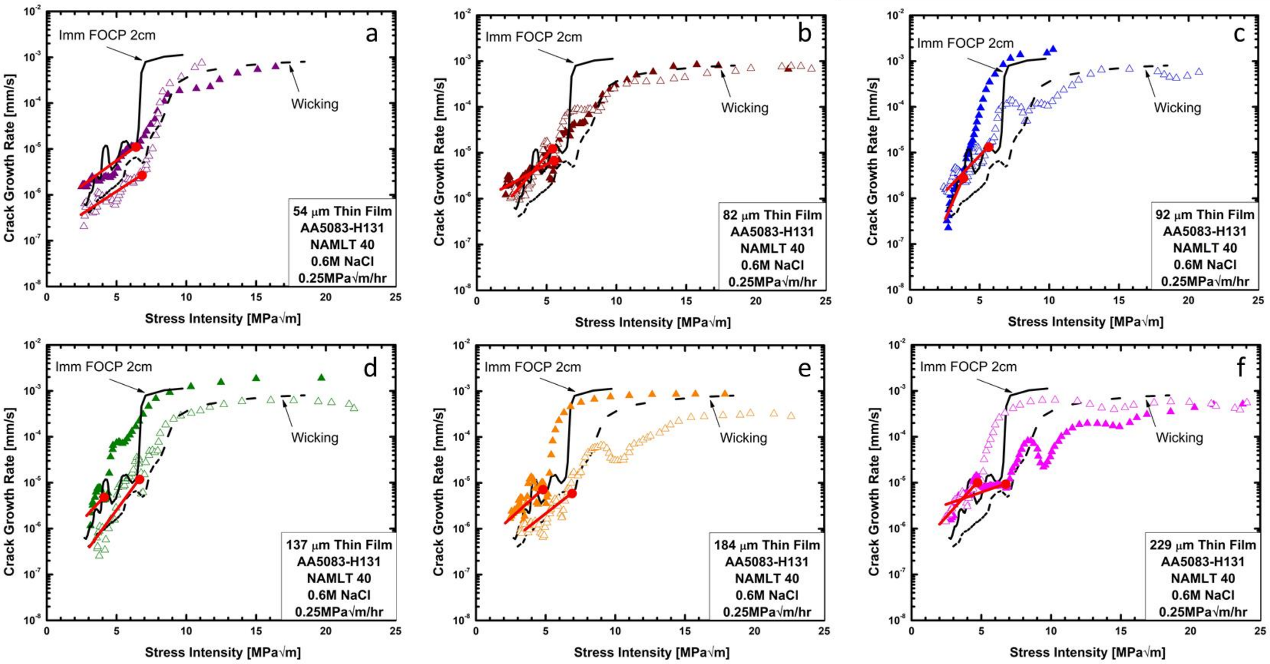

Figure 3.8. Crack growth rate vs. stress intensity for AA5083-H131 at a NAMLT values of 40 mg/cm^2 for thin film thicknesses of a) 54 µm, b) 82 µm, c) 92 µm, d) 137 µm, e) 184 µm, and f) 229 µm. The IGC regime and K_{TH} for each test are represented by a red line and circle, respectively.

In summary, two findings are worth noting. First, for film thickness ≤ 82µm, IG-SCC crack growth kinetics were akin to the wicking condition which suggests a similar level of cathodic limitation. Second, for film thickness ≥92 µm, a dual trend was observed in which one condition behaved similar to a cathodically limited condition (wicking) while the other behaved more akin to a non-cathodically limited condition (FOCP 2 cm) with a significantly lower K_{TH}.

3.4.3. Electrochemical potential observations

Applied potential strongly impacts the IG-SCC susceptibility of 5xxx series aluminum alloys[30,40]. This observation was extended to atmospheric conditions in a prior work where changes in the bulk surface potential directly correlated to IG-SCC crack progression[20]. As such the potential was monitored during testing in an attempt to correlate trends in the OCP to the crack growth kinetics. Examples of collected OCP plots are shown in Figure 3.9 for thin film thicknesses of 54 µm (Figure 3.9a), 92 µm (Figure 3.9b), and 229 µm (Figure 3.9c). Common trends correlating to the different crack growth regimes are observed, as seen and reported in a previous paper[20]. These trends are: (1) a slight or negligible drift in the OCP prior to the K_{TH}; (2) a more significant and constant decline in OCP during Stage I and Stage II crack growth; and (3) reaching of a minimum OCP close to sample failure with sharp negative spikes in the OCP during sudden ductile failure events. These regimes are delineated in Figures 3.9a-c by marking the K_{TH} and K_F (stress intensity upon final failure) on the plots with vertical lines. Values of the OCP at the start of SCC testing (E_I), at the K_{TH} (E_{TH}), and at K_F (E_F) are reported in Table 3.1 for all thin film thicknesses in which OCP was successfully collected. These values are compared to a full immersion test run at -0.8 V_{SCE} in Figure 3.10.

Table 3.2. Values of the OCP (V_{SSC}) at the start of SCC Testing (E_I), at the K_{TH} (E_{TH}), and at K_F (E_F) for all thin film thicknesses.

Recorded Potential (V_{SSC})	Thin Film Thickness					
	54 µm	82 µm	92 µm	137 µm	184 µm	229 µm
E_I	-0.782	X	-0.813	-0.823	-0.796	-0.809
E_{TH}	-0.79	X	-0.811	-0.817	-0.794	-0.793
E_F	-0.854	X	-0.883	-0.877	-0.882	-0.877

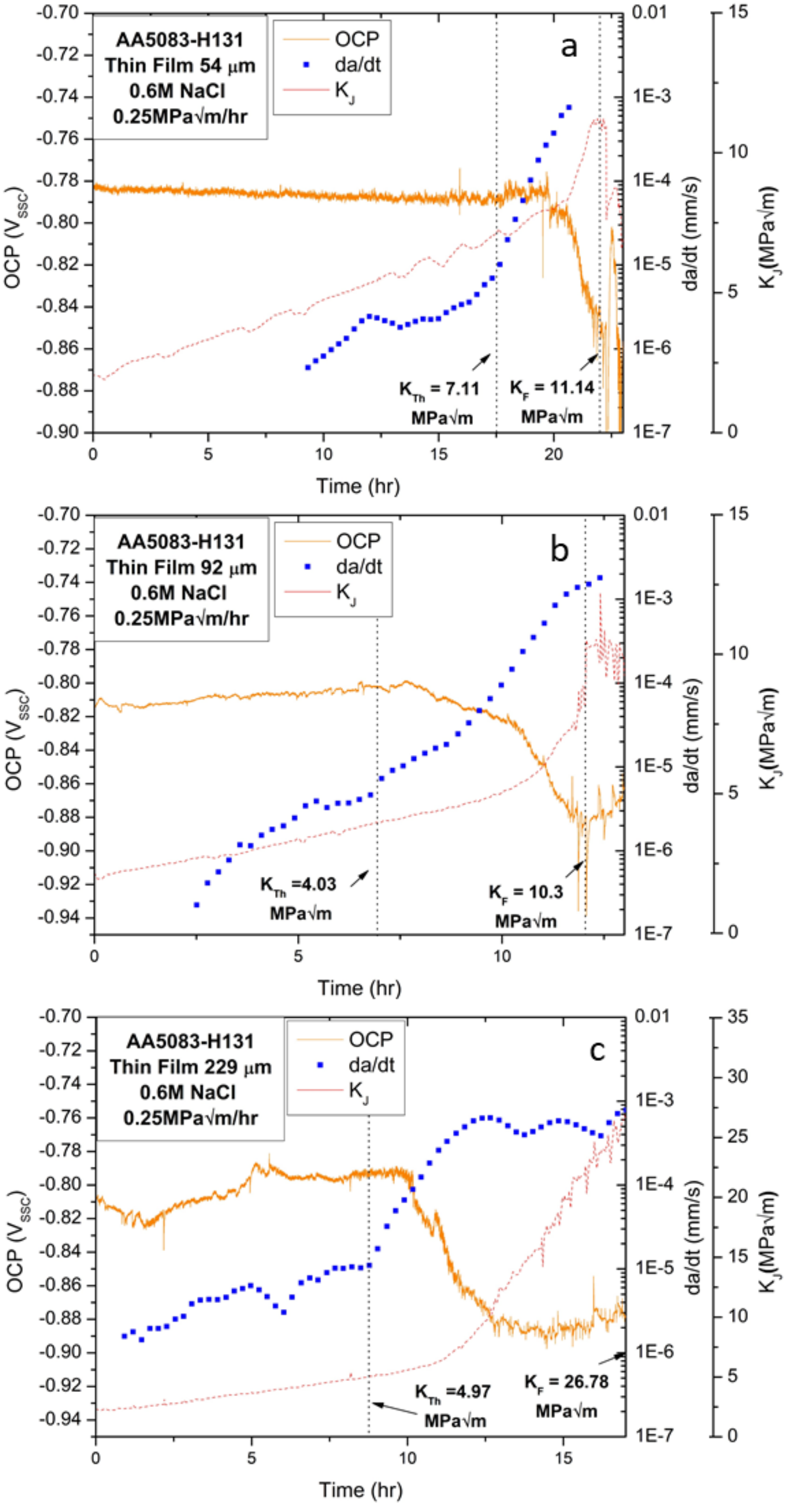

Figure 3.9. OCP (V_{SSC}), da/dt (mm/s), and K_J (MPa√m) vs time (hr) data for (a) AA5083-H131 NAMLT 40 mg/cm2 54 µm, (b) AA5083-H131 NAMLT 40 mg/cm2 92 µm, and (c) AA5083-H131 NAMLT 40 mg/cm2 229 µm.

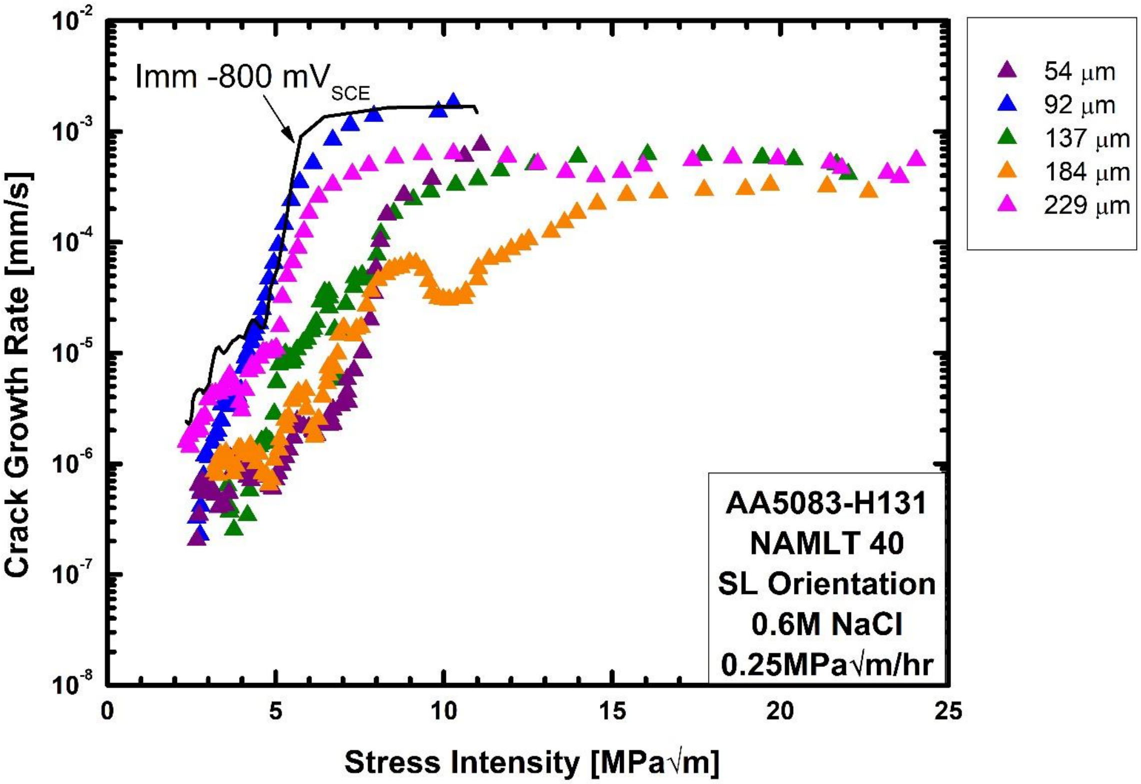

Figure 3.10. Crack growth rate vs. stress intensity for AA5083-H131 at a NAMLT values of 40 mg/cm^2 for different thin film thicknesses compared to AA5083-H131 at a NAMLT values of 40 mg/cm^2 in the full immersion condition set to -800 mV$_{SCE}$.

3.5. Discussion

The discussion will address three aspects of the results: (1) the verification and applicability of the thin film environment protocol detailed in this paper, and (2)-(3) addressing the observed mechanical and electrochemical phenomenon in the context of previously established frameworks and postulated IG-SCC mechanisms, respectively. Figure 3.8 demonstrates that the thickness of the solute thin film has a discernable effect on the IG-SCC susceptibility of the sample, with larger thickness tending to result in higher observed crack growth rates. These results correlate well with a cathodic limitation framework, in which anodic demand fueling the relevant IG-SCC mechanism is being limited by ohmic drop of the supporting cathodic area surrounding the crack tip through the thin film solution. Larger water layers have been shown to exhibit smaller ohmic resistances, thus are expected to show lower amounts of cathodic limitation and higher IG-SCC susceptibilities. This framework is further supported by observed trends in the OCP values collected during testing with an SSC probe, in which the bulk potential is seen to correlate well with anticipated anodic demand. Critically, these results were obtained with a nominally constant chloride concentration across all testing and any effects due to a changing electrolyte composition should be minimal in this current study.

3.5.1. Verification of the thin film protocol

Use of an AAO membrane to artificially create a thin layer of solution around a sample is a novel technique that allows for the creation of a thin film conditions under environments and testing conditions that are otherwise resistant to traditional thermodynamically-controlled techniques. This technique allows for greater variability in sample orientation, temperature, and humidity while maintain a constant and evenly spread thin film of solution across the entire solution surface. While this technique allows for greater control and maintenance of thin films, it is of critical importance that the AAO film does not interfere with the required electrochemical reactions necessary for IG-SCC for the technique to be applicable to atmospheric environments, as opposed to an occluded environment.

It has been well documented that the availability of oxygen at the sample surface can have a strong impact on corrosion rates in IGC studies due to the oxygen reduction reaction (ORR) that serves as the cathodic reaction[3]. Therefore, it is critical that the experimental configuration does not impede diffusion of oxygen into the thin film since this could inhibit the mass transport kinetics of the cathodic reaction; two potential effects should be explored. First, the diffusion rate of gaseous oxygen through the membrane and the oxygen uptake of gaseous oxygen into liquid water at the membrane interface must not limit the available oxygen at the sample surface beyond that inherent to the thin film condition. Figure 3.3 shows that oxygen diffusion rates through the membrane is roughly one fifth of that through air, and could potentially limit the oxygen diffusion into solution. However, the oxygen diffusion rates through water are orders of magnitude lower than that of oxygen through air[36,37], as such the observed reduction of oxygen diffusion through the AAO (relative to air) would not be the limiting step in the transport of oxygen to the sample surface and ample oxygen should be able to reach the liquid water interface. Second, oxygen uptake at the water interface could be affected due to a reduction in exposed liquid water surface area created by the AAO membrane. Modelling of this interface for a variety of AAO membrane porosities, and therefore exposed liquid area to atmosphere, shows that oxygen diffusion through AAO created thin films is negligible over thin film thicknesses from 20 µm to 800 µm. This clearly illustrates that for the 50% porosity AAO membrane used in this study, oxygen diffusion through the AAO membrane and liquid water interface is unchanged for all thin film thickness employed and could be extended to broader ranges thin film thicknesses if desired.

Provided that there are no AAO induced changes in the oxygen availability, the other primary effect of a thin-film geometry on the resulting corrosion rate is expected to be a modification of ohmic drop through the solution between the cathode and anode[3,41]. Smaller solution geometries have larger ohmic drops associated with them, thus limiting the available cathodic area and resulting cathodic current. Therefore, it is of great importance that thin films created with AAO membranes do not alter this ohmic resistance when compared to a model thin film created without an AAO membrane cover. Alumina, being an electrical resistor, has orders of magnitude lower conductance (~10^{-8} µS/cm) than chloride containing solutes (~10^{4} µS/cm) and should thus not contribute to any currents passing through the film. Further confirmation of its liquid water permeability and accurate representation of the nominal thin film thicknesses via EIS, illustrated by Table 3.1, indicate that ohmic resistance through the films will be governed solely by the indicated thickness of the encapsulated thin film.

3.5.2. Effect of film thickness on IG-SCC susceptibility

Observed trends in IG-SCC susceptibility 5xxx-series alloys in atmospheric environments can be understood in the context of a couple anodic dissolution and HEAC-based mechanism for cracking. As anodic dissolution of the intergranular β phase (and α Al matrix) at the crack tip occurs, hydrolysis of the resulting cations will cause a strong drop in the crack tip pH and ingress of [Cl-] to maintain charge neutrality. These crack tip conditions are conducive to H production and adsorption at the crack tip. This adsorbed hydrogen can then diffuse ahead of the crack tip in the fracture process zone resulting in embrittlement and more rapid crack growth rates than seen for anodic dissolution alone[31]. The initial anodic dissolution process requires and equal cathodic current supply; in the absence of an external source (e.g. a potentiostat or galvanic couple) the crack wake or bulk sample surface must provide this cathodic current[1,2]. The available cathodic area, and thus maximum cathodic current, is determined by the geometry and properties of the electrolyte due to ohmic resistance along ionic paths. In cases where the environment causes large amounts of ohmic drop, such as with thin solution layers and low conductivity electrolytes, cathodic limitation can occur and limit the maximum cathodic current and thereby the extent of the anodic reactions that govern the proposed IG-SCC mechanisms. The effects of geometry-introduced cathodic limitation due to reduced cathodic area availability in atmospheric environments has been observed and discussed in a previous paper for the current material lot[20]. However, as the film thickness decreases (to on the order of microns) it is also necessary to account for a potential impact of enhanced access for oxygen replenishment due to small diffusion distances from the bulk environment to the electrolyte-metal interface. Many studies have shown that as water layer thickness reduces to thicknesses below that of the natural convection layer of oxygen the cathodic rates can instead increase due to increased oxygen availability on the sample surface[3,5–7]. The exact thickness of this convection layer is debated, but studies have suggested values as low as 250 μm for this critical thickness[9]. Figure 3.8a-b shows that the lowest thin film thicknesses tested (54 and 82 μm) behaved most similar to the wicking conditions, which was the most cathodically limited solution geometry tested in prior work[33]. This suggests a dominant role of ohmic resistance, despite the increased availability of oxygen diffusion at these lower thicknesses.

Interestingly, for thicknesses ≥92 μm (Figure 3.8c-f) a dual trend is observed in the testing between duplicate tests. While the origin of this dual behavior is unknown it is clear that in some instances the IG-SCC susceptibility increases. This indicates that for this specific sample geometry, alloy lot, and solution composition the “critical thickness” needed to achieve cathodic limitation may be between 82 and 92 μm. Origins of the dual behavior seen for thin film thicknesses ≥92 μm could potentially be due to: (1) the variability in the testing protocol, and/or (2) inherent variability in the IG-SCC behavior for atmospheric conditions. Considering the first, the complexity of the experimental setup could cause inaccurate thin film thicknesses, loss of a discrete thin film as the sample extends, and/or modification of the thin film concentration.

While the validations of the experimental procedures (detailed above) suggested a well-controlled protocol, it is still prudent to detail how such errors could be induced. Inaccuracies in thin film thickness could result from two sources, either errors in the tape border thicknesses or flexure of the AAO film over the exposed surface. As EIS measurements confirm tape thicknesses were largely correct ±5 µm, and alumina is a rigid ceramic, any errors from these sources should be negligible. Intermittent drying out or loss of the thin film condition during the test would result in local conditions akin to the wicking environment, which would be consistent with the dual behavior observed in Figure 3.8c-f. Moreover, a change in thin film thickness during testing due to either evaporation or water vapor deposition could result in a change in chloride concentration. However, this scenario seems unlikely since steps were taken to mitigate the loss of a discrete thin film, such as enclosing the sample in a high humidity chamber. Additionally, visual observation and the consistency of relevant OCP measurements via the SSC probe during the testing duration further confirm a thin film was maintained.

Alternatively, this dual behavior could be an artifact of the inherent variability of SCC testing. A study on this same material lot by Crane showed that replicate testing of the same condition and protocol could yield an average variability of 2 MPa√m in the K_{TH} and ~$1x10^3$ mm/s in the da/dt_{II}[31]. It was postulated that this could be due to crack tip ohmic difference enhanced by H_2 bubbles or corrosion product[30], crack-front shape change governed by through-thickness potential difference, or microstructural heterogeneity[31]. While through-thickness potential differences and microstructural heterogeneities cannot be confirmed and should be relatively independent of thin film thickness, the buildup of corrosion product and entrapment of H_2 bubbles in the crack tip could potentially be the determining factor. In these small-volume thin film environments the exact morphology and distribution of these corrosion products would have an increased contribution towards established diffusion gradients with the surrounding bulk solution and could therefore increase this variability. As film thickness increases, larger solution volumes could more easily allow for corrosion product diffusion and H_2 bubble egress out of the crack tip, thus behaving closer to full immersion testing. This would decrease the crack tip ohmic drop and increase IG-SCC susceptibility, as is seen for these duplicates. Ultimately, this increased variability could be a result of the thin-film condition itself.

Despite the dual behavior there are several relevant finds for film thicknesses ≥92 µm. First, for the 184 and 229 µm thicknesses both duplicates exhibit a noticeably lower da/dt_{II} rates as compared to the 92 and 137 µm conditions. This may suggest that altering the oxygen diffusion distance via thin film thickness may have an effect on the maximum IG-SCC growth rate. While ohmic drop appears to be the primary governing factor of cathodic limitation in this IG-SCC system, as seen by the overall trend across all the thin film thicknesses, oxygen diffusion effects could still play a minor role once the critical thickness for cathodic limitation is surpassed. This trend corresponds well with the estimated values for the maximum diffusion layer of oxygen as all of these tested thicknesses are encompassed by even conservative estimates. This would suggest that should thicker films be tested, nominally above 250 µm, this trend would taper off.

Second, another trend observed in Figures 3.8c-d is that for films greater than 92 µm one of the duplicates for each thickness exhibited a noticeably lower K_{Th} than the maximum IG-SCC susceptibility condition (full immersion). The da/dt_{II} for these tests remain at values consistent with full immersion testing, however, indicating that this trend derives solely from a factor affecting the onset of IG-SCC (Stage I cracking). Under the assumption that cathodic limitation is limited in these thicker film conditions and solution geometry is not the contributing factor, it stands to reason that the culprit is most likely crack tip chemistry development. Lower total solution volumes, as compared to full-immersion, would allow for a greater chemistry buildup near the crack tip due to the lack of a bulk solution "buffer." This could in turn allow for lower pH levels and higher corrosion product buildup, ultimately generating higher amounts of H and embrittlement. This is corroborated by the high stress-assisted IGC rates observed in these environments that are noticeable faster than recorded IGC rates for this alloy lot (~1×10^{-6} mm/s)[22]. It is therefore likely this trend is due to inherent problems with keeping low volume thin film solutions at a constant solution chemistry across multiple tests.

3.5.3. Electrochemical potential observations

Analysis of electrochemical potential data collected during testing (Figures 3.9a-c) reveal a strong correlation between IG-SCC crack growth kinetics and bulk potential of the sample surface. This behavior is consistent with prior findings and is understood via a mixed-potential theory paradigm[20]. Specifically, where there are anodic reactions occurring at the crack tip and the respective cathodic reactions occurring along the bulk and crack wake surfaces. As anodic demand increases due to increased IG-SCC reaction rates and/or crack tip extension (thus revealing unpassivated β and α phase), higher cathodic currents are also demanded in order to sustain them. Assuming cathodic reaction kinetics remain constant during a test duration, increased cathodic current can only be obtained by manipulation of the bulk surface potential. Therefore, as anodic demand at the crack tip increases the bulk potential must decrease accordingly. Should cathodic reaction kinetics change significantly due to increased oxygen diffusion due to thinner solution films, however, the magnitude of these trends would be altered. It is therefore important to further investigate how these trends can vary across multiple cathodic kinetics as they may give insight into the changes in oxygen variability observed across the thin film thicknesses.

Using the mixed-potential theory paradigm discussed above, trends in the electrochemical potential observed during testing are easily explained. Prior to reaching the K_{TH} the OCP is seen to remain relatively constant at resting OCP values expected for this alloy. If any drift is observed it is relatively erratic and in line with previously noted OCP drift behaviors observed. Upon reaching stress intensities near the K_{TH}, however, the OCP is seen to steadily decrease by about 80 mV. This behavior is expected, as once the K_{TH} is reached IG-SCC mechanisms are activated and crack growth rates increase. Increased crack growth rates lead to further β phase dissolution and exposed unpassivated α phase, thereby resulting in increased anodic demands. This induces a consequent drop in the bulk surface potential to provide the necessary balancing cathodic current. While K_{TH} acts as a useful indicator of when this decrease in OCP will occur, this onset was also noted to correlate well with achieving crack growth rates of roughly 1×10^{-4} mm/sec. This critical crack growth rate is likely the point at which anodic demand from the IG-SCC mechanism outweighs that which can be provided ambiently by this specific alloy at OCP. Therefore, this critical crack growth is suspected to be highly dependent on sample geometry, alloy composition, and solution composition. After this decrease, the OCP is seen to halt once Stage II crack growth rates are achieved, remaining at roughly this lower value until test termination. During Stage II crack growth IG-SCC rates remain constant, therefore there is no longer an increasing amount of anodic demand and bulk potential no longer needs to decrease further. Sharp, negative spikes are sometimes observed in this phase, resulting from ductile tearing and sudden passivation of fresh material, but otherwise the OCP remains constant at this lower potential.

For 5xxx-series alloys, the electrochemical potential has been identified as a governing factor for the ultimate crack growth rates observed[20,40,42]. Measurements of OCP values taken at key points during testing are shown in Table 3.2, and indicate that all tests began at values of roughly -0.8 V_{SSC} and finished with values of around -0.88 V_{SSC}. However, despite similar electrochemical potentials a wide range of IG-SCC susceptibilities are observed across the tests as seen in Figure 3.10. These electrochemical values correlate generally well with full immersion, potentiostatically-controlled testing, with -0.8 V_{SCE} serving as the upper bound for IG-SCC susceptibility and more cathodic potentials leading to lower IG-SCC susceptibilities. Spread in IG-SCC susceptibility across tests at the same nominal electrochemical potential is still unaccounted for, however. This discrepancy may result from ohmic drop inherent to the SSC probe placement. Similar to the cathodic current supplying the anodic dissolution at the crack tip, ohmic drop between the SSC probe position and the bulk surface is significant and similarly dependent on the thin film thickness. As thin film thickness decreases, ohmic drop between the SSC probe and the bulk surface increases and the recorded potential could be altered. The effect of ohmic drop on recorded SSC potential reading in a thin film was observed in a previous paper, although in that study ohmic drop was shown to be limited (~5 mV) and was altered via probe distance from the crack tip and not film thickness[20]. Alternatively, this spread in IG-SCC behavior could be due to increased oxygen availability at the bulk surface. An increase in oxygen diffusion to the bulk surface would allow for increased cathodic reaction kinetics and greater cathodic currents at higher electrochemical potentials. Thus, in line with the mixed-potential paradigm discussed above, the bulk surface would not be required to decrease as much to provide the same amount of cathodic current and could remain at a more anodic potential.

3.6. Conclusions

A novel protocol for conducting LEFM-based IG-SCC testing under thin film environments was established through implementation of AAO membranes. The IG-SCC susceptibility of the alloy AA5083-H131 sensitized at 100°C to a NAMLT value of 40 mg/cm^2 was assessed at various nominal thin film thicknesses ranging from 54 to 229 µm using this protocol. Tensile testing was performed with high-resolution crack growth monitoring using the dcPD method in 0.6 M NaCl electrolyte. All subcritical crack growth data were analyzed using the elastic-plastic K_J. Use of an SSC probe allowed for in situ electrochemical potential measurements and insights. Based on these results, the following conclusions are established.

- Verification experiments coupled with finite element simulations indicate that the AAO-based approach for implementing thin film environments will not significantly affect oxygen diffusion kinetics or the ohmic resistance of the thin film.
- For a constant electrolyte composition, testing of AA5083-H131 in thin film environments suggests increased IG-SCC susceptibility past a critical thickness consistent with known geometry-induced cathodic limitation behaviors.
- For thin film thicknesses past a critical thickness, a dual behavior was observed between duplicates. The origin of this behavior, whether procedural or actual, is unknown.
- Results suggest that oxygen diffusion rates through the thin film geometry had a minor effect as compared to ohmic drop through the solution.
- Fluctuations in the OCP of the bulk surface directly correlated with trends in the crack growth kinetics for all observed thin film thicknesses.

3.7. Acknowledgements

This research was financially supported by the Office of Naval Research with Dr. Airan Perez as the Scientific Officer. Professor R.G. Kelly and Ryan Katona have also provided indispensable insight into the development and validation of this testing development and interpretation of the results.

3.8. References

1. Z.Y. Chen, F. Cui, and R.G. Kelly, *J. Electrochem. Soc.* 155 (2008): p. C360.
2. Z.Y. Chen, and R.G. Kelly, *J. Electrochem. Soc.* 157 (2010): p. C69.
3. C. Liu, J. Srinivasan, and R.G. Kelly, *J. Electrochem. Soc.* 164 (2017).
4. N.D. Tomashov, Development of the Electrochemical Theory of Metallic Corrosion (1964).
5. M. Stratmann, *Corrosion Science* 30 (1990): pp. 697-714.
6. M. Stratmann, H. Streckel, K.T. Kim, and S. Crockett, 30 (1990): pp. 715–734.

7. G.S. Frankel, M. Stratmann, M. Rohwerder, A. Michalik, B. Maier, J. Dora, and M. Wicinski, *Corros. Sci.* 49 (2007): pp. 2021–2036.
8. M. Stratmann, *Corrosion Science* 30 (1990): pp. 681-696.
9. O. Dolgikh, A. –S Demeter, S. V. Lamaka, M. Taryba, A.C. Bastos, M.C. Quevedo, and J. Deconinck, *Electrochim. Acta* 203 (2016): pp. 379–387.
10. T.H. Muster, A. Bradbury, A. Trinchi, I.S. Cole, T. Markley, D. Lau, S. Dligatch, A. Bendavid, and P. Martin, *Electrochim. Acta* 56 (2011): pp. 1866–1873.
11. B. Krawczyk, P. Cook, J. Hobbs, and D.L. Engelberg, *Corros. Sci.* 142 (2018): pp. 93–101.
12. Z.Y. Liu, W.K. Hao, W. Wu, H. Luo, and X.G. Li, *Corros. Sci.* 148 (2019): pp. 388–396.
13. W. Wu, Z. Liu, S. Hu, X. Li, and C. Du, *Ocean Eng.* 146 (2017): pp. 311–323.
14. N. Mi, M. Ghahari, T. Rayment, and A.J. Davenport, *Corros. Sci.* 53 (2011): pp. 3114–3121.
15. J.S. Warner, *PhD Diss. Dep. Mater. Sci. Eng.* Ph.D. Diss (2010).
16. G.G. Scatigno, P. Dong, M.P. Ryan, and M.R. Wenman, *Materialia* 8 (2019): p. 100509.
17. D.T. Spencer, M.R. Edwards, M.R. Wenman, C. Tsitsios, G.G. Scatigno, and P.R. Chard-Tuckey, *Corros. Sci.* 88 (2014): pp. 76–88.
18. V.N. Rafla, P. Khullar, R.G. Kelly, and J.R. Scully, *J. Electrochem. Soc.* 165 (2018): pp. C562–C572.
19. P. Khullar, J. V. Badilla, and R.G. Kelly, *ECS Electrochem. Lett.* 4 (2015): pp. C31–C33.
20. P. Steiner, and J. Burns, *Corrosion* 74 (2018): pp. 1117–1131.
21. M.L.C. Lim, R.G. Kelly, and J.R. Scully, *Corrosion* 72 (2016): pp. 198–220.
22. M.E. Mcmahon, P.J. Steiner, A.B. Lass, and J.T. Burns, *Corrosion* 73 (2017): pp. 347–361.
23. M.L.C. Lim, "Intergranular Corrosion Propagation in Sensitized Al-Mg Alloys," 2016.
24. R.P. Gangloff, D.C. Slavik, R.S. Piascik, and R.H. Van Stone, *Small Crack Test Methods* (1992): pp. 116–168.
25. M.E. Mcmahon, P.J. Steiner, A.B. Lass, and J.T. Burns, *Corrosion* 73 (2017): pp. 713–723.
26. H. Tada, P. Paris, and G. Irwin, "The Stress Analysis of Cracks Handbook" (St. Louis, MO: Paris Productions Incorporated, 1985).
27. E647-15e1. Standard Test Method for Measurement of Fatigue Crack Growth Rates. *ASTM B. Stand.* 1–49 (2016). doi:10.1520/E0647-15E01.2

28. T. Anderson, “Fracture Mechanics: Fundamentals and Applications,” 3rd ed. (Boca Raton, FL: CRC Press, 2005).

29. V. Kumar, M.D. German, and C.F. Shih, “An Engineering Approach for Elastic-Plastic Fracture Analysis” (1981).

30. C.B. Crane, R.G. Kelly, and R.P. Gangloff, *Corrosion* 72 (2016): pp. 242–263.

31. C.B. Crane, and R.P. Gangloff, *Corrosion* 72 (2016): pp. 221–241.

32. Z.D. Harris, E.M. Dubas, A.S. Popernack, B.P. Somerday, and J.T. Burns, *Theor. Appl. Fract. Mech.* (n.d.): p. in review.

33. P. Steiner, and J. Burns, *ICF 2017 - 14th Int. Conf. Fract.* 1 (2017): pp. 566–567.

34. R.P. Gangloff, H.M. Ha, J.T. Burns, and J.R. Scully, *Metall. Mater. Trans. A* 45 (2014): pp. 3814–3834.

35. R.G.K. R. M. Katona, S.Tokuda, J. Perry, “Design, Construction and Validation for in-Situ Water Layer Thickness Determination during Accelerated Corrosion Testing” (n.d.).

36. A. Okubo, *Q. Rev. Biol.* 62 (1987): pp. 131–131.

37. R.T. Ferrell, and D.M. Himmelblau, *J. Chem. Eng. Data* 12 (1967): pp. 111–115.

38. W. Xing, G. Yin, and J. Zhang, “Oxygen Solubility, Diffusion Coefficient, and Solution Viscosity. Rotating Electrode Methods and Oxygen Reduction Electrocatalysts” (Elsevier B.V., 2004).

39. R.H. Jones, D.R. Baer, M.J. Danielson, and J.S. Vetrano, *Metall. Mater. Trans. A* 32 (2001): pp. 1699–1711.

40. M.E. McMahon, J.R. Scully, and J.T. Burns, *Jom* 69 (2017): pp. 1389–1397.

41. A.D. King, J.S. Lee, and J.R. Scully, *J. Electrochem. Soc.* 163 (2016): pp. 342–356.

42. C.B. Crane, R.G. Kelly, and R.P. Gangloff, *Corrosion* 72 (2016): pp. 242–263.

Chapter 4. Effect of solution chloride concentration

4.1. Abstract

The effect of chloride concentration on the IG-SCC behavior of AA5083-H131 in atmospheric environments was investigated using fracture mechanics-based testing, high fidelity monitoring of crack growth kinetics, and electrochemical potential measurements. Critically, the IG-SCC susceptibility was found to increase across all environments as chloride concentration increased, denoted by a decrease in the K_{TH} and larger da/dt_{II} crack growth rates. Furthermore, IG-SCC susceptibility decreased across all chloride concentrations as cathodic limitation due to solution geometry effects increased. These results are analyzed in the context of a coupled anodic dissolution and H-embrittlement mechanism, wherein the increase in IG-SCC susceptibility for higher chloride concentrations results from increased overpotentials at the crack tip for hydrogen production and the decrease in IG-SCC susceptibility from solution geometry results from cathodic limitation of the governing IG-SCC mechanism, leading to a decrease in the dissolution at the crack tip, a less aggressive crack chemistry development, and thus lower levels of H production. A close correlation between the OCP of the bulk surface and the crack growth kinetics was also observed across all environments and chloride concentrations, with higher chloride concentrations and cathodic limitations resulting in larger changes in electrochemical potential. This correlates well with known potential-dependent IG-SCC observations for these alloys.

4.2. Introduction

To date studies on IGC and IG-SCC susceptibility in Al-Mg alloys have primarily been performed with specimens fully immersed in solutions of constant electrolyte compositions[1–8] and a maintained electrochemical potential[1,2]. While these conditions provide repeatable results and ease of setup, they may fail to correlate with realistic atmospheric environments. These atmospheric environments are typically defined by low solution volumes, lack of any external electrochemical control, and high electrolyte chloride concentrations. Investigation into the isolated effects of solution geometry and lack of electrochemical control in Al-Mg alloys have been investigated in previous chapters and show that these factors can have strong effects on the observed crack growth rates, even when held at a constant electrolyte composition[9]. It was shown that upon removal of a governing potentiostat, cathodic reactions necessary for the IG-SCC mechanism were transferred unto the bulk surface. This cathodic transfer is in-line with established pitting studies, wherein the bulk surface surrounding an anodic site was found to provide the balancing cathodic current for IGC[10,11]. Additionally, it was found that the solution geometry had a distinct effect on the available cathodic current that could be provided. By reduction of the balancing cathodic area through physical masking or ohmic resistance the anodic reactions occurring at the crack tip (and therefore resulting IG-SCC crack growth rates dependent on those reactions) could be stifled through cathodic limitation.

While the effects of atmospheric solution geometries and cathodic source effects have been shown in Al-Mg alloys, the electrolyte solution composition has also been shown to have a large impact on IG-SCC susceptibility[12,13]. In addition to higher amounts of contaminants and pollutants that may also impact the IG-SCC mechanism, atmospheric environments are also prone to higher chloride molarities than those typically seen in full immersion. This can occur due to either evaporation and concentration of bulk chloride solutions or the deliquescence of water vapor onto previously deposited salt deposits. When tested in full-immersion studies, higher chloride levels are often directly correlated with higher levels of IG-SCC susceptibilities. In a study by McMahon *et al.* it was observed that IG-SCC susceptibilities of Al-Mg alloys tested in different chloride concentrations closely correlated with the corresponding dependence of the pitting potentials of the β and α phases on chloride concentration. Specifically, high IG-SCC susceptibilities at potentials above the β and α pitting potentials, intermediate IG-SCC susceptibility above the β phase pitting potential and below α pitting potentials, and low IG-SCC susceptibility below both the β and α phase pitting potential[12]. As chloride concentrations increased, leading to shifts in the breakdown potentials of both phases to more negative potentials, higher IG-SCC susceptibilities were observed across the same applied electrochemical potential. Therefore, this trend suggests that the effect of chloride concentration on the IG-SCC susceptibility is largely due to a modification of the pitting potentials which determine anodic dissolution rates and hydrogen production at the crack tip. This trend is further supported by the studies of Crane *et al.*, who show that electrochemical potential has a large contribution to IG-SCC susceptibility due to its effect on the crack tip chemistry development[13]. Critically, it was demonstrated that when an occluded crack tip chemistry was achieved, either through electrochemical control or modification of the bulk solution, higher crack growth rates were achieved even in relatively unsensitized as-received alloys.

Although the effects of chloride concentration are rather clear in full immersion, potentiostatically-controlled conditions, atmospheric environments present additional factors that may alter these trends. Firstly, due to removal of the potentiostat and transfer of the cathode to the bulk surface the conductivity of the solution must now be considered. Higher ionic molarities result in higher conductivities, therefore ohmic resistances through the electrolytic solution will be decreased and larger cathodic areas could be supported[11]. Consequently, higher IG-SCC crack growth rates may be achieved before the onset of solution geometry induced cathodic limitation effects. Secondly, due to decreased solution volumes the initial bounding conditions for crack tip chemistry development may be altered from that of full immersion. Full immersion conditions have bulk solutions constantly in contact with the crack tip with volumes orders of magnitude larger than the crack tip, thus they able to provide adequate ionic diffusion and act as a buffer. Atmospheric environments, which have less solution in contact with the crack tip, may not be able to provide similar support and could thus alter crack tip chemistry development.

4.2.1. Chapter objective

The primary objective of this paper is to isolate and investigate the effects of chloride concentration on the IG-SCC of Al-Mg alloys in atmospheric environments. To this end, there are three main goals. First, a variety of chloride concentrations will be tested across multiple atmospheric environments to determine if the overall trend of chloride concentration from full immersion studies remains the same. Second, the effects of solution geometry on this trend will be observed, specifically if lower solution geometries amplify or dampen these trends. Lastly, the trends observed in the electrochemical data will be analyzed and interpreted in relation to the previous observations.

4.3. Experimental methods and material

4.3.1. Materials and sample prep

In this study the Al-Mg alloy engineering alloy AA5083-H131 was investigated. The source, thickness, and composition of this alloy is reported in Table 2.1. The temper designation indicates that this alloy has been strain hardened, retaining 3/8 of the residual hardening[14]. The Ramberg-Osgood parameters and results of a grain size analysis are reported in Table 2.2. Prior LEFM based testing in 0.6 M NaCl of this exact production lot of material demonstrated that high susceptibility to IG-SCC at a NAMLT value of 40 mg/cm^2 in 0.6 M NaCl[9]. Additional microstructure and sensitization analysis on this alloy are detailed elsewhere[1].

Single edge notch tensile (SENT) specimens of the AA5083-H131 alloy were machined with an S-L orientation (loading applied in S direction, crack growth in L direction) and polished to 400 grit finish. The samples have a gauge width of 17.33 mm and thickness of 6.62 mm. A 1.52 mm deep electrically discharged machined (EDM) notch was placed at the mid-point of the gauge section which aligned with the center (T/2) location in the S-direction of the plate. Samples were then sensitized at 100°C for 336 hours to achieve the desired NAMLT value of 40 mg/cm^2 based on previously established sensitization curves for these material lots derived from ASTM G67 testing[15].

4.3.2. Mechanical testing

All fracture tests were conducted using software-controlled, servo-hydraulic frames with active crack length feedback via the direct current potential difference (dcPD) method.[29]

Potential readings were taken via copper wires (0.127-mm diameter) coated in perfluoroalkoxyalkane spot welded 0.5 mm ± 0.1 mm from the center of the EDM notch with a 6 A constant current passing through the sample. These potential readings were then taken every 30 s in a process reported by McMahon, et al.,[6,12] and converted to an instantaneous crack length using the Johnson's equation, resulting in crack growth resolution of roughly 0.5 µm.[6]

Samples were loaded by means of freely rotating clevis grips, in compliance with stress intensity (K) boundary conditions.[30] They were fatigue precracked to a cumulative notch plus crack length of 2 mm at a constant K_{max} of 6 MPa·√m at a stress ratio ($R = K_{min}/K_{max}$) of 0.1 and a frequency of 8 Hz. The precrack length was then extended to 2.75 mm via a decreasing K protocol from a K_{max} of 6 MPa·√m to a K_{max} of 3.5 MPa·√m at a stress ratio of 0.1 and a frequency of 3 Hz. At this point a 2-kN load was applied to the precracked specimens (corresponding to a K_{max} of roughly 2 MPa·√m) and the testing environment was introduced; these conditions were held for 1 h to stabilize the initial crack tip and bulk surface chemistry. Following this 1 h hold samples were tested via slow-rising displacement at a rate corresponding to an initial dK/dt of roughly 0.25 MPa·√m/h. Tests were run until failure or the samples exhibited bulk scale plasticity.

Following test completion, linear post-processing crack length corrections were applied based on fracture surface analysis of the initial and final crack lengths. Crack growth rates were calculated from the tangent of a second order polynomial fit to 7 crack length vs time data points (akin to the protocol established for fatigue crack growth rates in ASTM E647[16]). Elastic-plastic stress intensity (K_J) analysis was also conducted using the 0.2% offset yield strength and Ramberg-Osgood constants for the alloys, derived via compressive testing and reported in Table 2.3, in compliance with previous literature[4,17,18]. A functional resolution limit due to localized (crack tip) plasticity introducing 'false' dcPD-measured crack extension was previously established for this production lot of AA5083-H131 lot and has a functional form of:[3,4]

$$\frac{da}{dt}_{False} = 5 \times 10^{-7} \cdot \exp(0.0577K) \qquad \text{(Eq. 4.1)}$$

Recent fracture mechanics experiments conducted in an inert environment (dry N_2 gas with RH < 5%) on a Ni-based superalloy using a fixed dK/dt testing protocol demonstrate that the dcPD-measured resolution limit scales linearly with dK/dt[19]. A correction protocol was then developed to subtract this 'false' da/dt contribution from measured da/dt, thereby enabling the ‘true’ da/dt to be determined for an experiment conducted under fixed dK/dt conditions[19]. Given that the current study utilizes testing at a fixed displacement rate, it is expected that dK/dt will begin to increase from the initial value of 0.25 MPa√m/hr once crack growth occurs. As such, it is incorrect to simply subtract Eq. 4.1 from measured da/dt vs. K relationships as was done in prior work[1,2,19,20] since Eq. 4.1 is only rigorously valid for dK/dt = 0.3 MPa√m/hr and therefore must be modified to incorporate an explicit dK/dt dependence. Given that the mechanistic basis for the scaling in the resolution limit is based solely on fracture mechanics principles[19,21] and is therefore nominally material-agnostic, a dK/dt dependence can be introduced into Eq. 4.1 via dividing the prefactor (5×10-7) in Eq. 4.1 by the dK/dt for the experiment to which Eq. 4.1 was fit (0.3 MPa√m/hr)6, yielding:

$$\frac{da}{dt}_{False} = 1.667 \times 10^{-6} \left(\frac{dK}{dt}\right) \cdot \exp(0.0577K) \qquad \text{(Eq. 4.2)}$$

In the current study, dK/dt was determined by numerically differentiating a smoothing spline fitted to the experimental K vs. time data using the Matlab curve fitting toolbox. A smoothing parameter (p) of 0.9 was utilized for fitting each individual experiment. The smoothing spline was selected for fitting the K vs. time profile due to an improved fit (quantified *via* R^2) over the entire time range relative to a power law or exponential function. Once the dK/dt vs. K relationship is known Eq. 4.2 can be utilized to calculate a test-specific resolution limit that accounts for the expected increase in dK/dt as cracking progresses. This ‘false’ da/dt can then be subtracted from the experimentally-measured da/dt to correct for effects of localized plasticity on the dcPD system[19].

4.3.3. Environmental setup

In this study three broad environmental categories were investigated: full immersion, misting, and wicked electrolyte directly into the crack. Further information on development and validation of these atmospheric environments can be found in a previous chapter[20]. Full-immersion conditions were conducted in a 200 mL Plexiglass cell, into which a 2 L reservoir of aerated 0.6 M NaCl solution at room temperature was circulated at a rate of 20 mL/min using a peristaltic pump. Two full-immersion conditions were investigated: (1) the test was run with no potential control and the OCP was allowed to float for the duration of the testing (termed FOCP in this paper) and (2) where a constant potential was set by the potentiostat. For full-immersion testing with no set potential, the exposed alloy surface area was masked 7.5 mm above and below the crack path plane (15 mm total height).

The misting protocol was designed to be representative of a constant salt-spray environment and was thus loosely based on ASTM B117.[34] To this end, a Plexiglass cell with a large radius and a sloped ceiling and floor was designed to promote air circulation and drainage of coalesced water away from the sample. Two 80° conical fine mist spray nozzles with an inner diameter of 0.35 mm were positioned at the cell perimeter on either side of the crack path and would continuously spray the sample from a 2 L reservoir of aerated 0.6 M NaCl solution at room temperature at a rate of roughly 40 mL/min. Drainage from the cell was collected and circulated back into the reservoir.

The condition wherein electrolyte was wicked directly into the crack (termed the "wicking condition") was designed to mimic conditions where electrolyte is contained only within the crack. For this condition, a wetted fiberglass wick was threaded through the sample notch, with one end located in a 100-mL input solute reservoir of aerated 0.6 M NaCl solution at room temperature and the other end leading into a separate output reservoir. This arrangement allowed the wick to act as a gravity siphon, in which electrolyte from the higher input reservoir would flow through the wick, into the notch, and into the lower output reservoir. This flow rate was not precisely measured but was estimated to be on order of 1 mL/h. The 100-mL input reservoir would be refilled daily with a fresh 0.6 M NaCl solution and would not be circulated from the output reservoir.

4.3.4. Electrochemical monitoring

For the full-immersion environments a potentiostat was used in floating ground mode (as the specimen was grounded through the loading frame) with a platinum mesh surrounding the sample as the counter electrode and saturated calomel electrode (SCE) probe as the reference. During LEFM testing of the misting and wicking environments the OCP was monitored via a 4-mm diameter sintered silver/silver-chloride (SSC) probe which acted as both a counter and reference electrode. Details of the governing electrochemical concepts, functional details/limitations of the probe application, and verification of the probe accuracy for thin film electrochemical measurements were demonstrated by Khullar, et al.[35] Notably, the probes were found to not impact the electrolyte composition, function well with currents up to 1 mA, and allow for accurate calculation of the ideal solution theoretical potential of these probes versus the standard hydrogen electrode (SHE) via the Nernst equation as long as the solution chloride concentration is known. As such, all the recorded electrochemical potentials collected via SSC probes will be translated with reference to an SCE reference electrode in this study to allow for direct comparison between all environments. During misting tests the probe was placed at the bottom of the exposed window on the side opposite the EDM notch (approximately 12 mm diagonally away from the notch tip for a 15 mm window). The probe was attached to the sample via 100 µm thick double-sided adhesive to slightly offset it from the sample surface. For wicking tests, the probe was placed in the outflow reservoir roughly 1 cm down the wick path from the sample notch. It is worth noting that in the probe configurations detailed above, distance from the crack tip to the SSC probe through thin/narrow ionic solution paths may lead to an increased electrical resistance. This can cause a change in the perceived potential due to ohmic drop, thus affecting the accuracy and validity of the SSC probe. While this is recognized as an area of concern and a potential source of error, due to the low currents involved in OCP measurements and the magnitude of the observed effects this should have a negligible consequence on the OCP interpretations in this study. Implementation and investigation on the accuracy of these probes in these atmospheric environments have been discussed further in a previous paper[20].

4.4. Results

4.4.1. Influence of environment on IG-SCC kinetics

Use of the dcPD method and slow rising displacement loading protocol described above allows for detailed analysis relating the crack growth rate, da/dt, versus the stress intensity, K_J. From these data the various stages of SCC crack growth can be determined and the IG-SCC dependent parameters derived. Traditionally the two parameters of interest are the K_{TH} and the Stage II crack growth rate (da/dt_{II}). The K_{TH} is demarcated as the stress intensity at the beginning of IG-SCC dominated fracture as opposed to stress-assisted intergranular corrosion (IGC). This is traditionally defined as the stress intensity at which crack growth exceeds the resolution limit. Due to the high susceptibility of AA5083-H131 at a NAMLT level of 40 mg/cm^2, however, stress-assisted IGC occurs at rates above this resolution limit and the K_{TH} is instead defined as the onset of Stage I cracking and a rapid increase in crack growth rate. The da/dt_{II} is defined as the crack growth rate which it is largely independent of increasing stress intensity; this has been postulated to be due to an H-diffusion limitation from the crack tip surface into the crack tip process zone[4,8]. This limitation causes a plateau in the da/dt vs K_J graph leading up to the KIC, at which point sub-critical HEAC based cracking is augmented by a ductile failure mechanism (possibly some stable ductile tearing then final rupture). It is worth noting that scatter has been observed in the da/dt vs. K_J relationship for samples from the same lot run under the same conditions, thus current data should be analyzed in the context of this inherent variability[4].

Crack growth vs stress intensity data for AA5083-H131 sensitized to NAMLT 40 mg/cm^2 for the various testing environments tested at various NaCl concentrations of 0.3 M, 0.6 M, 1.2 M, 2.4 M, and 5.45 M are reported in Figures 4.1a-e respectively. Values for the K_{TH}, which ranged from values of roughly 2 to 9 MPa√m, are listed in Table 4.1 for each testing environment and chloride concentration. Overall trends show a general decrease in K_{TH} across a constant environment as the chloride concentration was increased, with K_{TH} values of roughly 6 to 9 MPa√m at 0.3 M NaCl and K_{TH} values of roughly 2 to 4 MPa√m at 5.45 M NaCl. It should be noted, however, that values for 1.2 M NaCl exhibited higher K_{TH} values than expected across all four environments. Additionally, the K_{TH} was found to correlate well with expected levels of cathodic limitation across the environments with the most limiting environment (wicking) typically exhibiting the highest K_{TH} values and the least inhibited environment (Imm -800 V_{SCE}) exhibiting the lowest. The misting and Imm FOCP environments, which have an intermediary amount of cathodic limitation, were seen to behave similarly and were largely bounded by the wicking and Imm -800 V_{SCE} environments. These trends are visually represented in Figure 4.2. Values for the da/dt_{II}, which range from roughly 1.3×10^{-4} mm/s to 3.5×10^{-3} mm/s, are listed in Table 4.2 for each testing environment and chloride concentration. Overall trends show that the da/dt_{II} increased as both chloride concentration increased and cathodic limitation decreased. It should be noted, however, that all the 0.6 M NaCl tests exhibited higher da/dt_{II} rates than expected compared to the other concentrations. These trends are visually represented in Figure 4.3.

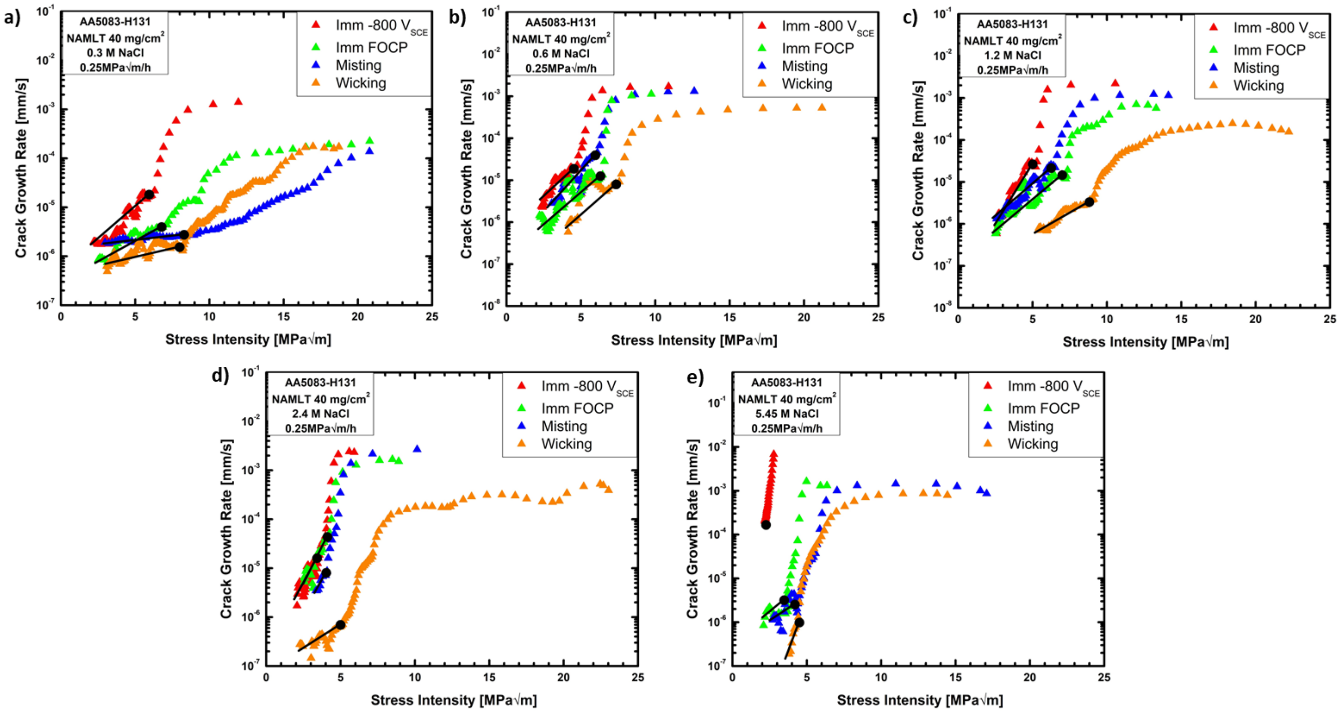

Figure 4.1. Crack growth rate vs. stress intensity for AA5083-H131 at a NAMLT values of 40 mg/cm^2 for chloride concentrations of a) 0.3 M NaCl, b) 0.6 M NaCl, c) 1.2 M NaCl, d) 2.4 M NaCl, and e) 5.45 M NaCl. The stress-assisted IGC regime and K_{TH} for each test are represented by a black line and circle, respectively.

Table 4.1. Recorded K_{TH} (MPa√m) values for each environment and chloride concentration.

Solution Concentration	Imm -800	FOCP	Misting	Wicking
0.3	6.08	6.87	8.64	8.11
0.6	4.59	6.47	5.46	7.49
1.2	5.09	7.12	6.44	8.98
2.4	3.48	4.29	4.04	5.03
5.45	2.15	3.67	4.22	4.41

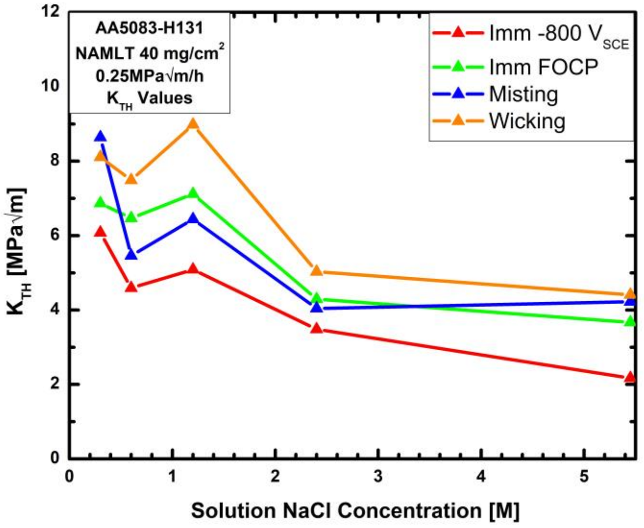

Figure 4.2. Graphical representation of K_{TH} values for AA5083-H131 at a NAMLT values of 40 mg/cm^2 across all solution geometries and chloride concentrations.

Table 4.2. Recorded da/dt_{II} (mm/s) values for each environment and chloride concentration.

Solution Concentration	Imm -800	FOCP	Misting	Wicking
0.3	$1.42\text{x}10^{-3}$	$1.94\text{x}10^{-4}$	$1.37\text{x}10^{-4}$	$1.78\text{x}10^{-4}$
0.6	$1.73\text{x}10^{-3}$	$1.15\text{x}10^{-3}$	$1.28\text{x}10^{-3}$	$7.73\text{x}10^{-4}$
1.2	$2.23\text{x}10^{-3}$	$6.63\text{x}10^{-4}$	$1.28\text{x}10^{-3}$	$2.42\text{x}10^{-4}$
2.4	$2.49\text{x}10^{-3}$	$1.55\text{x}10^{-3}$	$2.71\text{x}10^{-3}$	$3.13\text{x}10^{-4}$
5.45	$8.16\text{x}10^{-3}$	$1.42\text{x}10^{-3}$	$1.48\text{x}10^{-3}$	$8.81\text{x}10^{-4}$

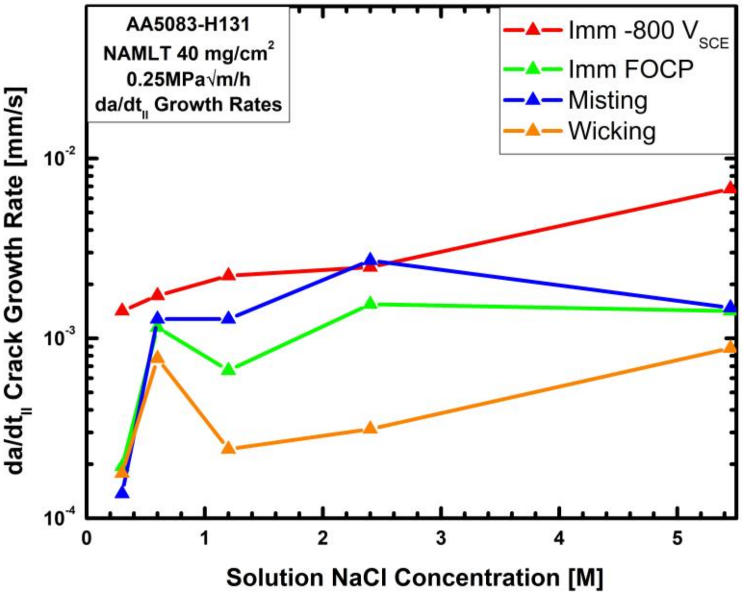

Figure 4.3. Graphical representation of da/dt$_{II}$ crack growth rates for AA5083-H131 at a NAMLT values of 40 mg/cm^2 across all solution geometries and chloride concentrations.

In summary, three overarching trends are apparent. First, K_{TH} values were found to generally decrease as chloride concentration increased and expected cathodic limitation due to solution geometry decreased. Second, da/dt$_{II}$ values were found to generally increase as chloride concentration increased and expected cathodic limitation due to solution geometry decreased. Lastly, the differences in K_{TH} and da/dt$_{II}$ between the two bounding cathodic limitation inducing geometries remained relatively constant as solution concentration increased.

4.4.2. Electrochemical potential observations

Applied potential strongly impacts the IG-SCC susceptibility of 5xxx series aluminum alloys[4,12]. This observation was extended to atmospheric conditions in a prior work where changes in the bulk surface potential directly correlated to IG-SCC crack progression[9]. As such the potential was monitored during testing in an attempt to correlate trends in the OCP to the crack growth kinetics. Examples of collected OCP plots are shown in Figure 4.4 for 0.3 M NaCl FOCP (Figure 4.4a), 1.2 M NaCl misting (Figure 4.4b), and 5.45 M NaCl wicking (Figure 4.4c). Common trends correlating to the different crack growth regimes are observed, as seen and reported in previous studies on this material lot[9][TF Ref]. These trends are: (1) a slight or negligible drift in the OCP prior to the K_{TH}; (2) a more significant and constant decline in OCP during Stage I and Stage II crack growth; and (3) reaching of a minimum OCP close to sample failure with sharp negative spikes in the OCP during sudden ductile failure events. For the wicking tests, however, a variation in trend 1 was observed wherein upon initiation of the SCC test the electrochemical potential was found to decrease suddenly before steadily increasing until roughly the K_{TH}. These regimes are delineated in Figures 4.4 by marking the K_{TH} and K_F (stress intensity upon final failure) on the plots with vertical lines. Values of the OCP at the initiation of SCC testing (E_I), at the K_{TH} (E_{TH}), and at K_F (E_F) are reported in Table 4.3 for all environmental conditions and chloride concentrations.

Table 4.3. Values of the OCP (V_{SCE}) at the start of SCC Testing (E_I), at the K_{TH} (E_{TH}), and at K_F (E_F) for all environments and chloride concentrations. Values are color-coded to illustrate the scale from more anodic potentials (green) to more cathodic potentials (red).

		0.3 M NaCl	0.6 M NaCl	1.2 M NaCl	2.4 M NaCl	5.45 M NaCl
Imm FOCP	E_I	-0.781	-0.845	-0.827	-0.869	-0.818
	E_{TH}	-0.784	-0.897	-0.877	-0.871	-0.822
	E_F	-0.853	-0.952	-0.894	-0.913	-0.831
Misting	E_I	-0.808	-0.809	-0.832	-0.845	-0.92
	E_{TH}	-0.794	-0.823	-0.84	-0.848	-0.919
	E_F	-0.829	-0.883	-0.873	-0.91	-1.01
Wicking	E_I	-0.845	-0.937	-0.877	-0.903	-0.857
	E_{TH}	-0.836	-0.891	-0.937	-0.941	-0.956
	E_F	-0.868	-0.915	-0.994	-1.01	-0.994

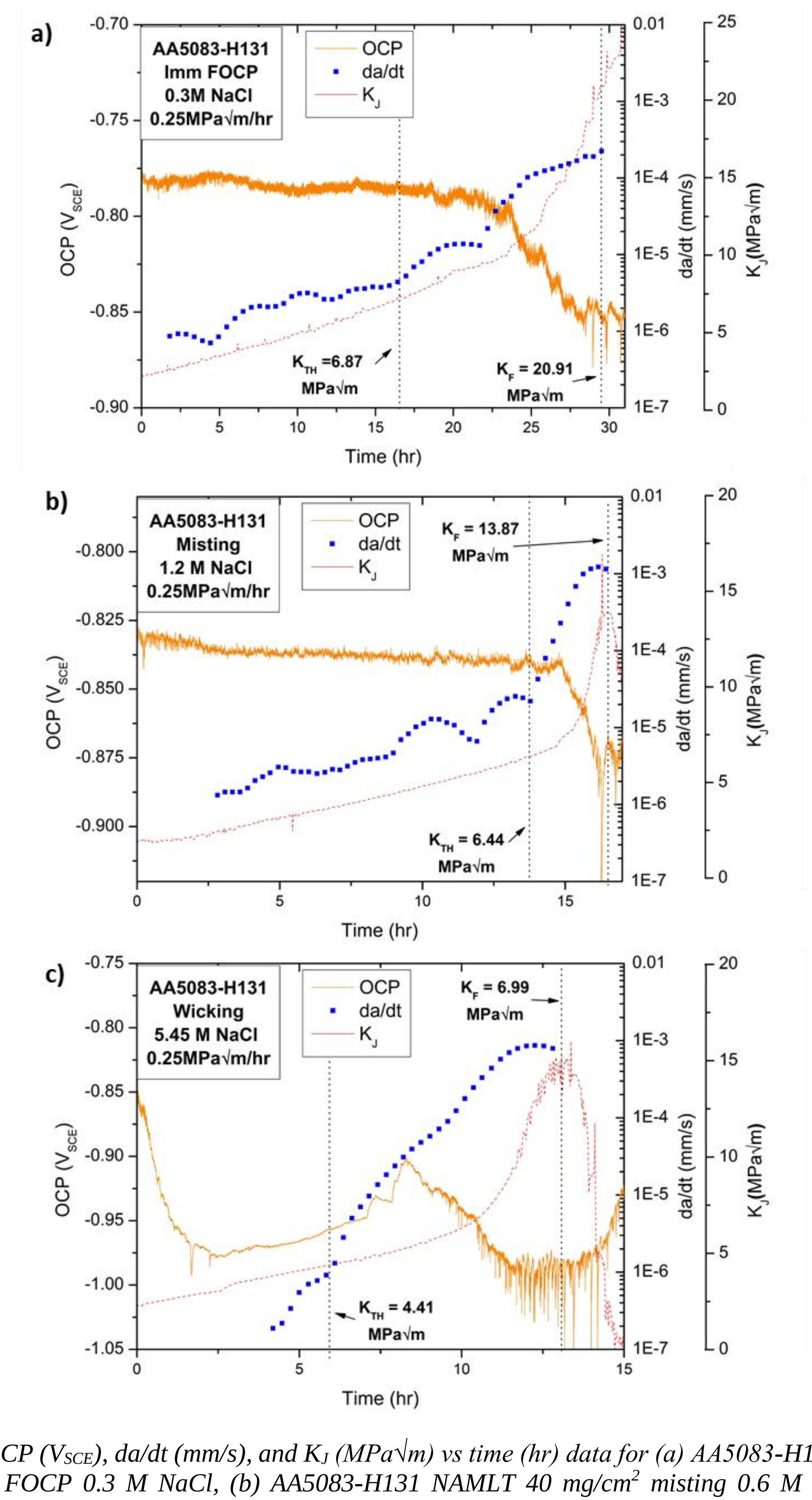

Figure 4.4. OCP (V_{SCE}), da/dt (mm/s), and K_J (MPa√m) vs time (hr) data for (a) AA5083-H131 NAMLT 40 mg/cm^2 Imm FOCP 0.3 M NaCl, (b) AA5083-H131 NAMLT 40 mg/cm^2 misting 0.6 M NaCl, and (c) AA5083-H131 NAMLT 40 mg/cm^2 wicking 5.45 M NaCl.

4.5. Discussion

This discussion will be divided into three parts, each focusing on a goal outlined in this paper. First, the general effects of chloride concentration on IG-SCC crack growth rates will be discussed independent of testing environment. Figure 4.1 demonstrates that a trend similar to that seen in full immersion studies occurs, with higher solution chloride concentrations resulting in lower K_{TH} values and higher da/dt_{II} rates. Second, the magnitude of these chloride concentration-induced effects across each environment will be analyzed and discussed. Lastly, any trends seen in the previous results will be correlated to trends observed in the collected electrochemical data. All results will be interpreted in the context of a cathodic limitation framework, in which anodic demand from an anodic dissolution and hydrogen embrittlement mechanism is being limited by ohmic drop of the supporting cathodic area surrounding the crack tip through the electrolytic solution.

4.5.1. Effect of chloride concentration on IG-SCC susceptibility

From full immersion studies performed on Al-Mg alloys it is well known that trends in IG-SCC susceptibility are closely tied to the chloride concentration of the testing solution. McMahon *et al*. demonstrated for AA5456-H116 that as chloride concentration is increased for IG-SCC tests run at constant potentials the K_{TH} is found to decrease and the da/dt_{II} rates are seen to increase[12]. Critically, the chloride concentrations were found to alter the breakdown potentials of the β and α phases (-0.95 V_{SCE} and -1.02 V_{SCE} at 0.6 M NaCl and 5.45 M NaCl respectively for $E_{pit(\beta)}$, -0.7 V_{SCE} and -0.85 V_{SCE} at 5.45 M NaCl respectively for $E_{pit(\alpha)}$[12]) with high IG-SCC susceptibilities above these potentials, intermediary susceptibility between these potentials, and low susceptibility below these potentials. Breakdown of these phases at the crack tip are necessary for the proposed IG-SCC mechanism as this will lead to further crack tip acidification, hydrogen production, hydrogen embrittlement, and ultimately crack growth. It is therefore expected that for each individual environment, or cathodic limitation system, the IG-SCC kinetics will behave similarly and show increased IG-SCC susceptibility as chloride concentration increases (distinguished by lower K_{TH} values and higher da/dt_{II} rates). These effects may be dampened or augmented by geometric effects or a floating electrochemical potential, which will be discussed in a later section, but should otherwise conform to the trends seen in full immersion set potential testing.

In regards to K_{TH} values, it is seen from Figure 4.2 that as solution concentration increases for most environments the K_{TH} generally decreased. Disregarding the potential effects due to a floating electrochemical potential, this is consistent with trends in the literature. As chloride concentration increases, the breakdown potentials for the β and α phases decreases, thus creating larger overpotentials for anodic dissolution and hydrogen production at the crack tip. Larger amounts of hydrogen production will therefore lead to larger amounts of hydrogen embrittlement, resulting in lower stress intensities required to initiate the IG-SCC mechanism. Interestingly, despite the overall trend seen there are two minor observations worth meriting: 1) consistently lower K_{TH} for the 0.6 M NaCl concentration and 2) consistently higher K_{TH} for the 1.2 M NaCl concentration. While these may in fact be actual trends observed in the testing, more testing would be needed to verify these trends as they fall largely in the variation that has been observed in the K_{TH} for this alloy lot (± 1 MPa√m)[3].

In regards to da/dt_{II} values, it is seen from Figure 4.3 that as solution concentration increases for most environments the da/dt_{II} crack growth rates generally increased. Again, disregarding the potential effects due to a floating electrochemical potential, this is consistent with previous trends in the literature[12]. The exact derivation of this trend is unknown, as bulk solution chloride concentrations are expected to have little effect on the crack tip chloride concentration once an occluded crack tip chemistry necessary for IG-SCC has already been developed. Therefore, this behavior is more likely to originate from changes in the cathodic kinetics on the bulk surface. Larger cathodic current densities, either through modification of the bulk OCP or increased oxygen diffusion rates due to thinner geometries, could allow for larger cathodic contributions that would fuel the da/dt_{II} crack growth. The consistently higher da/dt_{II} rates for the misting condition over the FOCP condition corroborate this postulation well, as the misting condition is expected to have higher oxygen diffusion rates despite a similar cathodic area. This fails to address the increased da/dt_{II} values also observed for the Imm -800 mV_{SCE} condition, however, and thus merits further investigation. In Figure 4.3 two further minor observations are worth mentioning: 1) consistently lower da/dt_{II} crack growth rates for the non-polarized environments in 0.3 M NaCl concentration and 2) consistently higher da/dt_{II} crack growth rates for the non-polarized environments in 0.6 M NaCl concentration. Once again whether these are actual trends observed or experimental variability is unknown as these once again fall within reported variabilities for this alloy lot[3].

4.5.2. Effect of chloride concentration on atmospheric cathodic limitation-induced effects

In discussing the effect of chloride concentration on IG-SCC growth in atmospheric conditions, it is first useful to outline the various environments and the expected amounts of cathodic limitation one would expect. The first condition, full immersion testing with a set potential, is expected to exhibit the highest IG-SCC susceptibility in all cases due to its bulk solution coverage and governing potentiostat which allows for an 'infinite' cathode. For the FOCP condition the same bulk solution geometry is used, minimizing ohmic resistance through solution, but removal of a governing potentiostat will transfer the cathode to the sample surface. When this solution geometry is reduced to a thin film across the sample surface, such as in the misting condition, ohmic resistance through the solution may play a greater role and lead to greater amounts of cathodic limitation. Lastly the wicking condition, which has neither a governing potentiostat or a large area of ionically connected surface to serve as a cathode, should behave as the most cathodically limited condition. For all these environments the chloride concentration is expected to affect the maximum amount of cathodic limitation, as the chloride concentration will alter the solution conductivity and therefore anticipated ohmic resistance through the solution. While this may add variability to the cathodic limitation induced at various chloride concentrations, should the conductivity negate all ohmic resistance or increase it enough to electrically isolate the crack tip the results should still be bounded by the FOCP and wicking conditions, respectively. Therefore, across all concentrations one would expect the full immersion at a set potential to exhibit the least cathodic limitation, followed by the FOCP, misting, and wicking respectively.

Since cathodic limitation is directly correlated to the anticipated IG-SCC susceptibility, conditions with higher cathodic limitations should exhibit higher K_{TH} values and lower da/dt_{II} rates with the opposite holding true for lower cathodic limitations. This trend holds generally true for the K_{TH} values shown in Figure 4.2 and for the da/dt_{II} values shown in Figure 4.3 for the wicking, FOCP, and Imm -800 m_{VSCE} conditions. The misting condition, however, showed greater variability for both parameters and had consistently higher da/dt_{II} rates than the FOCP condition. This trend may simply be result from experimental variation, as both the misting and FOCP condition were seen to behave similar across most concentrations, and could be resolved with further replication testing. It should be noted that similar behavior between these conditions does seem to indicate that the misting condition does not provide significantly increased ohmic resistance compared to the FOCP condition. This is consistent with previous chapters investigating atmospheric environments[9] and the effects of thin film water layer thickness on IG-SCC for this exact material lot, which indicated that for a 0.6 M NaCl solution the thickness at which cathodic limitation was observed was around 92 microns. Initial estimates for the misting condition water layer thickness were around 100 microns[9], but further testing has indicated that it is most likely closer to 150 microns. Alternatively, the increased da/dt_{II} crack growth rates could be due to the effects of increased oxygen diffusion through the misted thin film rather than a bulk solution, which would further alter the cathodic reaction kinetics observed and increase the available cathodic current for a given electrochemical potential. Studies have indicated that the critical film thickness in which increased oxygen diffusion occurs in thin films varies between 250 microns and 1 mm[22–26], therefore estimates for the misting film thickness are well below these estimates.

Now that the effects of both chloride concentration and geometry-induced cathodic limitation are independently determined, the magnitude that these factors affect each other can be derived. As solution chloride concentration increases, solution conductivity also increases, and this may in turn decrease the effects of cathodic limitation observed across the different atmospheric environments. Alternatively, the solution geometry-induced cathodic limitation could severely limit the maximum cathodic current available despite this increase to conductivity and stifle crack growth rates proportionately. Either of these effects could have a noticeable impact on crack tip chemistry development, which would strongly impact the K_{TH} values observed, or crack tip chemistry maintenance, which would strongly impact the da/dt_{II} crack growth rates. Should these factors have any influence over each other a diverging or converging of the lines representing the different environments should be apparent in Figures 4.2 or 4.3.

From Figure 4.2 we can see that for the K_{TH} values difference between the least limiting (Imm -800 mV_{SCE}) and most limiting (wicking) environments remained roughly the same across all chloride conditions. This strongly indicates that these factors are largely independent when determining the K_{TH} for this system. It is likely that across all the conditions and chloride concentrations present in this study an adequate amount of cathodic current could be supplied through the solution, regardless of solution chloride concentration. From Figure 4.3 we can see that the da/dt_{II} crack growth rates also maintained a roughly similar spread between the polarized and non-polarized environments across all chloride conditions.

4.5.3. Electrochemical observations and trends

Prior research from Chapter 3 into the electrochemical potential of Al-Mg alloys during IG-SCC testing have revealed a strong correlation between the IG-SCC crack growth kinetics and the bulk potential of the sample surface[9]. This correlation is best understood within the framework of a mixed-potential theory paradigm, in which anodic reactions occurring at the crack tip that fuel the IG-SCC mechanism are balanced by cathodic reactions occurring along the bulk surface. As IG-SCC crack growth rates increase or the crack tip extends (thus revealing unpassivated β and α phase), anodic demand needed to fuel dissociation at the β and α phase are subsequently increased and higher currents are required. In the absence of a governing potentiostat, which can act as an 'infinite' cathode, the balancing cathodic current must be supplied by cathodic reactions, such as the oxygen reduction reaction and hydrogen evolution reaction, along the bulk surface. Provided these cathodic reactions kinetics remains constant during a test's duration, increased cathodic currents can only be obtained by manipulation of the bulk surface potential. Therefore, there exists an inherent direct correlation between the IG-SCC crack growth kinetics, or more specifically the anodic demand at the crack tip, and the bulk surface potential. Additionally, this allows for insight into the amount of cathodic limitation experienced for each environment. In the presence of increasing amounts of cathodic limitation, which would further limit the maximum amount of cathodic current one could achieve from the bulk surface, we could expect larger changes in the bulk surface potential to compensate for the diminished current increases.

Trends observed in the electrochemical potential behavior during testing follow well with anticipated anodic demand at the crack tip and can be seen well in Figures 4.4a-c. Prior to reaching the K_{TH}, when the IG-SCC mechanism is activated, OCP behavior is seen to be relatively erratic and in line with normal OCP drift behaviors observed for the misting and Imm FOCP testing. Interestingly, for the wicking conditions this was not true and all tests showed a marked and sudden decrease in the electrochemical potential before steadily increasing. This can be seen clearly in Figure 4.4c. This indicates that upon commencement of an increasing load, anodic demand for the wicking condition was suddenly increased. As this occurs prior to the K_{TH}, and thus not IG-SCC related, this is most likely a result of incomplete solution penetration at the crack tip due to closure. Initiation of an increasing load will decrease crack closure and expose unpassivated alloy surface, which would therefore initially increase anodic demand. This trend is likely not apparent in the other conditions due to their greater solution volumes and access to the crack tip from the sides of the sample. Upon reaching the K_{TH} for all conditions, the electrochemical potential is then seen to decrease steadily during Stage I and Stage II cracking. More specifically, this decrease was seen to correspond very closely with the deviation of the K rate from linearity after the K_{TH}. This is expected as upon reaching the K_{TH} and deviation of the K rate the IG-SCC mechanism is activated and anodic demand steadily increases noticeably. Finally, a minimum in the OCP is achieved upon sample failure and sharp, negative spikes are observed during sudden ductile crack extensions that expose unpassivated material at the crack tip.

Using the framework and trends described above, electrochemical potential data listed in Table 4.3 reveals important insight into both the anodic demand and cathodic limitation observed across all the environments and concentrations tested. Firstly, it can be seen that for each individual environment that as solution chloride concentration increases there is a general decrease in the measured electrochemical potentials. This is consistent with expectations, as increases in the chloride concentration were seen to increase IG-SCC rates, and therefore anodic demand, for all environments. Secondly, it can be seen that for each chloride concentration the electrochemical potentials decreased as cathodic limitation due to geometric effects increased. This is again consistent with expectations, as increased amounts of cathodic limitation will decrease the cathodic current available and require larger changes in the bulk surface potential to supply similar currents. Furthermore, variations in these trends are seen to be roughly mirrored in the IG-SCC susceptibility data in Figures 4.2 and 4.3. For the 0.6 M NaCl concentration, electrochemical potentials at more negative potentials than expected are seen for the FOCP and wicking condition (and slightly for the misting towards the end of testing). These correspond well to the increased da/dt_{II} rates observed for these conditions in Figure 4.3. Conversely, higher electrochemical potentials in 1.2 M NaCl for the atmospheric environments correspond well with the higher K_{TH} values seen for these tests in Figure 4.2. Lastly for the 0.3 M misting condition, which exhibited a noticeably higher K_{TH} and lower da/dt_{II} than expected during IG-SCC testing, abnormally higher electrochemical potentials can be seen in Table 4.3.

4.5.4. Implications for IG-SCC characterization of Al-Mg alloys in atmospheric environments

While full immersion testing offers multiple procedural advantages in the IG-SCC characterization of Al-Mg alloys, cyclic wetting and drying cycles in humid atmospheric environments have been shown to represent the most aggressive corrosion environments experienced by metals[27–29]. During drying cycles, solution geometries are reduced and solution concentrations increased, with the opposite occurring for wetting cycles. Accelerated testing utilizing such wet/dry cycles are thus often used as the primary protocol in the determination of the corrosion susceptibility in atmospheric environments.

While wet/dry cycling offers the best estimates for corrosion susceptibility, little work has been accomplished on the IG-SCC susceptibility of Al-Mg alloys due to experimental complexity. This work therefore provides a basis for the anticipated behaviors of these alloys in wet/dry cycling by independently isolating the effects of various key factors. Results indicated that a reduction in solution volume will reduce IG-SCC susceptibility, and higher chloride concentrations will increase IG-SCC susceptibility. Additionally, the highest IG-SCC susceptibility was always achieved when the sample was polarized to an electrochemical potential approximate to the OCP in full immersion. Therefore, conservative values for the maximum IG-SCC susceptibility of Al-Mg alloys in a hypothetical wet/dry cycle testing protocol can be achieved by comparable full immersion, set electrochemical potential at the highest anticipated chloride concentration. Additional insight into the IG-SCC behaviors during transient wetting/drying cycles can also be gleamed based on the contributions of the individual effects.

4.6. Conclusions

The IG-SCC susceptibility of AA5083-H131 sensitized to 40 mg/cm^2 was investigated for multiple model atmospheric environments and chloride concentrations ranging from 0.3 M NaCl to 5.45 M NaCl. Tensile testing was performed with high-resolution crack growth monitored using the dcPD method. All subcritical crack growth data were analyzed using the elastic-plastic K_J. Use of an SSC probe allowed for in situ electrochemical potential measurements and insights. The following conclusions are established.

- For each atmospheric environment an increase in chloride concentration resulted in increased IG-SCC susceptibility (resulting in lower K_{TH} values and higher da/dt_{II} crack growth rates).
- IG-SCC susceptibility was found to decrease across each chloride concentration as cathodic limitation from solution geometry-induced effects increased.
- As chloride concentration increased, cathodic limitation was found to have a no discernable effect on the K_{TH} or da/dt_{II} crack growth rates observed between non-polarized and polarized environments.
- Electrochemical potential data supports the observation that anodic demand at the crack tip increases as chloride concentration increases and cathodic limitation increases as solution geometry decreases.
- Conservative estimates for atmospheric IG-SCC crack growth rates can be achieved by using full immersion testing at a set potential at the highest anticipated chloride concentration.

4.7. Acknowledgements

This research was financially supported by the Office of Naval Research with Dr. Airan Perez as the Scientific Officer. Professor R.G. Kelly has also provided valuable insight into the development of these atmospheric environments and interpretation of the results.

4.8. References

1. M.E. Mcmahon, P.J. Steiner, A.B. Lass, and J.T. Burns, *Corrosion* 73 (2017): pp. 347–361.
2. M.E. Mcmahon, P.J. Steiner, A.B. Lass, and J.T. Burns, *Corrosion* 73 (2017): pp. 713–723.
3. C.B. Crane, and R.P. Gangloff, *Corrosion* 72 (2016): pp. 221–241.
4. C.B. Crane, R.G. Kelly, and R.P. Gangloff, *Corrosion* 72 (2016): pp. 242–263.

5. J.L. Searles, P.I. Gouma, and R.G. Buchheit, *Metall. Mater. Trans. A Phys. Metall. Mater. Sci.* 32 (2001): pp. 2859–2867.
6. G.L. Pioszak, and R.P. Gangloff, *Metall. Mater. Trans. A Phys. Metall. Mater. Sci.* 48 (2017): pp. 4025–4045.
7. R.H. Jones, J.S. Vetrano, and J.F. Windisch, *Corrosion* 60 (2004): pp. 1144–1154.
8. R.H. Jones, D.R. Baer, M.J. Danielson, and J.S. Vetrano, *Metall. Mater. Trans. A* 32 (2001): pp. 1699–1711.
9. P. Steiner, and J. Burns, *Corrosion* 74 (2018): pp. 1117–1131.
10. C. Liu, J. Srinivasan, and R.G. Kelly, *J. Electrochem. Soc.* 164 (2017).
11. Z.Y. Chen, and R.G. Kelly, *J. Electrochem. Soc.* 157 (2010): p. C69.
12. M.E. McMahon, J.R. Scully, and J.T. Burns, *Jom* 69 (2017): pp. 1389–1397.
13. C.B. Crane, R.G. Kelly, and R.P. Gangloff, *Corrosion* 72 (2016): pp. 242–263.
14. M.L.C. Lim, R.G. Kelly, and J.R. Scully, *Corrosion* 72 (2016): pp. 198–220.
15. M.L.C. Lim, "Intergranular Corrosion Propagation in Sensitized Al-Mg Alloys," 2016.
16. E647-15e1. Standard Test Method for Measurement of Fatigue Crack Growth Rates. *ASTM B. Stand.* 1–49 (2016). doi:10.1520/E0647-15E01.2
17. T. Anderson, "Fracture Mechanics: Fundamentals and Applications," 3rd ed. (Boca Raton, FL: CRC Press, 2005).
18. V. Kumar, M.D. German, and C.F. Shih, "An Engineering Approach for Elastic-Plastic Fracture Analysis" (1981).
19. Z.D. Harris, E.M. Dubas, A.S. Popernack, B.P. Somerday, and J.T. Burns, *Theor. Appl. Fract. Mech.* (n.d.): p. in review.
20. P. Steiner, and J. Burns, *ICF 2017 - 14th Int. Conf. Fract.* 1 (2017): pp. 566–567.
21. R.P. Gangloff, H.M. Ha, J.T. Burns, and J.R. Scully, *Metall. Mater. Trans. A* 45 (2014): pp. 3814–3834.
22. M. Stratmann, *Corrosion Science* 30 (1990): pp. 697-714.
23. M. Stratmann, H. Streckel, K.T. Kim, and S. Crockett, 30 (1990): pp. 715–734.
24. G.S. Frankel, M. Stratmann, M. Rohwerder, A. Michalik, B. Maier, J. Dora, and M. Wicinski, *Corros. Sci.* 49 (2007): pp. 2021–2036.

25. M. Stratmann, *Corrosion Science* 30 (1990): pp. 681-696.
26. O. Dolgikh, A. –S Demeter, S. V. Lamaka, M. Taryba, A.C. Bastos, M.C. Quevedo, and J. Deconinck, *Electrochim. Acta* 203 (2016): pp. 379–387.
27. X. Zhao, and G.S. Frankel, *Corrosion* 62 (2006): pp. 956–966.
28. B. Maier, and G.S. Frankel, *Corrosion* 67 (2011): pp. 1–10.
29. N. Brown, P. Kramer, F. Friedersdorf, M. Schindelholz, and J. Siegel, *Corrosion* 72 (2016).

Chapter 5. Use of ZRP in atmospheric environments

5.1. Abstract

The viability of zinc-based metal-rich coatings in an atmospheric misting environment was examined for highly sensitized AA5456-H116 using fracture mechanics-based testing, high-fidelity monitoring of crack growth, and electrochemical potential measurements. The baseline IG-SCC behavior for a misting environment at various set electrochemical potentials (via sintered silver chloride) probes was first examined. Initial results showed that the effect of potential on the IG-SCC crack growth rates were diminished as compared to full-immersion conditions, suggesting a potentially less potent effect of cathodic polarization via galvanic coupling in atmospheric environments. This diminished mitigation was also seen in direct testing of a candidate zinc-rich primer in the same misting environment, with little change across multiple scribe lengths. The presence of cathodic protection is supported by observed electrochemical potential data, which indicates the primer established a cathodic potential for the majority of testing. *In toto*, these results demonstrate that zinc-rich primers remain a feasible mitigation technique for Al-Mg alloys in atmospheric environments.

5.2. Introduction

The IG-SCC behavior of Al-Mg alloys has been extensively correlated to the electrochemical potential in chloride containing environments[1–5]. This is suspected to be due to the proposed coupled anodic dissolution mechanism for IG-SCC in these alloys, which postulates that dissolution of the β and α phases at the crack tip followed by metal ion hydrolysis causes an aggressive acidified crack tip chemistry and enhanced H production at the crack tip[6–8]. H diffuses ahead of the crack tip into the fracture process zone, enabling hydrogen embrittlement and crack growth rates faster than possible from anodic dissolution alone[8]. This mechanism corresponds well with experimental trends of IG-SCC susceptibility that align with the pitting potentials of the β and α phases; specifically, high susceptibility at electrochemical potentials anodic to the pitting potentials for both phases, intermediate susceptibility for potentials between the β and α phase pitting potentials, and low susceptibility at potentials cathodic to both pitting potentials[9]. Therefore, a reasonable IG-SCC mitigation strategy is to lower the electrochemical potential to below one or both of these pitting potentials; this has been demonstrated for full immersion environments[9].

Practically, this cathodic polarization can be obtained in engineering applications by the use of a metal-rich coatings. These coatings, which have high weight concentrations of metal pigments embedded in resin or some other medium, seek to establish a galvanic coupling with the base alloy. Through this galvanic coupling intermediate cathodic potentials below the pitting potential of the β and α phases can be achieved and the IG-SCC mechanism retarded. In addition to the galvanic potential achieved, however, other factors such as the self-corrosion rates, passivation rate, porosity, and secondary barrier formation must also be considered to achieve maximum protection[10]. All of these factors have been found to impact the efficacy and ability of metal-rich primers to mitigate IG-SCC. Zinc-rich primers (ZRP) are being considered, these systems employ high pigment weight concentrations (PWC) of pure zinc to obtain protective potentials below the pitting potentials of both the β and α phase (-1.09 V_{SCE} in 0.6 M NaCl)[10]. While typically employed on steel substrates, these ZRP have been shown to mitigate IG-SCC on Al-Mg substrates due to their high PWC's and the formation of corrosion product (ZnO and $Zn(OH)_2$) secondary impedance barriers[10,11].

While testing of ZRP's on Al-Mg alloys has been performed in full immersion conditions[10], their effectiveness in atmospheric environments remains to be seen. It has been shown for Al-Mg alloys that atmospheric environments, typified by lower solution geometries and higher chloride concentrations, can have discernable effects on the IG-SCC susceptibility and bulk surface electrochemical potential[12]. While initial attempts to apply electrochemical potentials in these atmospheric conditions was largely successful, IG-SCC mitigation was slightly reduced due to ohmic drop through the thin solution geometries between the probe and the crack tip[12]. Similar ohmic drop concerns may therefore severely limit the distance over which a protective potential established by a ZRP can be achieved, also known as the "throwing power" of the primer[13], thus reducing the ZRP efficacy in these environments. Furthermore, should the solution morphology become more tortuous or individual discrete droplets form the throwing power can be further reduced. Conversely, solution chemistry changes may also have increased effect in atmospheric environments due to lower solution volumes. Metal ion concentrations, such as Zn^{2+}, have been shown to reduce IG-SCC in these alloys and could have increased potencies in these conditions[14]. Therefore, the efficacy of ZRP primers may be drastically altered in these atmospheric environments and might be an ineffective mitigation strategy for engineering applications.

5.2.1. Chapter objective

Testing by McMahon on AA5456-H116 sensitized to 65 mg/cm^2 has demonstrated the efficacy of ZRP primers on highly sensitized Al-Mg alloys in full immersion conditions[10]. It was found that intermediate to low porosity, high Zn PVC ZRP formulations established and conserved protective electrochemical potentials sufficient for cathodic protection and are recommended to achieve sufficient IG-SCC mitigation in aggressive marine environments. Critically, these experiments were conducted in full-immersion environments and do not address the effects of solution geometry. Therefore, the main objective of this paper is to extend ZRP evaluation to atmospheric environments in order to address their efficacy in these conditions. Specifically, any observed reductions in cathodic potential protection, throwing power, or IG-SCC mitigation. First, the effectiveness of cathodic potential protection via potentiostat in atmospheric environments will be performed to benchmark expected electrochemical potential behaviors at various cathodic potentials. The top performing ZRP from McMahon *et al.*, determined by desirable electrochemical and application properties, will then be tested and compared to full immersion conditions. Finally, the electrochemical data collected will be analyzed and correlated to crack growth behavior.

5.3. Experimental methods and material

5.3.1. Materials and sample preparation

In this study the Al-Mg alloy AA5456-H116 was investigated. The source, thickness, and composition of this alloy is reported in Table 2.1. The temper designation indicates that this alloy has been special strain hardened to a corrosion resistant temper[15]. The Ramberg-Osgood parameters and results of a grain size analysis are reported in Table 2.2. Prior LEFM based testing in chloride containing solutions of this exact production lot of material demonstrated a high susceptibility to IG-SCC at a NAMLT value of 65 mg/cm^2 in 0.6 M NaCl[9]. Additional microstructure and sensitization analysis on this alloy are detailed elsewhere[1].

Single edge notch tensile (SENT) specimens of the AA5456-H116 alloy were machined with an S-L orientation (loading applied in S direction, crack growth in L direction) and polished to 400 grit finish. The samples have a gauge width of 17.33 mm and thickness of 6.62 mm. A 4.83 mm deep electrically discharged machined (EDM) notch was placed at the mid-point of the gauge section which aligned with the center (T/2) location in the S-direction of the plate. Samples were then sensitized at 100°C for 336 hours to achieve the desired NAMLT value of 65 mg/cm^2 based on previously established sensitization curves for these material lots derived from ASTM G67 testing[16].

Following sensitization samples were cleaned *via* sonication in acetone and methanol for 15 minutes each. Uncoated samples were then masked using vinyl tape and a rubber butyl stop-off lacquer, leaving exposed alloy 7.5 mm above and below the Mode I crack path (1.5 cm total height) unless otherwise noted. Coated samples were cold sprayed with an organic epoxy ZRP (OZRP) from Sherwin Williams with a 90% Zn PWC. Additional physical, electrochemical, and sourcing details are detailed for this OZRP by McMahon *et al*[10]. All cold spraying was performed by Luna Innovations, Inc. using thoroughly agitated, mixed formulations and a spraying distance of 200 to 300 mm with 50% overlap. For the coated samples scribe lengths with heights of 0.3, 5, and 10 mm centered on the Mode I crack plane were left exposed and uncoated in order to ascertain the throwing power of the ZRP coating.

5.3.2. Mechanical testing

All fracture tests were conducted using software-controlled, servo-hydraulic frames with active crack length feedback via the direct current potential difference (dcPD) method[17]. Potential readings were taken via copper wires (0.127 mm diameter) coated in PFA (perfluoroalkoxyalkane) spot welded 0.5±0.1 mm from the center of the EDM notch with a constant 6 A or 1 A current passing through the sample during precracking and constant displacement testing, respectively. These potential readings were then taken every 30 seconds in a process reported by McMahon et al.[1,18] and converted to an instantaneous crack length using the Johnson's equation, resulting in crack growth resolution of roughly 0.5 µm[1].

Samples were loaded by means of freely rotating clevis grips, in compliance with stress intensity (K) boundary conditions[19]. They were fatigue precracked to a cumulative notch plus crack length of 5.3 mm via a decreasing K protocol from a K_{max} of 6 MPa√m to a K_{max} of 3.5 MPa√m at a stress ratio ($R = K_{min}/K_{max}$) of 0.1 and a frequency of 3 Hz. At this point a 1 kN load was applied to the precracked specimens (corresponding to a K_{max} of roughly 2 MPa√m) and the testing environment was introduced; these conditions were held for 1 hr to stabilize the initial crack tip and bulk surface chemistry. Following this 1 hr hold samples were tested via slow-rising displacement at a rate corresponding to an initial dK/dt of roughly 0.25 MPa√m/hr. Tests were run until failure or the samples exhibited bulk scale plasticity.

Following test completion, linear post-processing crack length corrections were applied based on fracture surface analysis of the initial and final crack lengths. Crack growth rates were calculated from the tangent of a second order polynomial fit to 7 crack length vs time data points (akin to the protocol established for fatigue crack growth rates in ASTM E647[20]). Elastic-plastic stress intensity (K_J) analysis was also conducted using the 0.2% offset yield strength and Ramberg-Osgood constants for the alloys, derived via compressive testing and reported in Table 2.2, in compliance with previous literature[8,21,22]. A functional resolution limit due to localized (crack tip) plasticity introducing 'false' dcPD-measured crack extension was previously established for this production lot of AA5083-H131 lot and has a functional form of:[8,23]

$$\frac{da}{dt}_{False} = 5 \times 10^{-7} \cdot \exp(0.0577K) \qquad \text{(Eq. 5.1)}$$

Recent fracture mechanics experiments conducted in an inert environment (dry N_2 gas with RH < 5%) on a Ni-based superalloy using a fixed dK/dt testing protocol demonstrate that the dcPD-measured resolution limit scales linearly with dK/dt[24]. A correction protocol was then developed to subtract this 'false' da/dt contribution from measured da/dt, thereby enabling the 'true' da/dt to be determined for an experiment conducted under fixed dK/dt conditions[24]. Given that the current study utilizes testing at a fixed *displacement* rate, it is expected that dK/dt will begin to increase from the initial value of 0.25 MPa√m/hr once crack growth occurs. As such, it is incorrect to simply subtract Eq. 5.1 from measured da/dt vs. K relationships as was done in prior work[1,18,24,25] since Eq. 5.1 is only rigorously valid for dK/dt = 0.3 MPa√m/hr and therefore must be modified to incorporate an explicit dK/dt dependence. Given that the mechanistic basis for the scaling in the resolution limit is based solely on fracture mechanics principles[24,26] and is therefore nominally material-agnostic, a dK/dt dependence can be introduced into Eq. 5.1 *via* dividing the prefactor (5×10^{-7}) in Eq. 5.1 by the dK/dt for the experiment to which Eq. 5.1 was fit (0.3 MPa√m/hr)[8], yielding:

$$\frac{da}{dt}_{False} = 1.667 \times 10^{-6} \left(\frac{dK}{dt}\right) \cdot \exp(0.0577K) \qquad \text{(Eq. 5.2)}$$

In the current study, dK/dt was determined by numerically differentiating a smoothing spline fitted to the experimental K vs. time data using the Matlab curve fitting toolbox. A smoothing parameter (p) of 0.9 was utilized for fitting each individual experiment. The smoothing spline was selected for fitting the K vs. time profile due to an improved fit (quantified *via* R^2) over the entire time range relative to a power law or exponential function. Once the dK/dt vs. K relationship is known Eq. 5.2 can be utilized to calculate a test-specific resolution limit that accounts for the expected increase in dK/dt as cracking progresses. This 'false' da/dt can then be subtracted from the experimentally-measured da/dt to correct for effects of localized plasticity on the dcPD system[24].

5.3.3. Environmental setup

The misting protocol was designed to be representative of a constant salt-spray environment and was thus loosely based on ASTM B117[27]. To this end, a Plexiglass cell with a large radius and a sloped ceiling and floor was designed to promote air circulation and drainage of coalesced water away from the sample. Two 80° conical fine mist spray nozzles with an inner diameter of 0.35 mm were positioned at the cell perimeter on either side of the crack path and would continuously spray the sample from a 2 L reservoir of aerated 0.6 M NaCl solution at room temperature at a rate of roughly 40 mL/min. Drainage from the cell was collected and circulated back into the reservoir. Further information on development and validation of these atmospheric environments can be found in a previous paper[25].

5.3.4. Electrochemical monitoring

During LEFM testing the electrochemical potential was monitored or applied via a 4-mm diameter sintered silver/silver-chloride (SSC) probe which acted as both a counter and reference electrode. Details of the governing electrochemical concepts, functional details/limitations of the probe application, and verification of the probe accuracy for thin film electrochemical measurements were demonstrated by Khullar, et al[28]. Notably, the probes were found to not impact the electrolyte composition, function well with currents up to 1 mA, and allow for accurate calculation of the ideal solution theoretical potential of these probes versus the standard hydrogen electrode (SHE) via the Nernst equation as long as the solution chloride concentration is known. As such, all the recorded electrochemical potentials collected via SSC probes will be translated with reference to an SCE reference electrode in this study to allow for direct comparison between all environments. During polarization testing the probe was placed at the bottom of the exposed window on the side opposite the EDM notch (approximately 12 mm diagonally away from the notch tip for a 15 mm window). The probe was attached to the sample via 100-µm thick double-sided adhesive to slightly offset it from the sample surface. During ZRP coating testing the probe was placed along the Mode I crack path, above the base alloy, opposite the notch in a similar fashion for all scribe widths (approximately 8 mm horizontally away from the notch tip). Implementation and investigation on the accuracy of these probes in these atmospheric environments have been discussed further in a previous paper[25].

5.4. Results

5.4.1. Impact of cathodic polarization on IG-SCC kinetics in misting environments

Use of the dcPD method and slow rising displacement loading protocol described above allows for detailed analysis relating the crack growth rate, da/dt, versus the stress intensity, K_J. From these data the various stages of SCC crack growth can be determined and the IG-SCC dependent parameters derived. Traditionally the two parameters of interest are the K_{TH} and the Stage II crack growth rate (da/dt_{II}). The K_{TH} is defined as the beginning of IG-SCC dominated fracture and is functionally defined as a significant increase in the slope of the da/dt vs. K_J relationship that occurs above the resolution limit. The da/dt_{II} is defined as the crack growth rate which it is largely independent of increasing stress intensity; this has been postulated to be due to an H-diffusion limitation from the crack tip surface into the crack tip process zone[2,4]. This limitation causes a plateau in the da/dt vs K_J graph leading up to the K_{IC}, at which point sub-critical HEAC based cracking is augmented by a ductile failure mechanism (possibly some stable ductile tearing then final rupture). It is worth noting that scatter has been observed in the da/dt vs. K_J relationship for samples from the same lot run under the same conditions, thus current data should be analyzed in the context of this inherent variability[2].

Crack growth vs stress intensity data for AA5456-H116 sensitized to NAMLT 65 mg/cm^2 and tested at various electrochemical potentials ranging from -800 to -1200 mV_{SCE} are reported in Figure 5.1. Data from McMahon for comparable full immersion testing of the same material lot polarized to -800 and -900 mV_{SCE} are included as reference lines (tests run at -1000 mV_{SCE} and below are not included as they show no crack growth above the stated resolution limit)[9]. Values for the K_{TH} of set electrochemical potential tests ranged from roughly 8 to 12 MPa√m for most tests, barring one -800 mV_{SCE} and one -900 mV_{SCE} test. For the -800 mV_{SCE} testing in misting one duplicate showed a noticeably higher K_{TH} than its corresponding full immersion test, which exhibited a K_{TH} value of roughly 6 MPa√m, while the other duplicate showed close correlation with the full immersion test. Conversely, both duplicates for -900 mV_{SCE} testing in misting exhibited a noticeably lower K_{TH} value than their corresponding full immersion test, which exhibited a K_{TH} value of roughly 15 MPa√m. This is likewise true but cannot be visually shown for the other more cathodic potentials, whose counterpart full immersion tests resulted in no discernable crack growth above the resolution limit during the entirety of testing[9]. Values for the da/dt_{II}, which range from roughly 4.1 * 10^{-5} mm/s to 4.1 * 10^{-4} mm/s, showed a slight trend with applied electrochemical with the -800 mV_{SCE} and -900 mV_{SCE} tests showing higher da/dt_{II} values than the more cathodic -1000 to -1200 mV$_{SCE}$ potentials. This demarcation correlates well with the expected pitting potential of the β phase, which is roughly estimated to be -950 mV$_{SCE}$ for 0.6 M NaCl solution[10].

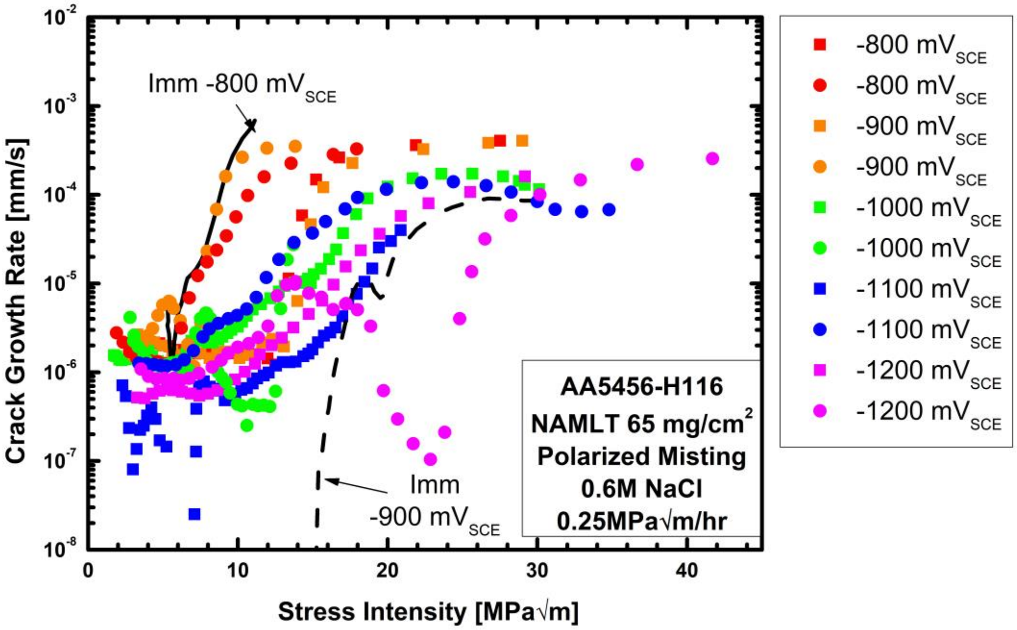

Figure 5.1. Crack growth rate vs. stress intensity for testing of AA5456-H116 at a NAMLT value of 65 mg/cm^2 at various electrochemical potentials in a misting environment. Reference lines for full immersion testing are taken from McMahon[10].

In summary, three overarching trends are apparent. First, K_{TH} values were found to be largely independent of applied electrochemical potential, although one -800 and one -900 mV$_{SCE}$ duplicate resulted in a noticeably lower K_{TH} value consistent with -800 mV$_{SCE}$ full immersion testing. Secondly, da/dt$_{II}$ generally decreased with increasing levels of cathodic polarization. Lastly, cathodic polarization in misting environments exhibited a lower level of mitigation of IG-SCC as compared to full immersion testing.

5.4.2. Efficacy of ZRP in misting environments

Crack growth vs stress intensity data for AA5456-H116 sensitized to NAMLT 65 mg/cm^2 and tested with various scribe widths of ZRP are reported in Figure 5.2. Values for the K_{TH} of the ZRP coated samples ranged from roughly 8 to 10 MPa√m, all of which are discernably higher than that observed for the OCP condition. Values for the da/dt$_{II}$, which range from roughly 8x10^{-5}

mm/s to 2.3x10^{-4} mm/s, are also noticeably lower than that observed for the OCP condition. All ZRP tests correspond well with the electrochemically polarized -1000 mV$_{SCE}$ test. This is consistent with prior work by McMahon wherein IG-SCC susceptibility of ZRP coated specimens was found to be directly correlated with the bulk surface. electrochemical potential[10].

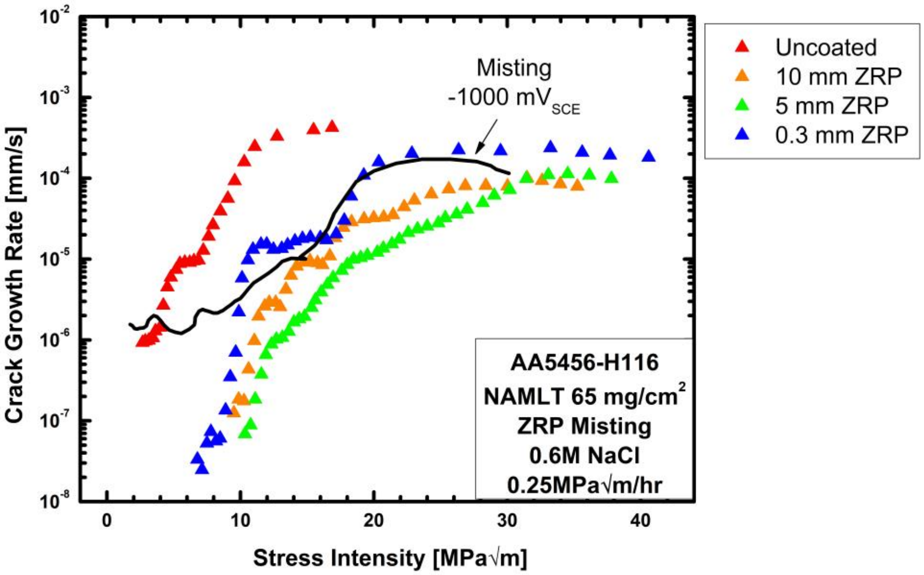

Figure 5.2. Crack growth rate vs. stress intensity for testing of AA5456-H116 at a NAMLT value of 65 mg/cm^2 for various ZRP scribe widths in a misting environment. Reference line is AA5456-H116 at a NAMLT value of 65 mg/cm^2 set to -1000 mV$_{SCE}$ in a misting environment.

In summary, three significant trends are apparent. First, testing of the ZRP in misting environments always resulted in lower IG-SCC susceptibilities as compared to testing of an uncoated sample. Second, scribe width of the ZRP resulted in little to no apparent change in IG-SCC susceptibility in misting environments. Finally, testing of the ZRP in misting environments corresponded well with electrochemically polarized misting testing, barring a noticeable decrease in stress-assisted IGC rates prior to Stage II cracking.

5.4.3. Electrochemical potential observations

The electrochemical potential was monitored during testing in an attempt to gauge how effectively the ZRP coatings were able to apply, and sustain, a protective potential. Examples of measured potential plots are shown in Figure 5.3 for AA5456-H116 sensitized to 65 mg/cm^2 and no ZRP coating and Figure 5.4 for AA5456-H116 sensitized to 65 mg/cm^2 with a 10 mm scribe ZRP coating (Figure 5.4a), a 5 mm scribe ZRP coating (Figure 5.4b), and a 0.3 mm scribe ZRP coating (Figure 5.4c). During polarization testing the probe was placed at the bottom of the exposed window on the side opposite the EDM notch (approximately 12 mm diagonally away from the notch tip for a 15 mm window) and during ZRP coating testing the probe was placed along the Mode I crack path opposite the notch in a similar fashion for all scribe widths (approximately 8 mm horizontally away from the notch tip). For the uncoated specimen common trends correlating to the different crack growth regimes were roughly observed, as seen and reported in previous studies on this material lot[12]. These trends are: (1) a slight or negligible drift in the OCP prior to the K_{TH}; (2) a more significant and constant decline in OCP during Stage I and Stage II crack growth; and (3) reaching of a minimum OCP close to sample failure with sharp negative spikes in the OCP during sudden ductile failure events. For ZRP coated specimens, however, this trend was not observed. For these samples the electrochemical profile reveals that lower electrochemical potentials of roughly -980 mV_{SCE} were established during the beginning of testing, which then rose up to a maximum of -900 mV_{SCE} over the course of 24 hours. These potentials were then maintained until testing terminated.

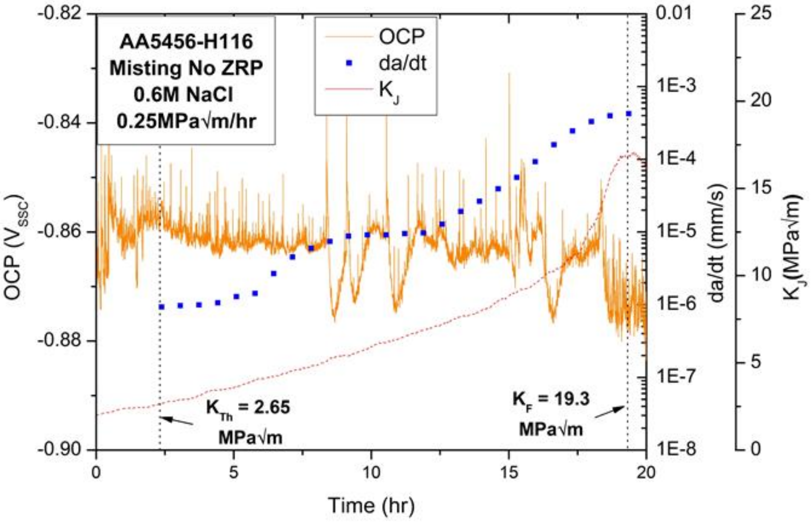

Figure 5.3. OCP (V_{SCE}), da/dt (mm/s), and K_J (MPa√m) vs time (hr) data for AA5456-H116 NAMLT 65 mg/cm^2 in a misting environment with no ZRP primer.

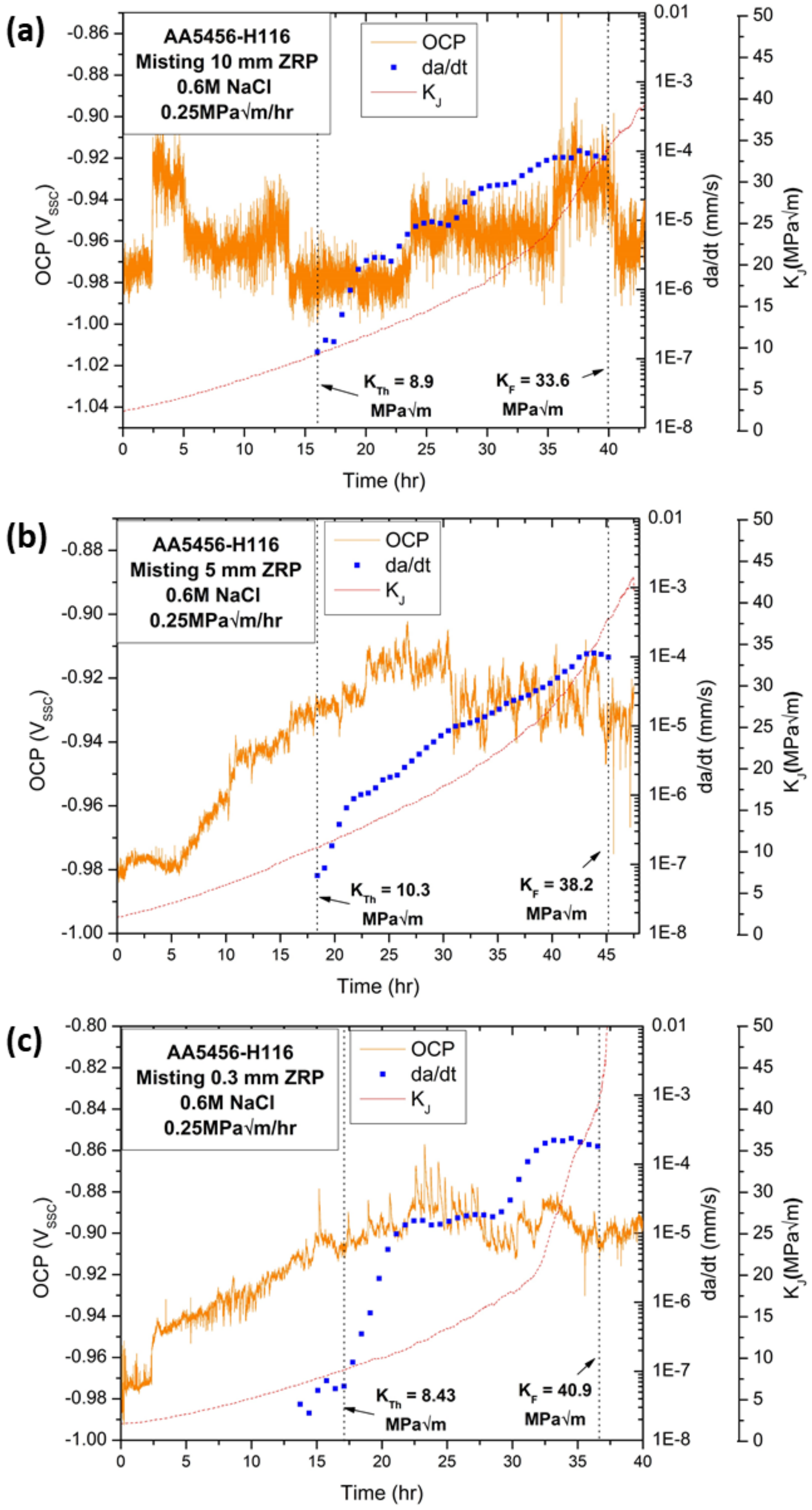

Figure 5.4. OCP (V_{SCE}), da/dt (mm/s), and K_J (MPa√m) vs time (hr) data for (a) AA5456-H116 NAMLT 65 mg/cm^2 in a misting environment with a 10 mm ZRP scribe, (b) AA5456-H116 NAMLT 65 mg/cm^2 in a misting environment with a 5 mm ZRP scribe, and (c) AA5456-H116 NAMLT 65 mg/cm^2 in a misting environment with a 0.3 mm ZRP scribe.

5.5. Discussion

This discussion will be divided into three parts. First, the baseline testing wherein electrochemical potentials were applied in misting environments, shown in Figure 5.1, will be discussed and analyzed. It can be seen that a discrepancy between full immersion and misting testing exists across the same nominal electrochemical potential, which could indicate complications in galvanic protection for these environments. Next, testing of ZRP coatings with various scribe lengths will be discussed and compared to the baseline testing results. Ultimately, the viability of these coatings will be determined for use in atmospheric environments and compared to full immersion testing results. Lastly, electrochemical trends observed during testing will be analyzed and correlated to trends in the IG-SCC susceptibility and/or crack growth rates.

5.5.1. Baseline testing of electrochemical polarization efficacy in misting environments

IG-SCC susceptibility is strongly dependent on the applied potential in full immersion environments[1–5]. Traditionally, however, these electrochemical potentials are applied in full immersion environments wherein ohmic drop through the solution would have a lower impact. Smaller solution volumes have been conclusively shown to provide significant levels of ohmic resistance that may complicate this protection mechanism[12]. Due to this ohmic resistance through the solution, applied potentials *via* potentiostat (or ZRP) may be diminished. Thus, benchmarking of the electrochemical behavior for various electrochemical potentials must first be conducted to determine the maximum expected efficacy one could achieve through electrochemical polarization in these environments.

From Figure 5.1 it can be seen that despite the wide range of applied potentials, little change in IG-SCC susceptibility is observed. When more cathodic electrochemical potentials are applied to an Al-Mg alloy, one would expect higher K_{TH} values and lower da/dt_{II} crack growth rates as the IG-SCC mechanism is throttled. In regards to the K_{TH}, this trend is not largely seen and as more negative potentials were applied the K_{TH} tended to remain the same. The two exceptions to this trend are the -800 mV_{SCE} and -900 mV_{SCE} duplicates that showed noticeably lower K_{TH} than the other tests. These potentials correlate well with the expected demarcation of IG-SCC susceptibilities established by the breakdown potentials of the various phases. At potentials below the breakdown potential of the β phase (-950 mV_{SCE} for 0.6 M NaCl solution[10]) the dissolution of the β phase at the crack tip is drastically decreased and hydrogen production leading to embrittlement reduced. This is further supported by the trends observed in the da/dt_{II} rates, which show a similar grouping of tests with potentials below 950 mV_{SCE} exhibiting lower da/dt_{II} rates. This baseline testing therefore indicates that cathodic protection can still be a viable mitigation technique in misting environments.

Comparison of the electrochemically controlled misting environments to their full immersion counterparts reveal a drastic decrease in the electrochemical-dependent IG-SCC behavior, however. While testing at -800 mV_{SCE} was found to be roughly comparable between both environments, testing at more negative potentials showed noticeable deviations. Testing at -900 mV_{SCE}, which shows a significantly higher K_{TH} and lower da/dt^{II} in full immersion conditions, shows no significant difference from -800 mV_{SCE} testing in misting conditions. For tests run at electrochemical potentials -1000 mV_{SCE} and below in misting this disparity is even more strikingly apparent, as their comparable full immersion tests showed no IG-SCC cracking at all above the resolution limit[9]. It can therefore be seen that the level of cathodic polarization mitigation is decreased in misting environments as compared to full immersion environments.

This discrepancy could be due to ohmic drop through the solution, ultimately deriving from the placement of the SSC probe that applies the protective current. Unlike full immersion testing, wherein a platinum mesh typically surrounds the sample and provides uniform current distribution through the solution, application of a potential through the SSC probe is highly localized. This placement (12 mm away from the crack tip in this study) is subjected to additional ohmic resistance through the thin solution film and will decrease the range at which the protective current can be applied, similar to the throwing power of ZRP coatings. Thus, while a nominally cathodic potential is applied, change in the electrochemical potential of the bulk surface around the crack tip may be lessened or unaffected altogether. This can be visually seen by the apparent centralization of the testing in Figure 5.1 around where one would expect a full immersion test run at OCP to be (roughly -860 mV_{SCE} as seen in Figure 5.3). This therefore suggests that the efficacy of cathodic protection in misting environments, while still viable, will have a drastically reduced effect and could be highly dependent on the placement of the probe and/or coating. Alternatively, this discrepancy could be due to increased oxygen diffusion rates on the sample surface. Thinner solution geometries would allow for increased oxygen diffusion rates through the solution, as seen and discussed in Chapter 3. These increased oxygen concentrations would allow for greater cathodic currents, ultimately allowing for higher amounts of dissolution at the crack tip.

5.5.2. Performance of ZRP coatings in misting environments

Trends observed in Figure 5.2 for ZRP coating performance correspond well with previously observed trends established in the benchmark applied electrochemical potential misting testing. It can be seen that when compared to an uncoated sample all ZRP testing exhibit lower IG-SCC susceptibilities, this suggests that the ZRP is applying a protective potential. Electrochemical profiles in Figures 5.4a-c indicate this potential is roughly in the range of 960 to 900 mV_{SCE}. From Figure 5.2 we can see that comparison of these tests to a -1000 mV_{SCE} polarized misting test shows greater similarity in IG-SCC parameters as compared to full immersion testing at -1000 mV_{SCE}. This therefore suggests that the ZRP coatings are able to successfully polarize the sample in a misting condition, but mitigation is still limited by the same factors that affected polarization via the SSC probe.

Under the assumption that ohmic drop is increased in atmospheric environments due to thin film geometries, it is reasonable to assume that the scribe width, or how far the ZRP coating is separated from the crack path, might therefore be an area of concern. As scribe width increases the distance that a current must be applied through the thin film also increases. Should a large enough scribe be used, the ZRP may be unable to apply a sufficient protective potential through the thin film to the crack tip. From Figure 5.2 we can see that this is not the case, and for all scribe lengths the ZRP was able to reduce IG-SCC susceptibility. This is further corroborated by electrochemical data in Figures 5.4a-c, which show similar protective potentials were applied along the Mode I crack plane for all scribe widths. This therefore appears to indicate that for these misting environments, ohmic drop through the solution is not the source of the decreased IG-SCC susceptibilities as even when the distance between the crack tip and coating was nearly eliminated (0.15 mm for the 0.3 mm scribe length) similar results were achieved to the polarized misting testing. These increased susceptibilities are consequently likely due to increased oxygen diffusion rates, which would still be present in these ZRP tests.

5.5.3. Electrochemical observations and trends

In order for metal-rich coatings to achieve successful protection during IG-SCC testing it must 1) achieve potentials cathodic to the OCP, 2) exhibit a high polarizability in order to respond to perturbations in the anodic demand due to exposure of new surfaces and 3) sustain those potentials are adequately maintained over long periods of time. While cathodic potentials may be easily obtained at the start of testing due to the metal pigment used, the ability of the ZRP to provide adequate polarizability and cathodic protection can depend greatly on many parameters[10]. A reduction in metal-rich primer efficacy is typically observed as metal pigments are depleted in the coating, therefore certain coatings may be unsuitable for sustained IG-SCC mitigation. From Figures 5.4a-c it can be seen that for the ZRP primer used in this study, a cathodic potential was in fact achieved at the start of testing for all scribe widths. While an OCP of roughly -860 mV_{SCE} was recorded for this highly sensitized Al-Mg alloy in 0.6 M NaCl, tests including a ZRP achieved electrochemical potentials of roughly -980 mV_{SCE} upon testing initiation. Good agreement between these tests and the set electrochemical potential test performed at -1000 mV_{SCE} support the link between IG-SCC behavior and bulk electrochemical potential, as was also demonstrated by McMahon[10]. It should be noted that as testing progressed, however, electrochemical potentials were seen to rise and achieve values closer to -930 mV_{SCE} and as high as -900 mV_{SCE} within 24 hours. This increase in potential during testing may indicate a decrease in the ZRP sustainability as IG-SCC crack growth rates increased, and merits further investigation.

One interesting observation worth noting is the disappearance of the trend between bulk surface potential and expected anodic demand when a ZRP coating was present. This trend, which can be seen in Figure 5.3, has been observed previously for this material lot in testing run at OCP[12]. This trend originates from the lack of an external cathode current source, as such the bulk surface potential must decrease in order to provide cathodic current to the anodic crack tip. Therefore, it is readily apparent why such trend is not seen for ZRP coated samples. Firstly, as previously discussed the ZRP coatings were able to successfully mitigate IG-SCC susceptibility, thus lower magnitudes of anodic demand should be needed. Secondly, given adequate ZRP polarizability the galvanic coupling between the ZRP and the sample surface should be relatively constant, ultimately mitigating these trends. This is consistent with the high polarizability of this ZRP demonstrated by McMahon[10].

5.6. Conclusions

The IG-SCC susceptibility of the alloy AA5456-H116 sensitized at 100°C to a NAMLT value of 65 mg/cm^2 was assessed at various electrochemical potentials established *via* SSC probe or a ZRP in a misting environment. Tensile testing was performed with high-resolution crack growth monitored using the dcPD method in 0.6 M NaCl electrolyte solutions. All subcritical crack growth data were analyzed using the elastic-plastic K_J. Use of an SSC probe allowed for in situ electrochemical potential measurements and insights. The following conclusions are established.

- Polarization of misting tests *via* SSC electrode resulted in diminished electrochemical potential-dependent IG-SCC susceptibility trends as compared to full immersion testing.
- Testing of a candidate ZRP in a misting environment resulted in a reduction of the IG-SCC susceptibility similar to that seen in polarized misting conditions.
- Increasing the scribe width of the tested ZRP up to 10 mm resulted in no discernable change in the IG-SCC susceptibility in misting environments.
- Electrochemical measurements obtained during ZRP testing indicate a protective potential was largely able to be applied during the entirety of testing. Typical electrochemical behavior collected during OCP testing, wherein the bulk surface acts as the cathode and decreases in potential as anodic demand increases, was not observed when a ZRP was present.

5.7. Acknowledgements

This research was financially supported by the Office of Naval Research with Dr. Airan Perez as the Scientific Officer.

5.8. References

1. M.E. Mcmahon, P.J. Steiner, A.B. Lass, and J.T. Burns, *Corrosion* 73 (2017): pp. 347–361.
2. C.B. Crane, R.G. Kelly, and R.P. Gangloff, *Corrosion* 72 (2016): pp. 242–263.
3. J.L. Searles, P.I. Gouma, and R.G. Buchheit, *Metall. Mater. Trans. A Phys. Metall. Mater. Sci.* 32 (2001): pp. 2859–2867.
4. R.H. Jones, D.R. Baer, M.J. Danielson, and J.S. Vetrano, *Metall. Mater. Trans. A* 32 (2001):

pp. 1699–1711.

5. S.K. Lee, P. Lv, and D.D. Macdonald, *J. Solid State Electrochem.* 17 (2013): pp. 2319–2332.
6. D.R. Baer, C.F. Windisch, M.H. Engelhard, M.J. Danielson, R.H. Jones, and J.S. Vetrano, *J. Vac. Sci. Technol. A Vacuum, Surfaces, Film.* 18 (2000): pp. 131–136.
7. R.H. Jones, J.S. Vetrano, and J.F. Windisch, *Corrosion* 60 (2004): pp. 1144–1154.
8. C.B. Crane, and R.P. Gangloff, *Corrosion* 72 (2016): pp. 221–241.
9. M.E. McMahon, J.R. Scully, and J.T. Burns, *Jom* 69 (2017): pp. 1389–1397.
10. M.E. McMahon, "Evaluation of Metal-Rich Primers for the Mitigation of Intergranular Stress Corrosion Cracking in Highly Sensitized Al-Mg Alloy AA5456-H116," University of Virginia, 2019.
11. R.N. Jagtap, P.P. Patil, and S.Z. Hassan, *Prog. Org. Coatings* 63 (2008): pp. 389–394.
12. P. Steiner, and J. Burns, *Corrosion* 74 (2018): pp. 1117–1131.
13. D. Kobayashi, M. Miyabe, Y. Kagiya, Y. Nagumo, R. Sugiura, T. Matsuzaki, and A.T. Yokobori, *Mater. Sci. Technol. (United Kingdom)* 30 (2014): pp. 24–31.
14. M.E. Mcmahon, J.T. Burns, and J.R. Scully, *Corros. Eng. Sci. Technol.* 55 (2020): pp. 331–340.
15. M.L.C. Lim, R.G. Kelly, and J.R. Scully, *Corrosion* 72 (2016): pp. 198–220.
16. M.L.C. Lim, "Intergranular Corrosion Propagation in Sensitized Al-Mg Alloys," 2016.
17. R.P. Gangloff, D.C. Slavik, R.S. Piascik, and R.H. Van Stone, *Small Crack Test Methods* (1992): pp. 116–168.
18. M.E. Mcmahon, P.J. Steiner, A.B. Lass, and J.T. Burns, *Corrosion* 73 (2017): pp. 713–723.
19. H. Tada, P. Paris, and G. Irwin, "The Stress Analysis of Cracks Handbook" (St. Louis, MO: Paris Productions Incorporated, 1985).
20. E647-15e1. Standard Test Method for Measurement of Fatigue Crack Growth Rates. *ASTM B. Stand.* 1–49 (2016). doi:10.1520/E0647-15E01.2
21. T. Anderson, "Fracture Mechanics: Fundamentals and Applications," 3rd ed. (Boca Raton, FL: CRC Press, 2005).
22. V. Kumar, M.D. German, and C.F. Shih, "An Engineering Approach for Elastic-Plastic Fracture Analysis" (1981).

23. C.B. Crane, R.G. Kelly, and R.P. Gangloff, *Corrosion* 72 (2016): pp. 242–263.

24. Z.D. Harris, E.M. Dubas, A.S. Popernack, B.P. Somerday, and J.T. Burns, *Theor. Appl. Fract. Mech.* (n.d.): p. in review.

25. P. Steiner, and J. Burns, *ICF 2017 - 14th Int. Conf. Fract.* 1 (2017): pp. 566–567.

26. R.P. Gangloff, H.M. Ha, J.T. Burns, and J.R. Scully, *Metall. Mater. Trans. A* 45 (2014): pp. 3814–3834.

27. ASTM International, *Water* 03 (2003): pp. 1–15.

28. P. Khullar, J. V. Badilla, and R.G. Kelly, *ECS Electrochem. Lett.* 4 (2015): pp. C31–C33.

Chapter 6. Effect of dcPD current implementation

6.1. Abstract

The impact of dcPD current on the electrochemical parameters of a system were investigated for model SCC testing environments and alloys. Several procedural and environmental factors were studied, including dcPD current wire attachment method, testing solution conductivity, corrosion damage at the lead interface, and current polarity. Ultimately it was found that for systems where the dcPD current application wires are exposed in electrolytic solutions, electrochemical potential and/or applied electrochemical current could be altered. Critically, strong metallurgical bonds between the dcPD current wires and sample plus the reduction of corrosion damage resulted in the smallest electrochemical impacts. Testing with dcPD current profiles similar to those used in SCC testing demonstrates that substantial changes in the electrochemical potential may occur under certain conditions, but is otherwise limited.

6.2. Introduction

The use of electrical potential difference (EPD) procedures to monitor crack growth have seen increasing and widespread acceptance in fracture research due to their high accuracy and efficiency[1,2]. These techniques rely on the principle that an electrical field in a cracked specimen with a current flowing through it is directly correlated to the exact sample geometry, most notably the crack size and length[1,2]. For a given constant current flow, voltage drop across the crack plane will increase for longer cracks due to a larger resistance and associated perturbation of the current streamlines. This change in potential can then be related directly to a change in crack size through analytical or empirical calibration techniques[3]. These EPD techniques are therefore applicable across a wide variety of testing environments and materials in which a current can be applied through the specimen, and can allow for *in-situ* crack growth monitoring and analysis[4].

Traditionally, two types of EPP techniques are employed: direct current potential drop (dcPD) and alternating current potential drop (acPD) differentiated primarily by their nominal current application method. The dcPD method is the traditional method to be employed, and typically uses direct currents of up to 50 amperes to create a two-dimensional electrical field which is constant through the sample thickness[4]. This method is prone to errors from thermoelectric effects and can cause sample heating when high currents are employed[2,4]. These effects were minimized with the creation of the acPD method, which typically uses a constant amplitude sinusoidal current. While thermoelectric effects are minimized with this technique, high frequencies were found to result in non-uniform current distributions along the sample surface in a phenomenon termed the "skin effect[4]." This ultimately led to the modification of the dcPD current method, upon the advancement of digital electronic capabilities, to employ pulsed and reversing currents in an effort to minimize thermoelectric effects while also avoiding the errors potentially induced from acPD testing.

The use of dcPD crack growth monitoring in fracture testing has been extensively studied, and many factors that may have an influence on the measured crack growth have been identified. Such examples include oxidization along the crack path, thermal effects, sample geometry, and plastic zone induced-effects[2,4,5]. However, it is generally assumed that dcPD current applied across the sample is contained fully within the sample thus does not impact the electrochemical conditions at the surface. This is presumed to be due to the high metal conductivity as compared to even highly conductive electrolyte solutions[6,7]. Many testing configurations allow for the application of the dcPD current outside of the testing solution, prior work by Gangloff et al. demonstrated that these conditions conform to the assumptions above[6]. However some testing configurations require application of the dcPD current wires directly onto the sample surface in solution without a coating[8–10]. This interface between the dcPD current wires and sample surface could result in "bleeding" current into the surrounding electrolyte. Furthermore, a loss of electrical contact between the dcPD current wires and sample could lead to the formation of an electrical capacitor in the circuit at each wire attachment. These effects can then lead to the creation of an electrical field that may impact the electrochemical potential, a factor that has been shown to highly impact intergranular corrosion (IGC) and intergranular stress corrosion cracking (IG-SCC)[11–15]. A detailed investigation into these potentially confounding effects has not been explicitly reported in the literature. As such, there is a knowledge gap on the impact of in-solution dcPD current wire attachment on the electrochemical conditions at the material surface.

6.2.1. Chapter objective

The objective of this study is to investigate the impact of applied dcPD current on the measured electrochemical surface conditions for testing configurations with exposed dcPD current wire attachments. Specifically, the effects of dcPD current wire attachment method, electrolytic solution conductivity, and corrosion damage will be investigated. Observed changes in either the electrochemical potential or voltage will then be analyzed as dcPD current is applied and terminated. Finally, a testing profile similar to one employed in IG-SCC testing will be performed to inform testing methodologies and estimate potential errors that may accrue over the testing duration.

6.3. Experimental methods and material

6.3.1. Materials and sample prep

Two common engineering alloys were investigated in this study, AA7075-T651 aluminum alloy and 17-4 PH stainless steel. Prior to testing, samples were cleaned by sonication in acetone, methanol, and DI water, respectively for 15 min each and subsequently dried with pressurized air. A copper wire (0.127 mm diameter) coated in PFA (perfluoroalkoxyalkane) was spot welded onto the sample and covered with a rubber butyl stop-off lacquer to serve as a working electrode. For the dcPD current wires platinum wire of 1 mm diameter was either mechanically attached into mechanical contact *via* vinyl electrical tape without any metallurgical bond, termed the 'mechanical contact' condition, or platinum wires of 0.25 mm diameter were spot welded onto either side of the sample in a braid of four wires, termed the 'spot welded' condition, and left uncovered.

6.3.2. Environmental setup and testing

Samples were connected to a direct current power supply via the dcPD current platinum wires and suspended in a 500 mL borosilicate beaker. A platinum mesh and a saturated calomel electrode (SCE) were also placed into the beaker to form a standard three-cell electrochemical setup, acting as the counter electrode and reference electrode respectively. Solutions of de-ionized (DI) water, 0.6 M NaCl, saturated (5.45 M) NaCl, or acetonitrile were then poured into the beaker to serve as an electrolyte. Electrical conductivities of these solutions were measured and listed in Table 6.1. For solutions tested in saturated NaCl solution additional testing was performed after letting the sample sit for 72 hours. The initial investigation was conducted by cycling the power supply on and off according to a schedule listed in Table 6.2 (this protocol is following a one hour hold to achieve signal stability). A 6 Amp dcPD current was used during mechanical attached testing and a 4 A dcPD current was used during spot welded testing due to differences in current carrying capacity. During this cycling of the current two metrics were monitored at a 5 Hz collection rate to determine the impact of the current application on the surface conditions of the sample. First, the electrochemical open circuit potential, termed "OCP"; this serves as a direct measure change in the surface conditions in response to the applied current. Second, current required to retain a set electrochemical potential near the measured OCP, termed "SetE". This is an indirect measure of changes but enables a higher level of precision and eliminates the complicating impact of OCP drift that is commonly observed in these materials independent of any outside current application.

Table 6.1. Measured electrical conductivities for the testing solutions.

Solution	Conductivity (µS/cm)
Acetonitrile	5.2
DI Water	102.5
0.6 M NaCl	24,590
Sat. NaCl	175,500

Table 6.2. Stepped dcPD current testing schedule.

Start Time (min)	**End Time (min)**	**Δt (min)**	**Current status**
0	1	1	off
1	2	1	on
2	4	2	off
4	6	2	on
6	9	3	off
9	12	3	on
12	16	4	off
16	20	4	on
20	25	5	off
25	30	5	on

Representative testing solutions for each of the alloys were then chosen to further explore current profiles that better represent actual SCC testing and the effects of extended testing durations on the evolution of observed changes. These environmental setups were created exactly as described above with the exception of the current wires being attached to an Amrel® PD5-20A programmable DC power supply. Before testing a 2 hr hold was performed with no applied dcPD current, followed by another 2 hr hold in which a constant 4A current was applied. A 6 hr test was then conducted wherein the 4A current was applied with a 10 second data collection "cycle" taken every 30 seconds. During these collection cycles the dcPD current polarity was switched back and forth 10 times with 0.5 seconds between each polarity switch.

6.4. Results

6.4.1. Stepped dcPD current OCP testing

Electrochemical potential measurements taken during OCP testing of various dcPD current wire attachment methods and environments are reported in Table 6.3. Values recorded are both the minimum and maximum instantaneous changes in electrochemical potential whenever a dcPD current was applied or terminated, termed 'Δ_{Instant}' in the data, and maximum change in electrochemical potential between the power application/removal, termed 'Δ_{Total}' in the data. Visual representation of these values can be seen in Figure 6.1 for OCP testing of AA7075-T651 in DI water wherein the dcPD wires were mechanical attached to the sample. It can be seen in Table 6.3 that for AA7075-T651 when the dcPD current wires were mechanically attached that the largest changes in electrochemical potential occurred when tested in DI water, although testing in saturated NaCl also showed large changes in potential. The observed changes for mechanically attached dcPD current wires were much larger across all environments than the corresponding tests of AA7075-T651 with spot welded dcPD current wires, an example of which is shown in Figure 6.2 for OCP testing DI water and Figure 6.3 for OCP testing in saturated NaCl. For the tests in which the dcPD current wires were instead spot welded onto the sample the largest instantaneous electrochemical potential changes occurred in a saturated NaCl solution left to sit for 72 hours, shown in Figure 6.4, and the largest overall electrochemical potential changes between steps occurred in acetonitrile. For the 17-4 PH stainless steel specimen with dcPD wires connected via spot welding the largest electrochemical potential changes occurred in DI water.

Table 6.3. Electrochemical potential changes (mV) collected during OCP direct current application testing.

dcPD OCP Testing (mV)		**dcPD On**				**dcPD Off**			
		$\Delta_{Instant}$ Min	**$\Delta_{Instant}$ Max**	**$\Delta_{Instant}$ Direction**	**Δ_{Total}**	**$\Delta_{Instant}$ Min**	**$\Delta_{Instant}$ Max**	**$\Delta_{Instant}$ Direction**	**Δ_{Total}**
AA7075 (Mechanical Contact)	DI Water	5	10	+	45	4	8	-	45
	0.6 M NaCl	4	10	+	2	0.5	2	-	4
	Saturated	10	20	+	2	3	7	-	3
AA7075 (Spot Welded)	Acetonitrile	0	0	N/A	6	0	0	N/A	7
	DI Water	0	0	N/A	3	0	0	N/A	10
	0.6 M NaCl	0	1	+	0.7	0	0	N/A	0
	Saturated	0	0	N/A	0.7	0	0	N/A	1
	72 Hr Sat.	2	3	-	0.6	2	3	+	0.8
17-4 PH (Spot Welded)	Acetonitrile	0	8	-	13	0	3	+	5
	DI Water	25	70	-	125	10	60	+	170
	0.6 M NaCl	12	20	-	36	13	16	+	29
	Saturated	1	1	+	3	1	2	-	3
	72 Hr Sat.	23	30	+	38	27	35	-	39

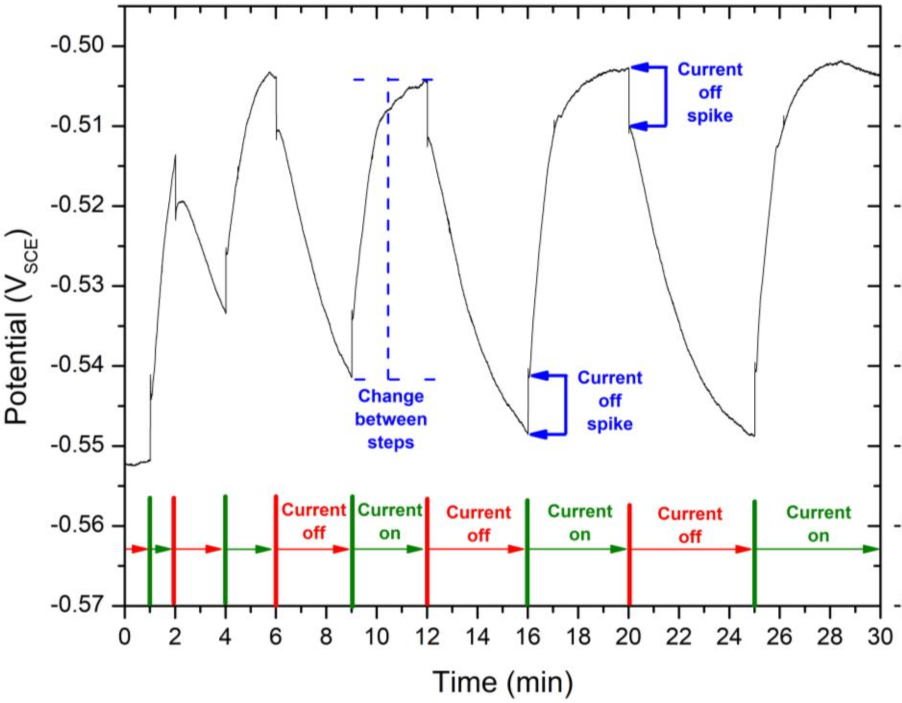

Figure 6.1. Electrochemical potential profile during stepped dcPD current testing for AA7075-T651 tested in DI water with platinum current wires mechanical attached to the sample.

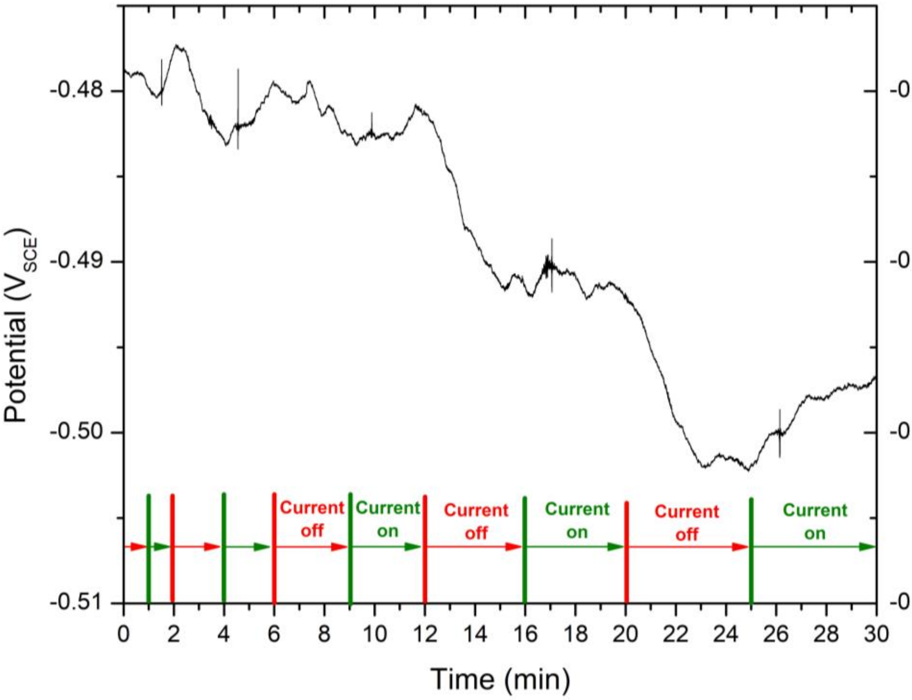

Figure 6.2. Electrochemical potential profile during stepped dcPD current testing for AA7075-T651 tested in DI water with platinum current wires spot welded to the sample.

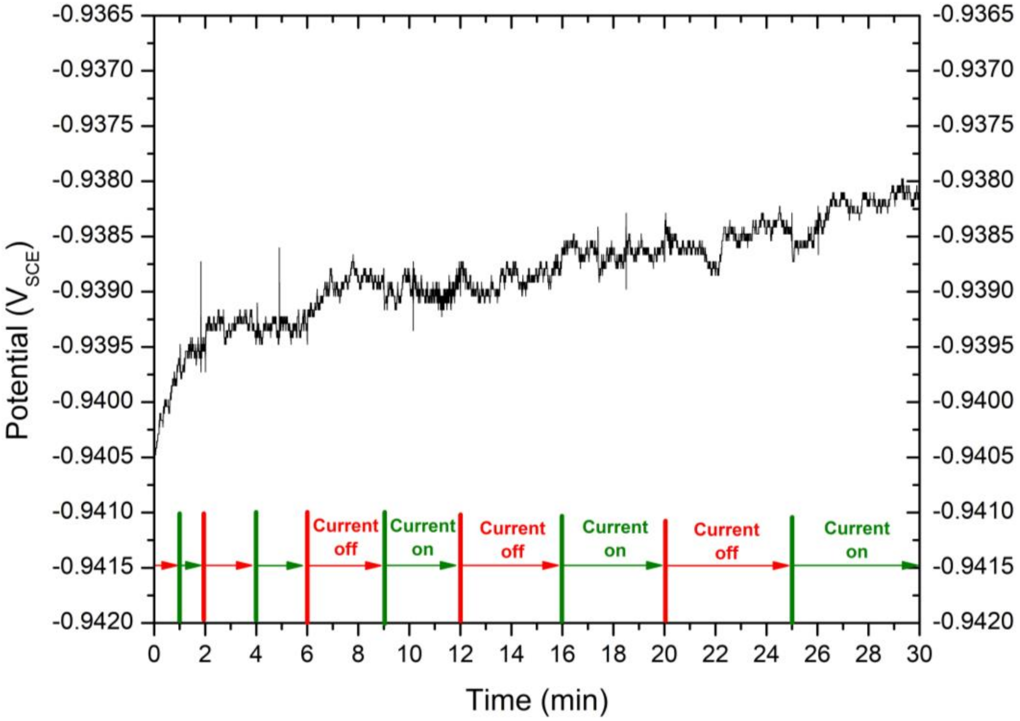

Figure 6.3. Electrochemical potential profile during stepped dcPD current testing for AA7075-T651 tested in saturated NaCl with platinum current wires spot welded to the sample.

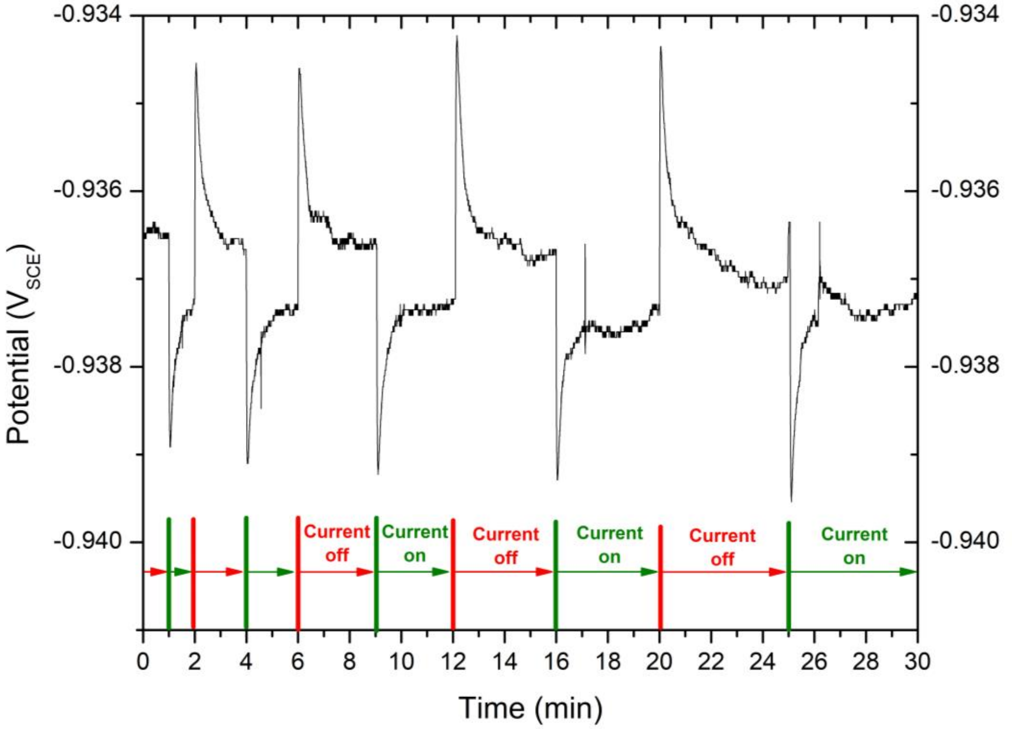

Figure 6.4. Electrochemical potential profile during stepped dcPD current testing for AA7075-T651 tested in saturated NaCl after a 72 hour hold with platinum current wires spot welded to the sample.

6.4.2. Stepped dcPD current SetE testing

Electrochemical current measurements taken during set electrochemical potential testing of various dcPD current wire attachment methods and solution conductivities are reported in Table 6.4. Values recorded are instantaneous changes in electrochemical current whenever a dcPD current was applied or terminated and maximum changes in electrochemical voltage between these events, analogous to the parameters shown in Figure 6.1 for the electrochemical potential and now demonstrated in Figure 6.5 for SetE testing under the same conditions. For the AA7075-T651 sample with mechanically attached dcPD wires the largest changes in electrochemical current occurred in saturated NaCl. For the AA7075-T651 sample with spot welded wires, the largest current changes occurred during testing in saturated NaCl left to sit for 72 hours. For the 17-4 PH stainless steel specimen with spot welded dcPD current wires the largest electrochemical current changes occurred in 0.6 M NaCl.

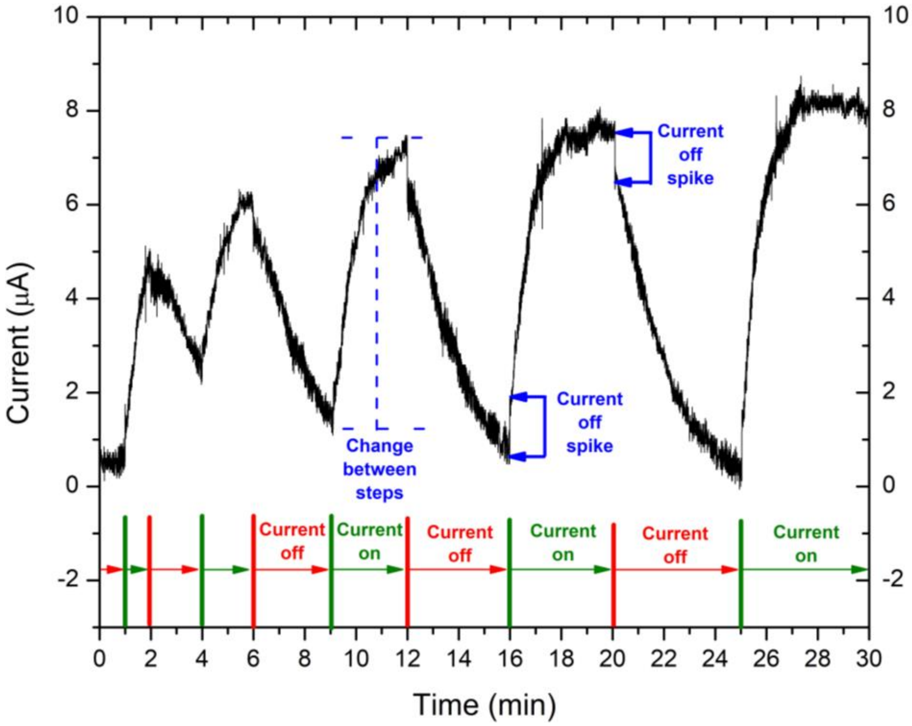

Figure 6.5. Electrochemical current profile during stepped dcPD current testing for AA7075-T651 tested in DI water with platinum current wires mechanical attached to the sample.

Table 6.4. Electrochemical current changes (μA) collected during SetE direct current application testing.

dcPD SetE Testing (μA)		**dcPD On**				**dcPD Off**			
		Δ_{Instant} Min	**Δ_{Instant} Max**	**Δ_{Instant} Direction**	**Δ_{Total}**	**Δ_{Instant} Min**	**Δ_{Instant} Max**	**Δ_{Instant} Direction**	**Δ_{Total}**
AA7075 (Mechanical Contact)	DI Water	0	1	+	8	0	1	-	8
	0.6 M NaCl	100	300	+	100	0	100	-	300
	Saturated	150	150	+	150	100	150	-	46
AA7075 (Spot Welded)	Acetonitrile	0	0	N/A	0	0	0	N/A	0
	DI Water	0	0	N/A	0.4	0	0	N/A	0.5
	0.6 M NaCl	0	0	N/A	29	0	0	N/A	10
	Saturated	6	13	-	18	9	24	+	39
	72 Hr Sat.	106	116	-	51	105	111	+	78
17-4 PH (Spot Welded)	Acetonitrile	0	0	N/A	0	0	0	N/A	0
	DI Water	1.1	1.6	-	0	0	0	N/A	0
	0.6 M NaCl	7	8	-	29	10	11	+	15
	Saturated	0	0	N/A	0	0	0	N/A	0
	72 Hr Sat.	0	0	N/A	0	0	0	N/A	0

6.4.3. Effect of dcPD current polarity on electrochemical parameters

Electrochemical potential profiles for AA7075-T651 in saturated NaCl and 17-4 PH stainless steel in DI water tested with dcPD current profiles comparable to SCC testing are shown in Figures 6.6 and 6.7 respectively. These conditions were chosen for each alloy as they showed the largest electrochemical potential and/or current changes, thus representing the most error-prone conditions. Magnification of the electrochemical profile at 0, 1, 2, and 5 hours are shown in Figure 6.8a-d for AA7075-T651 in saturated NaCl and Figure 6.9a-d for 17-4 PH stainless steel in DI water. These figures reveal a sinusoidal waveform of 10 cycles with a 1 second period that repeats with 30 second intervals of no fluctuation in between. Magnitudes above and below the starting electrochemical potential of the collection cycle, represented by the amplitude of the waveform, are reported in Tables 6.5 and 6.6 for AA7075-T651 in saturated NaCl and 17-4 PH stainless steel in DI water respectively. The largest observed instantaneous change in electrochemical potential was ~20 mV for the AA7075-T651 in saturated NaCl and ~1 mV for the 17-4 PH stainless steel in DI water.

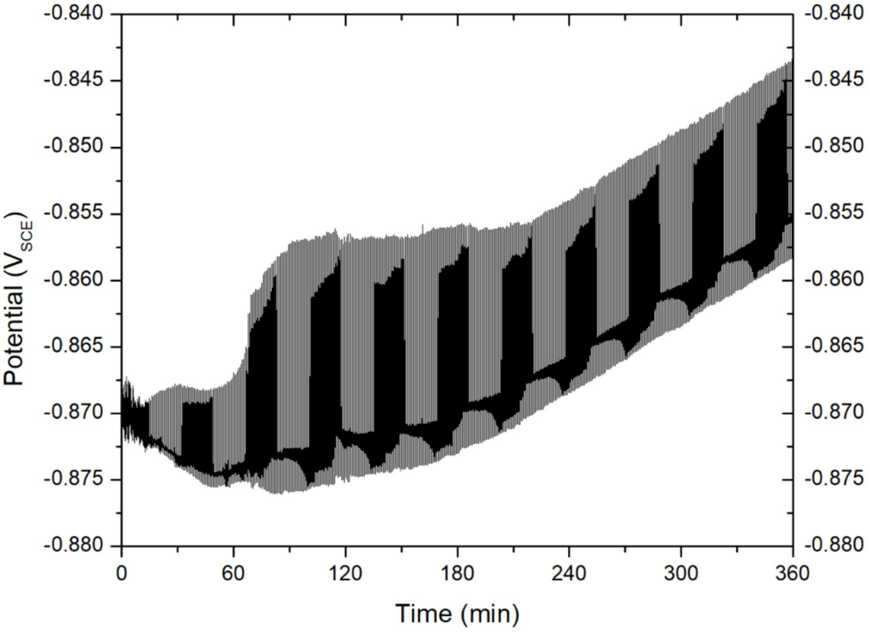

Figure 6.6. Electrochemical potential profile of AA7075-T651 in saturated NaCl solution with spot welded current wires during an SCC dcPD current profile. Note the gray region is an artifact of the plotting software resolution and is comprised of many close sinusoidal oscillations.

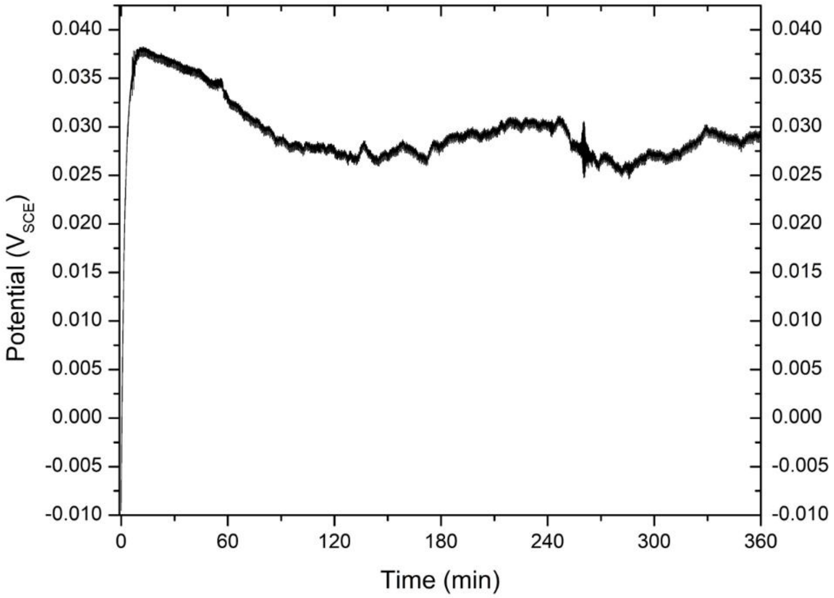

Figure 6.7. Electrochemical potential profile of 17-4 PH stainless steel in DI water with spot welded current wires during an SCC dcPD current profile.

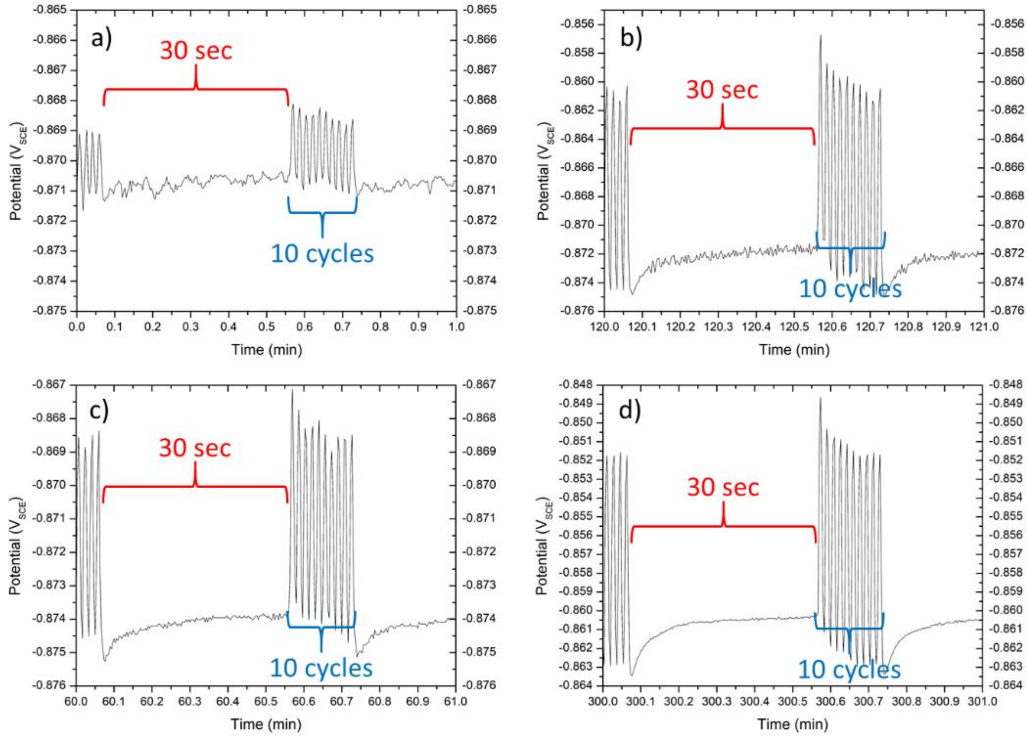

Figure 6.8. Magnifications of the electrochemical potential profile of AA7075-T651 in saturated NaCl solution with spot welded current wires during an SCC dcPD current profile shown in Figure 6.6. Times shown are a) at the start of testing, b) 1 hour into testing, c) 2 hours into testing, and d) five hours into testing. All profiles show a repeating 10 cycle sinusoidal pattern every 30 seconds, corresponding to the current profile wherein the current polarity was switched 10 times every 30 seconds.

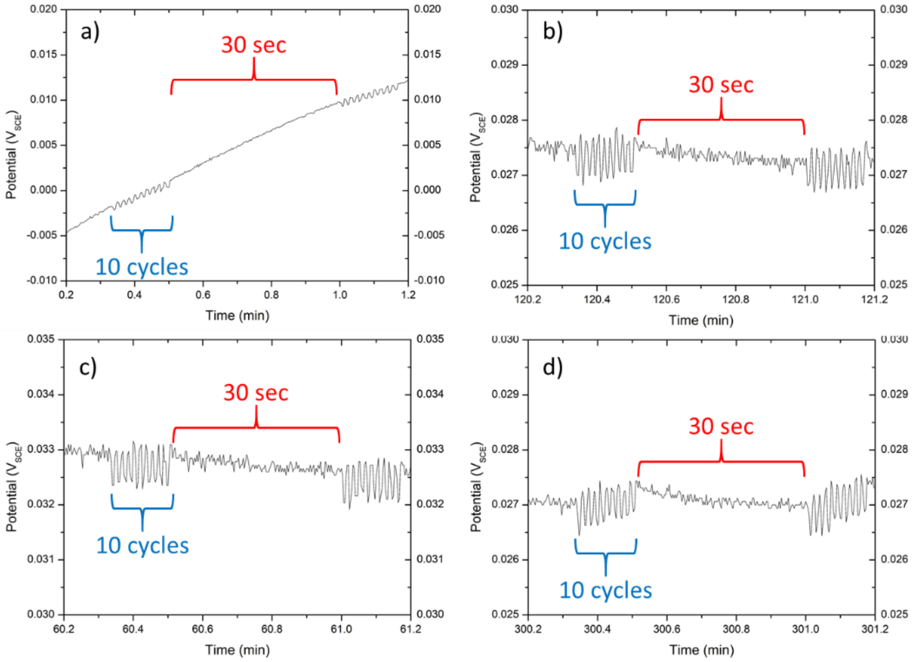

Figure 6.9. Magnifications of the electrochemical potential profile of 17-4 PH stainless steel in DI water with spot welded current wires during an SCC dcPD current profile shown in Figure 6.7. Times shown are a) at the start of testing, b) 1 hour into testing, c) 2 hours into testing, and d) five hours into testing. All profiles show a repeating 10 cycle sinusoidal pattern every 30 seconds, corresponding to the current profile wherein the current polarity was switched 10 times every 30 seconds.

Table 6.5. Electrochemical potential changes (mV) above and below the midline during a sinusoidal SCC testing cycle for AA7075-T651 in saturated NaCl.

Time (hr)	Δ_{Cycle} (+)	Δ_{Cycle} (-)
0	3 mV	0 mV
1	7 mV	1 mV
2	15 mV	4 mV
5	12 mV	3 mV

Table 6.6. Electrochemical potential changes (mV) above and below the midline during a sinusoidal SCC testing cycle for 17-4 PH stainless steel in DI water.

Time (hr)	Δ_{Cycle} (+)	Δ_{Cycle} (-)
0	0 mV	1 mV
1	0.25 mV	0.5 mV
2	0.25 mV	0.5 mV
5	0.25 mV	0.5 mV

6.5. Discussion

From Tables 6.3 and 6.4 it can be clearly seen that across multiple testing configurations electrochemical potential and/or voltage can be influenced by the application of a dcPD current. This discussion will therefore be divided into four separate parts in order to address the various factors indicated by the results that may affect the electrochemical potential/voltage applied. These factors are identified as: (1) dcPD wire attachment method, (2) testing environment conductivity, (3) environment-induced corrosion damage, and (4) dcPD current polarity and testing duration. The impact of each of these parameters will be isolated from the data and an attempt to explain observed trends will be derived from established behaviors.

6.5.1. Effect of dcPD wire attachment method

The nature of the bond between dcPD current wire and specimen surface will impact the electrical resistance at the interface, thus is expected to potentially affect the measured electrochemical properties of the system. While it is generally assumed that the dcPD current applied runs solely through the metal sample due to its vastly higher electrical conductivity, a substantial increase in the resistance at the interface between the current application wire and the sample may invalidate this assumption[6,7]. For a mechanical bond this could happen via ingress of thin layers of electrolytic solution and/or oxide layers or corrosion product formed on the sample surface can act as barriers to electrical current. For metallurgical bonds, this contact could be degraded via poor weld attachments or corrosion of the interface. When electrical resistance through the sample is increased, current can be "bled" through the external electrolyte which can lead to changes in the measured electrochemical potential. As such, any of the above degradation mechanisms would result changes in measured electrochemical potential upon changes in the applied dcPD current. As expected, Table 6.3 demonstrates that electrochemical potential changes for AA7075-T651 with mechanically attached dcPD wires resulted in drastically larger Δ_{Instant} upon application/termination of the dcPD current than AA7075-T651 with spot welded dcPD current wires across all comparable testing solutions. This is reasonably considering expected higher level of resistivity with a mechanical contact as compared to the metallurgical bond and the higher propensity of subsequent degradation for such a mechanical bond.

The electrochemical behavior observed in Figures 6.1 and 6.5 can also be explained using similar reasoning. As the dcPD current wires and the metal sample are highly conductive materials separated by the electrolyte and/or oxide layers, which are far less conductive, the dcPD current wire connections functionally serve as capacitors in an electrical circuit. As current is applied, electrical fields between the two connections build and energy is stored. These building electrical fields will change the measured electrochemical potential accordingly as long as the capacitors continue to charge. This can be seen in Figures 6.1 and 6.5 by the building potential/current whenever the dcPD current is applied. Upon removal of this current, the capacitors will discharge their stored energy conversely and the system will return to roughly equilibrium conditions seen before testing. In Figure 6.1 this is seen to be roughly -0.55 V_{SCE} and in Figure 6.5 to be roughly 0.5 μA. Should the resistive layer between the connections be minimized, such as by spot welding the wire to the sample surface to produce a strong metallurgical contact, these effects should be minimized greatly, as is seen in Figure 6.2 for the electrochemical potential. Therefore, it is vitally important that a strong connection be made with the dcPD current wires no matter the testing environment.

6.5.2. Effect of testing environment conductivity

While it is generally assumed that the bulk of dcPD current applied through the sample is limited solely to pathways through the metal sample (given proper metallurgical contact), electrical principles dictate small amounts of current will still be “bled” through the surrounding solution pathway as it will act as a parallel circuit for the current. The magnitude of this current will be dependent on the solution electrical conductivity, with higher conductivities offering lower electrical resistance and potentially higher amounts of bled current. Conversely, less conductive solutions could provide higher resistances to alternative electrical pathways through the solution and thus mitigate this lost current almost entirely. From Table 6.3 we can see that for spot-welded AA7075-T651 testing no solution (barring the test run in saturated NaCl after 72 hours which will be discussed later) resulted in either significant $\Delta_{Instant}$ or changes in electrochemical potential beyond that of the OCP drift typically observed for aluminum alloys. This is also largely true for electrochemical current during SetE testing, shown in Table 6.4, except for the saturated NaCl test which showed significant changes. Since no distinguishable trends were observed across the various solution conductivities, it is therefore likely that the AA7075-T651 achieved proper metallurgical contact and little to no current was bled through the surrounding solution. This is in line with the assumption that dcPD current is isolated to pathways through the sample, and indicates that solution conductivity has little effect in testing with this alloy.

For the 17-4 PH stainless steel sample with spot welded attachments, on the other hand, a trend was observed with solution conductivity. Testing in acetonitrile and saturated NaCl, the solutions with the lowest and highest electrical conductivities respectively, showed almost no change in electrochemical potential or voltage similar to AA7075-T651 testing. Testing in DI water, however, showed the largest changes in electrochemical potential while testing in 0.6 M NaCl showed the largest changes in electrochemical current. This is unexpected, as one would expect the trend to scale with conductivity, specifically with higher electrochemical changes occurring in higher solution conductivities due to greater amounts of bled current. A justification for this non-linear behavior is unknown, but indicates that solution conductivity is not the sole factor in determining the amount of bled current observed. This discrepancy may be due to additional factors at the metal/solution interface, such as additional oxide formation at higher chloride concentrations, that may provide additional barriers to electrical conductivity through the solution. While the exact correlation with solution conductivity merits further study, the presence of such a trend for the 17-4 stainless steel can be justified by the nearly order of magnitude lower electrical conductivity as compared to an aluminum sample. This decreased conductivity would further promote alternative electrical pathways through the solution, and is in line with expected behavior using the reasoning above.

6.5.3. Effect of environment-induced corrosion damage

While efforts may be made to ensure proper dcPD current wire connections prior to testing, exposure of the dcPD current wires to a corrosive solution may create a time-dependent factor as the connection corrodes. As the connections corrode, metallurgical contact is decreased and replaced with less-conductive corrosion product that may serve as an additional electrical barrier and further increase the capacitance. This will in turn increase the magnitude of electrochemical changes observed as corrosion continues. From Tables 6.3 and 6.4 it can be seen that this is exactly the trend observed, with tests held in saturated NaCl solutions for 72 hours resulting in much larger changes in electrochemical parameters for AA7075-T651. This can be seen by comparing Figures 6.3 and 6.4, and was additionally confirmed by the presence of extensive hydrogen gas evolution during testing and localized corrosion at the dcPD current wire connections sites following test completion as evidenced in Figure 6.10a-b. For 17-4 PH stainless steel this was also observed for the electrochemical potential, but for the electrochemical current no change was observed. Localized corrosion was not visually present along the dcPD current wire connections for this alloy, as seen in Figure 6.10c, which indicates a loss in connection was not seen, although non-visible corrosion may still have occurred. Therefore, the origin for the increase in electrochemical potential is unknown for this alloy.

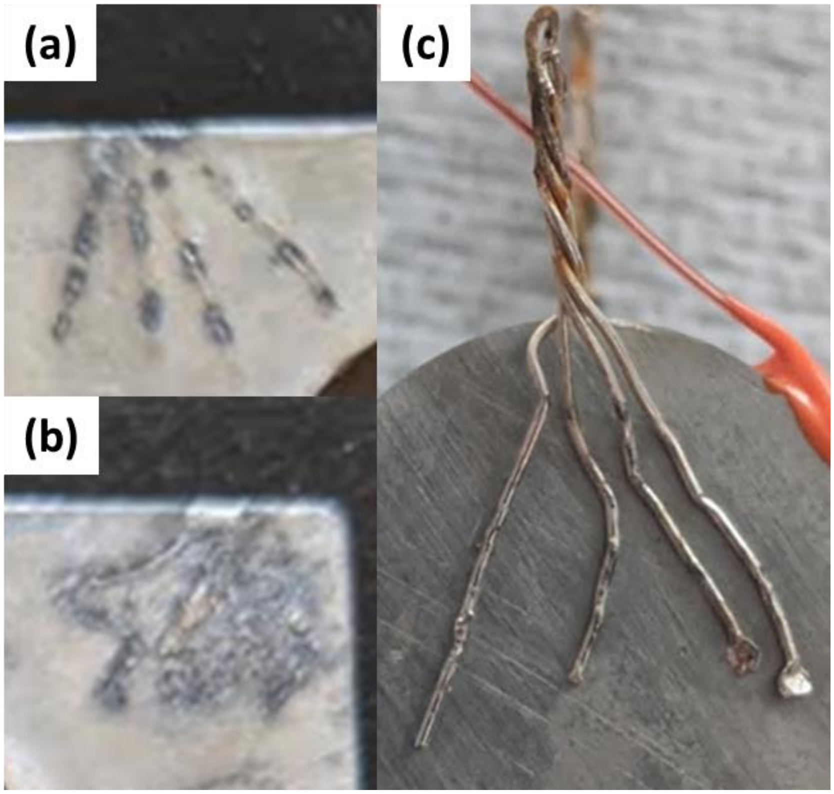

Figure 6.10. Visual images of dcPD current wire attachments following testing in saturated NaCl solution for 72 hours for (a-b) AA7075-T651 and (c) 17-4 PH stainless steel. For AA7075-T651 the platinum dcPD current wires were easily detached following test completion and are thus not pictured.

6.5.4. Effect of dcPD current polarity and testing duration

Although dcPD crack growth monitoring is nominally performed using a direct current power source, dcPD collection protocols typically employing polarity switching during data collection for the increased accuracy and mitigation of thermoelectric effects germane to dcPD testing. This switch in polarity is usually performed multiple times per data cycle to ensure proper sampling of the measured dcPD voltage. Given the results seen earlier, it is therefore possible that during these data collection cycles the electrochemical properties will be highly variable and potentially have a strong impact on the surface electrochemistry. Furthermore, it can be observed in Figure 6.4 that a time-dependent behavior sometimes evolved during testing, with larger electrochemical changes occurring for each subsequent current application/termination. Consequently, in order to investigate the potential magnitude of these effects each of the alloys was subjected to a standard dcPD testing current profile akin to one that would be used in SCC testing while the electrochemical potential was monitored[11,16,17]. For each alloy the testing solution that exhibited the largest changes in electrochemical properties during the previous stepped current application tests, saturated NaCl for AA7075-T651 and DI water for 17-4 PH stainless steel, was used to best illustrate the potential effects observed. The duration of each test was extended to 6 hours in an attempt to fully encompass the time-dependency of these changes. These tests are shown in Figures 6.6 and 6.7 respectively.

For AA7075-T651, it is apparent that a wide spread in the electrochemical potential was recorded during the entirety of testing. Magnification of this profile at various times, as is done in Figure 6.8, shows that these variations occur exactly when the polarity switches during data collection cycles. Additionally, it can be seen in Figure 6.6 and Table 6.5 that these Δ_{Cycle} generally grew larger as the test progressed, most likely due to the increasing effects of corrosion damage on the connection interface as discussed earlier. These Δ_{Cycle} are much larger than those seen in earlier testing for this solution, and indicates that switching the polarity seems to have an increased effect on the magnitude of the Δ_{Cycle}. This most likely results from the capacitor-like behavior of the dcPD current wire connection, wherein the constant current applied between the data collection cycles would accumulate electrical charge along the two interfaces. During data collection cycles, when the polarity is switched and not simply turned off as in the previous tests, the effects of a reversed polarity would be magnified as the previously established electric fields would now be opposing. This would also explain the apparent asymmetry of the Δ_{Cycle}, with the largest changes resulting from when the polarity is switched from its “base” polarity applied between collection cycles.

For 17-4 PH stainless steel a similar trend is observed, albeit with a few key differences. Analysis of Figure 6.7 does not demonstrate the correlation of electrochemical potential with data collection cycle as clearly, but magnification of the profile in Figure 6.9 once again shows the same 30 second data collection cycle followed by 10 cycles. Unlike AA7075-T651, which showed an enhanced magnitude in electrochemical potential changes, the Δ_{Cycle} recorded for 17-4 PH stainless steel are drastically lower than those observed in previous testing. This discrepancy most likely results from the lower electrical conductivity of stainless steel as compared to aluminum, which would result in longer polarization times and less immediate changes in charging. This can be further seen in Figure 6.7, wherein the first three minutes of testing resulted in a large change in electrochemical potential before stabilizing. This initial change was not seen in Figure 6.6 for AA7075-T651, and most likely is the time needed to fully establish the electric fields for the primary polarity. Furthermore, this initial jump in potential is consistent with the values and trends seen in previous testing.

6.5.5. Implications & future work

From these results it can be seen that multiple factors may ultimately have an impact on the electrochemical behavior observed and should be taken into account in SCC testing protocols. Primarily, it is observed that the electrical connection between the dcPD wire and sample surface was seen to have the largest impact on SCC testing, with large changes in electrochemical parameters being observed when a constant metallurgical bond was not established or maintained. In order to decrease the magnitudes of these effects strong metallurgical bonding techniques, corrosion protection protocols, and reduced testing durations are all potential avenues of mitigation that would address these concerns. Secondly, solution conductivity was found to have a more minor impact under certain solution conductivities even when strong metallurgical bonding was established. The exact nature and derivation of this behavior is still not fully understood, however, and merits further study as trends were found to be highly dependent on alloy composition.

6.6. Conclusions

The impact of an applied dcPD electrical current on the electrochemical properties of various testing setups and solutions with exposed dcPD current wire attachments was investigated. The factors investigated were dcPD current wire application method, testing solution conductivity, extent of corrosion damage, and the dcPD current polarity. Ultimately it was determined that the dcPD wire attachments acted akin to capacitors without proper metallurgical contact, and could lead to substantial changes in measured electrochemical potential and/or voltage.

- ❖ Application method was determined to have a large impact on recorded electrochemical parameters, with larger potentials and currents observed when improper metallurgical contact was made between the dcPD current wires and the sample.
- ❖ Solution conductivity was observed to have an alloy-dependent trend on measured electrochemical parameters. For AA7075-T651 solution conductivity had very little effect on electrochemical potential, but high electrical conductivity solutions resulted in larger changes in electrochemical current. For 17-4 PH stainless steel testing solution conductivities in the median range resulted in the largest changes in both electrochemical potential and current.
- ❖ Subjecting both alloys to a highly corrosive environment to induce corrosion damage resulted in much larger changes to the electrochemical parameters as compared to their pre-corroded conditions.
- ❖ Application of a dcPD crack growth sampling current profile, akin to SCC testing, shows that switching the dcPD current polarity could have substantial effects, especially for more conductive metals such as aluminum.

6.7. References

1. R. Horstman, K. Lieb, B. Power, R. Meltzer, M. Vieth, G. Aronson, and R. Ritchie, *J. Test. Eval.* 7 (1979): p. 208.
2. J.K. Donald and J. Ruschau, *Fatigue Crack Measurement; Techniques and applications* (1991): pp. 11-38.
3. R.P. Gangloff, *Fatigue Fract. Eng. Mater. Struct.* 4 (1981): pp. 15–31.

4. E647-15e1. Standard Test Method for Measurement of Fatigue Crack Growth Rates. *ASTM B. Stand.* 1–49 (2016). doi:10.1520/E0647-15E01.2
5. Z.D. Harris, E.M. Dubas, A.S. Popernack, B.P. Somerday, and J.T. Burns, *Theor. Appl. Fract. Mech.* (n.d.): p. in review.
6. R.P. Gangloff, *Metall. Trans. A* 16 (1985): pp. 953–969.
7. R.S. Piascik, "Mechanisms of Intrinsic Damage Localization During Corrosion Fatigue: Al-Li-Cu System," University of Virginia, 1989.
8. P.L. Andresen, and M.M. Morra, *J. Press. Vessel Technol. Trans. ASME* 129 (2007): pp. 488–506.
9. Y. Ashida, A. Flick, P.L. Andresen, and G.S. Was, *Corrosion* 69 (2013): pp. 136–144.
10. P.L. Andresen, *Corrosion* 64 (2008): pp. 439–464.
11. M.E. Mcmahon, P.J. Steiner, A.B. Lass, and J.T. Burns, *Corrosion* 73 (2017): pp. 347–361.
12. C.B. Crane, R.G. Kelly, and R.P. Gangloff, *Corrosion* 72 (2016): pp. 242–263.
13. J.L. Searles, P.I. Gouma, and R.G. Buchheit, *Metall. Mater. Trans. A Phys. Metall. Mater. Sci.* 32 (2001): pp. 2859–2867.
14. R.H. Jones, D.R. Baer, M.J. Danielson, and J.S. Vetrano, *Metall. Mater. Trans. A* 32 (2001): pp. 1699–1711.
15. S.K. Lee, P. Lv, and D.D. Macdonald, *J. Solid State Electrochem.* 17 (2013): pp. 2319–2332.
16. M.E. Mcmahon, P.J. Steiner, A.B. Lass, and J.T. Burns, *Corrosion* 73 (2017): pp. 713–723.
17. P. Steiner, and J. Burns, *ICF 2017 - 14th Int. Conf. Fract.* 1 (2017): pp. 566–567.

Chapter 7. Summary and conclusions

7.1. Overview

This chapter summarizes the key conclusions emerging from the work completed in this dissertation.

7.2. Summary and Key Conclusions

1. The intergranular stress corrosion cracking susceptibility of AA5083-H131 and AA5456-H116 alloys sensitized at 100°C to NAMLT values of 22 mg/cm^2 and 40 mg/cm^2 were assessed in various full-immersion and atmospheric environments (misting and wicking) in 0.6 M NaCl with no set potential. Tensile testing was performed with high-resolution crack growth monitored using the dcPD method and constantly replenished environments with 0.6 M NaCl solution. It was found that for a constant electrolyte composition, AA5083-H131 and AA5456-H116 testing in atmospheric environments showed decreased IG-SCC susceptibility as compared to full immersion experiments with a set -0.8 V_{SCE} potential. Retarded crack growth kinetics are attributed to cathodic limitation of the governing IG-SCC mechanism and correlate with known potential-dependent IG-SCC observations. Novel use of a sintered silver/silver chloride probe allowed for in-situ electrochemical potential measurements and polarization in these atmospheric environments. Fluctuations in the OCP of the bulk surface directly correlated with trends in the crack growth kinetics for environments (full immersion, misting, and wicking) without a set potential.
2. A novel protocol for conducting LEFM-based IG-SCC testing under thin film environments was established through implementation of AAO membranes. The IG-SCC susceptibility of the alloy AA5083-H131 sensitized at 100°C to a NAMLT value of 40 mg/cm^2 was assessed at various nominal thin film thicknesses ranging from 54 to 229 µm using this protocol in 0.6 M NaCl electrolyte. Verification experiments coupled with finite element simulations indicate that the AAO-based approach for implementing thin film environments will not significantly affect oxygen diffusion kinetics or the ohmic resistance of the thin film. For a constant electrolyte composition, testing of AA5083-H131 in thin film environments suggests increased IG-SCC susceptibility past a critical thickness

consistent with known geometry-induced cathodic limitation behaviors. For thin film thicknesses past this critical thickness, a dual behavior was observed between duplicates. The origin of this behavior, whether procedural or actual, is unknown. Results also suggest that oxygen diffusion rates through the thin film geometry had a minor effect as compared to ohmic drop through the solution. Fluctuations in the OCP of the bulk surface once again directly correlated with trends in the crack growth kinetics for all observed thin film thicknesses.

3. The IG-SCC susceptibility of AA5083-H131 sensitized to 40 mg/cm^2 was investigated for multiple model atmospheric environments and chloride concentrations ranging from 0.3 M NaCl to 5.45 M NaCl. For each atmospheric environment an increase in chloride concentration resulted in increased IG-SCC susceptibility (resulting in lower K_{TH} values and higher da/dt_{II} crack growth rates), but IG-SCC susceptibility was found to decrease across each chloride concentration as cathodic limitation from solution geometry-induced effects increased. As chloride concentration increased, cathodic limitation was found to have a no discernable effect on the K_{TH} or da/dt_{II} crack growth rates observed between non-polarized and polarized environments. The electrochemical potential data supports the observation that anodic demand at the crack tip increases as chloride concentration increases and cathodic limitation increases as solution geometry decreases. Conservative estimates for atmospheric IG-SCC crack growth rates can be achieved by using full immersion testing at a set potential at the highest anticipated chloride concentration.
4. The IG-SCC susceptibility of the alloy AA5456-H116 sensitized at 100°C to a NAMLT value of 65 mg/cm^2 was assessed at various electrochemical potentials established *via* SSC probe or a ZRP in a misting environment. Polarization of misting tests *via* SSC electrode resulted in diminished electrochemical potential-dependent IG-SCC susceptibility trends as compared to full immersion testing. Testing of a candidate ZRP in a misting environment was seen to result in a reduction of the IG-SCC susceptibility similar to that seen in polarized misting conditions. Increasing the scribe width of the tested ZRP up to 10 mm resulted in no discernable change in the IG-SCC susceptibility in misting environments. Electrochemical measurements obtained during ZRP testing indicate a

protective potential was largely able to be applied during the entirety of testing. Typical electrochemical behavior collected during OCP testing, wherein the bulk surface acts as the cathode and decreases in potential as anodic demand increases, was not observed when a ZRP was present.

5. The impact of an applied dcPD electrical current on the electrochemical properties of various testing setups and solutions with exposed dcPD current wire attachments was investigated. The factors investigated were dcPD current wire application method, testing solution conductivity, extent of corrosion damage, and the dcPD current polarity. Application method was determined to have a large impact on recorded electrochemical parameters, with larger potentials and currents observed when improper metallurgical contact was made between the dcPD current wires and the sample. Solution conductivity was also observed to have an alloy-dependent trend on measured electrochemical parameters, albeit at a reduced factor. For AA7075-T651 the solution conductivity had very little effect on electrochemical potential, but high electrical conductivity solutions resulted in larger changes in electrochemical current. For 17-4 PH stainless steel testing the solution conductivities in the median range resulted in the largest changes in both electrochemical potential and current. Subjecting both alloys to a highly corrosive environment to induce corrosion damage resulted in much larger changes to the electrochemical parameters as compared to their pre-corroded conditions. Application of a dcPD crack growth sampling current profile, akin to SCC testing, shows that switching the dcPD current polarity could have substantial effects, especially for more conductive metals such as aluminum. Ultimately it was determined that the dcPD wire attachments acted akin to capacitors without proper metallurgical contact, and could lead to substantial changes in measured electrochemical potential and/or voltage.